Synthesis of Anisotropic Magnetic Nanoobjects Designed for Locomotion in External Magnetic Fields

Inaugural-Dissertation

Zur

Erlangung des Doktorgrades

Der Mathematisch-Naturwissenschaftlichen Fakultät

der Universität zu Köln

vorgelegt von

Alexey Bushmelev

aus Nowosibirsk, Russische Föderation

Acknowledgments

Abstract

The subject of the present work is the synthesis of novel nanoscale objects, designed for self-propulsion under external actuation. The synthesized objects present asymmetric hybrid particles, consisting of a magnetic core and polymer flagella and their hydrodynamic properties under the actuation by external magnetic fields are investigated. The single-domain ferromagnetic cobalt ferrite nanoparticles are prepared by thermal decomposition of a mixture of metalorganic complexes based on iron (III) cobalt (II) in non-polar solvents. Further modification of the particles includes the growth of the silver particle on the surface of the cobalt ferrite particle to form a dumbbell-shaped heterodimer. Different possible mechanisms of dumbbell formation are discussed. A polyelectrolyte tail with ability to adjust the persistence length of the polymer, and thus the stiffness of the tail, by variation of pH is attached to the particles. A polymer tail consisting of a polyacrylic acid chain is synthesized by hydrolysis of poly(tert-butyl acrylate) obtained by atom transfer radical polymerization (ATRP). A functional thiol end-group enables selective attachment of the tail to the silver part of the dumbbell, resulting in an asymmetric functionalization of the dumbbells. The calculations on the propulsion force and the sperm number for the resulting particles reveal a theoretical possibility for the propelled motion. Under the actuation of the particles with flagella by alternating magnetic field an increase in the diffusion coefficient compared to non-actuated or non-functionalized particles is observed. Further development of such systems for application as nanomotors or in drug delivery is promising.

Kurzzusammenfassung

In dieser Arbeit wird die Synthese neuartiger Nanoobjekte, die für eine autonome Bewegung unter externer Aktuation konzipiert sind, behandelt. Diese Objekte liegen in Form asymmetrischer Partikel vor, die aus einem magnetischen Kern und Polymergeißeln bestehen. Die hydrodynamischen Eigenschaften dieser Objekte werden unter Aktuirung durch ein externes Magnetfeld untersucht. Die eindomänigen ferromagnetischen Cobaltferritnanopartikel werden durch thermische Zersetzung einer Mischung aus metallorganischen Eisen(III)- und Cobalt(II)-Komplexen in unpolaren Lösungsmitteln erhalten. Um im nächsten Schritt dumbbell-artige Heterodimere zu erhalten, erfolgt das Wachstum von Silberpartikeln auf der Oberfläche der Cobaltferritnanopartikel. Die verschiedenen möglichen Formationsmechanismen der Dumbbellbildung werden diskutiert. Polyelektrolytgeißeln, deren Persistenzlänge und somit die Steifigkeit der Ketten durch den pH-Wert der Lösung eingestellt werden kann, werden an die Dumbbells gebunden. Der aus Polyacrylsäure bestehende Polymerschwanz wird durch Hydrolyse von Poly(tert-Butylacrylat) erhalten, welches mittels Atom Transfer Radical Polymerization (ATRP) synthetesiert wird. Eine funktionelle Thiol-Endgruppe sorgt für eine selektive Bindung der Polymerketten an die Silberpartikel. Die theoretischen Berechnungen der Antriebskräfte und „Sperm Numbers" ergibt die Wahrscheinlichkeit einer angetriebenen Bewegung der Partikel. Experimentell ist eine Erhöhung des Diffusionskoeffizienten im Wechselfeld im Vergleich zu unfunktionalisierten Partikeln und Partikeln in Abwesenheit eines magnetischen Feldes zu beobachten. Eine weitere Entwicklung dieser Systeme als Nanomotoren oder für den Arzneimitteltransport im Organismus ist vielversprechend.

Table of Contents

Index of abbreviations

d_{Ag}	diameter of silver particle
$d_{CoFe_2O_4}$	diameter of cobalt ferrite particle
$\rho_{CoFe_2O_4}$	density of cobalt ferrite
ΔF^{*}	nucleation barrier
ΔF^{*}_{Homo}	homogeneous nucleation energy
ΔG_S	Gibbs free surface energy
μ_0	vacuum magnetic permeability
$\mu_{CoFe2O4}$	mass content of cobalt ferrite
μ_I	ionic strength
A	exchange constant
a	crystal lattice parameter
AC	alternating current
Ac	acetate
acac	acetylacetonate
a_{CC}	number of C-C bonds per monomer
Ag@CoFe$_2$O$_4$	Ag/cobalt ferrite particle
AIBN	azobisisobutyronitrile
ATRP	atom transfer radical polymerization
b	crystal lattice parameter
B	magnetic flux density
C	concentration
CA	citric acid
C_c	critical concentration

C_e	equilibrium concentration
C_E	energy conversion constant
CFA	cobalt ferrite synthesized from oleate complexes
CFO	cobalt ferrite synthesized from acetylacetonate complexes
$CoFe_2O_4$	cobalt ferrite
d	doublet
d	diameter
D	diffusion coefficient
d_0	single-domain-multidomain transition diameter
d_{AC}	hydrodynamic diameter measured by AC susceptometry
DDLS	depolarized dynamic light scattering
d_h	hydrodynamic diameter
DLP	dumbbell-like particle
DLS	dynamic light scattering
d_{mag}	magnetic core size
D_{rot}	rotational diffusion coefficient
d_S	superparamagnetic-ferromagnetic transition diameter
D_t	translational diffusion coefficient
EA	elemental analysis
ESI	electron spectroscopy imaging
et al.	et altera
EtOH	ethanol
F	force
F_0	propulsion force
F_c	number of polymer chains per particle

Fe_3O_4	magnetite
f_S	content of thiol-functionalized polymer chains
F_S	surface polymer density
FTIR	Fourier-transformed infrared
GPC	gel permeation chromatography
H	magnetic field strength
H_c	coercivity
HPLC	high-performance liquid chromatography
IR	infrared
K	magnetocrystalline anisotropy constant
k	Debye-Hückel screening length
K_{ATRP}	atom transfer radical polymerization rate constant
k_B	Boltzmann constant
k_d	deactivation rate constant
k_p	polymerization rate constant
k_S	stiffness
$K\alpha$	K-alpha line
L	length
l_B	Bjerrum length
l_{CC}	length of C-C bonds
l_e	electrostatic persistence length
l_g	Gaussian chain length
l_k	Kuhn length
l_P	persistence length
LSM	light scattering microscopy
m	multiplet

m	magnetic moment
M	magnetization
MBrP	methyl-2-bromopropionate
M_n	number average molar mass
m_p	polymer mass
M_r	remanence magnetization
M_S	saturation magnetization
MSD	mean squared displacement
M_w	weight average molar mass
n_0	refractive index
N_b	number of Kuhn monomers
N_{CC}	number of C-C bonds
N_d	number of dumbbell-like particles
NMR	nuclear magnetic resonance
N_p	number of polymer chains
p	pressure
P	monomer conversion
P(t-BuA)	poly(tert-butyl acrylate)
PAA	polyacrylic acid
PAA-SH	polyacrylic acid thiol
PDI	polydispersity index
PEG	poly(ethylene glycol)
PEG-SH	poly(ethylene glycol) monomethyl ether thiol
Pe_{rot}	rotational Péclet number
Pe_{trans}	translational Péclet number
PMDETA	N,N,N′,N″,N″-pentamethyldiethylenetriamine

ppm	parts per million
PTFE	polytetrafluoroethylene
q	scattering vector
q_c	electric charge
r	radius
Re	Reynolds number
r_{eff}	effective median radius
R_g	radius of gyration
R_{gl}	radius of gyration of a rod-like chain
R_{gr}	radius of gyration of a linear chain
r_h	hydrodynamic radius
R_{max}	contour length
R_p	polymerization rate
s	singlet
S_N2	nucleophilic substitution second order
S_p	sperm number
T	temperature
t	time
TEM	transmission electron microscopy
tert-BuA	tert-butyl acrylate
TFA	trifluoroacetic acid
THF	tetrahydrofuran
u	velocity
UV-vis	ultraviolet-visible
v	kinematic viscosity
V	volume

$\tilde{V}$	hydrodynamic volume
V_f	velocity field
vh	vertical-horizontal
VSM	vibrating sample magnetometry
vv	vertical-vertical
WLC	worm-like chain
XRD	X-Ray diffractometry
α	anomalous diffusion exponent
α_L	Langevin parameter
β	bead effectiveness
γ	interfacial energy
Γ	decay rate
δ	chemical shift
ε	misfit parameter
η	dynamic viscosity
Θ	surface coverage
θ	scattering angle
θ_c	contact angle
θ_{CC}	tetrahedral angle between C-C bonds
λ	wavelength
ξ	friction coefficient
ρ	density
σ	standard deviation
σ_m	mobility
τ_B	Brownian relaxation time
τ_N	Néelian relaxation time

$\Phi_{\text{electrostatic}}$	screened Debye-Hückel potential
χ^*	complex magnetic susceptibility
χ_{ini}	initial susceptibility
ω	field frequency

1. Introduction

1.1. Propulsion and diffusion of nanoscaled objects

The controlled motion of nanoscale and microscale objects in liquid medium is of interest both fundamentally and for numerous potential applications, such as invasive diagnosis and target therapies,[1–4] drug delivery,[5–7] environmental sensing and monitoring,[8–11] cell manipulation and analysis[12] and various micro- and nanodevices.[13]

The principle of motion involves Purcell's "scallop theorem", which states, that a reciprocal motion cannot lead to any net propulsion at low Reynolds numbers.[14] Out of it, various strategies of propulsion have been introduced. They can be divided into several groups. One group includes the motion based on phoretic effects, arising from a physical gradient in the medium, such as thermophoresis,[15–19] chemophoresis[20–23] or electrophoresis[24–26]. Such swimmers have been synthesized in a broad size range. Whereas most of the objects are on micrometer scale, particles of 30 nm able to propel themselves using chemophoresis have been reported.[22] The other group includes the propulsion by asymmetric movement of the object or its parts. Different types of propulsion have been introduced, such as motion of the magnetic filament[27] or motion of magnetic particles, functionalized with soft flagella. In general, two types of motion of such objects can be actuated by an magnetic field: flexible oar-like beats[1,27–30] and flexible[31–34] or helical[35–40] rotating propellers. The smallest systems of this kind are the magnetic helices of approximately 400 nm long as reported by Fischer, which can move only in highly viscous media.[36] Otherwise, the size of the magnetic helices, able to show a directed motion in water are theoretically limited by 900 nm.[41] The systems, based on undulating oar-like movements of the flagella are less common and are present only at microscale. These systems can be subdivided in two groups: objects, where the filament itself shows magnetic properties,[27] and objects consisting of a magnetic bead

and a flexible polymer flagellum or flagella attached to it.[29,42] The motion of both types of systems has been simulated numerically to model the influence of different parameters on the propulsion.[43–49]

An important dimensionless parameter for the flagellum, which characterizes the relative magnitudes of the viscous and bending forces, is the sperm number (S_p).

$$S_p = \left(\frac{l^4 \cdot \omega \cdot \xi}{k} \right)^{\frac{1}{4}} \qquad \textbf{(1-1)}^{[45]}$$

where l is the length of the flagellum, ω is the frequency of the AC field, k is the stiffness of the flagellum, ξ is the friction coefficient of the flagellum. When the stiffness of the flagellum is very high, the S_p goes to zero, and the swimming speed and efficiency go to zero, as predicted by scallop theorem. At very high S_p values a plateau region is expected, where the speed and the efficiency of swimming become independent of sperm number. The sperm number characterizes the effectiveness of the tail. For large sperm numbers the propulsive force is then

$$F_0 = 0.01 \cdot d^2 \cdot L^4 \cdot \frac{\omega^2}{k_B \cdot l_p \cdot T} \cdot \xi^2 \qquad \textbf{(1-2)}^{[50]}$$

Where d is the diameter of the bead, k_B is the Boltzmann constant, T is the temperature, ω is the frequency of the magnetic field. In equation (**1-2**) $k_B \cdot l \cdot T$ denotes the tail's bending modulus. To characterize the effectiveness of the magnetic bead another dimensionless parameter β is introduced.

$$\beta = \frac{m \cdot B}{\pi \cdot \eta \cdot \omega \cdot d^3} \qquad \textbf{(1-3)}^{[50]}$$

Where m is the magnetic moment of the bead, B is the external magnetic field, η is the viscosity of the dispersant. This parameter characterizes the effectiveness of the magnetic bed. It reflects the competition between the magnetic torque on the bead and viscous friction.

A steady flow past a body is described by equation (**1-4**)

$$(V_\text{f} \cdot \nabla)V_\text{f} = -\nabla\left(\frac{p}{\rho}\right) + v\Delta V_\text{f}$$

(**1-4**)[51]

Where V_f is the velocity field, p is the pressure, ρ is the density and v is the kinematic

viscosity. For a body with the size L a dimensionless quantity, called the Reynolds number

(Re), can be formed.

$$Re = \frac{u \cdot L}{v} = \frac{\rho \cdot u \cdot L}{\eta}$$

(**1-5**)[51]

Where u is the velocity of the object relative to the fluid, η is the dynamic viscosity. Reynolds

number is an important parameter determining the ratio of the nonlinear (inertial) term

$(V \cdot \nabla)V$ to the viscous friction term $v\Delta V$. For the systems with very low Reynolds numbers

the Navier-Stokes equation can be reduced to

$$-\nabla p + \eta\nabla^2 u = 0$$

(**1-6**)[14]

meaning that the inertia term can be neglected. When the Reynolds numbers are low, the

viscous forces dominate and diffusion takes place. At low Reynolds numbers the velocity of

the particle is proportional to the external force F:

$$v_0 = \sigma_\text{m} \cdot F$$

(**1-7**)

The coefficient of proportionality σ_m is known as the mobility. For spherical particles with

radius r the mobility is inverse to the Stokes drag coefficient:

$$\frac{1}{\sigma_m} = 6 \cdot \pi \cdot \eta \cdot r$$

(**1-8**)[52]

The diffusion coefficient is then the ratio between the thermal energy and the Stokes drag

coefficient. For spherical particles with radius r diffusion coefficient is calculated using the

Stokes-Einstein equation:

$$D_{t} = \frac{k_{B} \cdot T}{6 \cdot \pi \cdot \eta \cdot r}$$
$$\textbf{(1-9)}^{[53]}$$

Though both diffusion and propulsion of the nanoscaled particles have been described by a number of theoretical models, experimental data covers only a small part of the proposed self-propelling objects.

1.2. Formation of the nanoparticles

LaMer has described one ideal formation mechanism of monodisperse nanocrystals by separating the nucleation and the growth steps in the homogeneous nucleation process.[54] A non-seeded growth of monodisperse nanocrystals by thermal decomposition of metallorganic synthetic precursors is consistent with this formation mechanism. As shown on **Figure 1-1**, the monomer concentration is rising in the prenucleation stage (stage I) due to decomposition of the precursor. The concentration of the monomers passes then the equilibrium concentration (C_e) without nucleation of nanocrystals because of the unfavorable supersaturation condition. The monomer concentration continues to increase with time until reaching a critical nucleation concentration (C_c), at which initial nucleation of the nanocrystals (stage II) starts. The monomer undergoes "burst-nucleation" which reduces the concentration of free monomers in solution. The rate of this nucleation is described as "effectively infinite" and after this point, there is almost no nucleation occurring due to the low concentration of monomers after this point. When the monomer concentration in stage II is finally below C_c, the growth stage begins (stage III). The nuclei of stage II grow steadily in stage III by incorporating additional monomers until their concentration drops below C_e. The variation of the parameters, such as concentration, temperature and heating rate are of sensitive influence on the size and the monodispersity of the resulting nanoparticles.
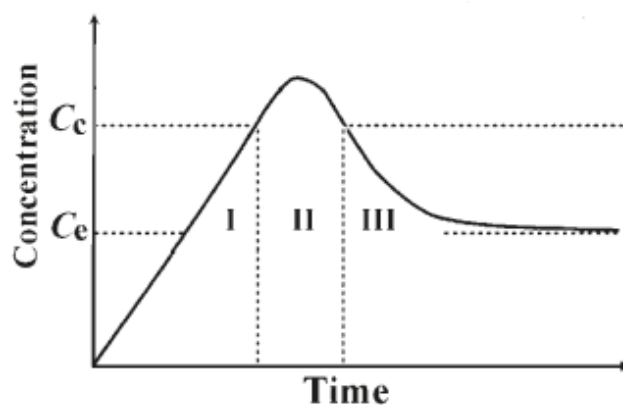
Figure 1-1. LaMer mechanism of the nanoparticles nucleation and growth (illustration taken from N. Bao[55]).

Ostwald ripening was first described in 1900.[56] This mechanism of growth consists in redissolving of smaller particles within the solution due to their higher solubility and surface energy and further growing of the larger particles. The mathematical model of Ostwald ripening was presented by Lifshitz and Slyozov.[57] Coalescence and oriented attachment are other growth mechanisms. While being similar in mechanism, they differ in the orientation of the grain boundary. Whereas for coalescence there is no particular preference for the attachment,[58] for the oriented alignment there is a common crystallographic alignment of the attachment, allowing continuous crystallographic planes.[59]

The cubic spinel structures, such as $M^{2+}Fe_2O_4$ or $MO \cdot Fe_2O_3$ (where M^{2+} is Fe, Co, Ni, Zn, Mn, Cu etc)[60–65] are a well-known class of iron oxides, where oxygen forms an fcc close packing, and M^{2+} and Fe^{3+} occupy either tetrahedral or octahedral interstitial sites.[66] The synthetic approaches towards the spinel-structured magnetic nanoparticles include sol-gel method,[67–69] alkaline precipitation[70–73] as well as methods based on the thermal decomposition of the metal organic complexes, such as oleate complexes[55,74] or acetylacetonate complexes.[66,75,76]

The growth of the silver nanoparticles has been thoroughly explored, however the information on the nucleation of such nanoparticles is still lacking.[77] Depending on the

reaction conditions the growth mechanism of silver particles can be different. Henglein et al.[78] reports that if the Ag particles are lacking the stabilizing citrate ligand, coalescence as a major growth pathway occurs. In case of high concentrations of sodium citrate, the ionic strength of the solution destabilizes the particles, making the growth over the reduction of the silver ions on the surface of the particles preferable. Harada and Takagiri investigated the photoreduction of the silver precursor.[79] The formation of the silver nanoparticles consisted of two steps: autocatalytic reduction-nucleation, which is itself a two-step process,[80] followed by Ostwald ripening. Richards et al.[81] reported the reaction of $[(PPh_3)_2Ag(O_2CC_{13}H_{27})]$ with AIBN to be a three-step process: LaMer nucleation was followed by coalescent growth and then Ostwald ripening took place.

An expansion to multi-component hybrid structures provides several advantages that are unavailable for single-component nanoparticles system. The first advantage is the combination of properties characteristic for each of the components. For the particles consisting of a magnetic counterpart and a noble metal counterpart it is the combination of magnetic and optical properties [82–85] or catalytic properties.[86,87] Amphiphilicity can also be considered as such a combination: counterparts with different surface properties lead to the so-called Janus particles.[88–90] Another important advantage is the enhancement of the physical properties of the single components, such as magnetic response[91] or magnetooptical response of the $Ag@CoFe_2O_4$ particles.[92] The third advantage is providing the physical properties unavailable for single-component systems. Breaking the symmetry is one of such examples.[88,89,93–95]

The formation of a multi-component hybrid includes creation of the interface between chemically and structurally different materials. The shape of the resulting hybrid depends on the sign of the total Gibbs free surface energy ΔG_S (see equation (**1-10**)).

$$\Delta G_S = \gamma_1 - \gamma_2 + \gamma_{1,2}$$

(**1-10**)

Where γ_1 and γ_2 are the solid/liquid interfacial energies for primary and secondary material and $\gamma_{1,2}$ is the solid/solid interfacial energy. If $\gamma_1 > \gamma_2$ and $\gamma_{1,2}$ is small (which is likely for materials that more or less match crystallographically), then $\Delta G_S > 0$ and the deposition will take place layer-by-layer, resulting in a core-shell structure (Frank - van der Merwe model),[96] as shown on On the contrary, if $\gamma_1 < \gamma_2$ (secondary material has higher energy surfaces) and $\gamma_{1,2}$ is high (due to lattice mismatch), then $\Delta G_S < 0$ and deposition will take a discontinuous island-like domain array character to minimize the overall interfacial area between the two materials (Volmer-Webber model). An intermediate case includes a two-mode deposition regime. In the beginning, a core-shell structure is being formed ($\Delta G_S > 0$). After reaching the critical thickness of the layer, a segregation to discrete arrays takes place ($\Delta G_S < 0$) as a sequence of the intensification of the interfacial strain fields (Stranski-Krastanov model). This process can't be fully explained on purely surface energetic grounds. Three-dimensional islands gain a decrease in the volume energy, compared to a thin film. This is characteristic for lattice mismatched systems, where relaxation of elastic stress induced by the mismatch is the driving force for transition from two-dimensional to three-dimensional growth. If the islands are mobile, the can encounter each other and coalesce into larger islands (Smoluchowski ripening). [97]
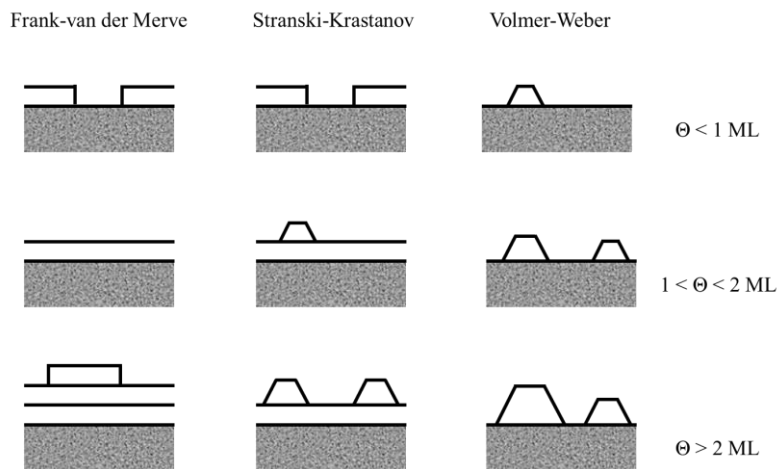
Figure 1-2. Schematic presentation of different growth modes (reproduced from [98]). Θ is the surface coverage.

To quantify the lattice mismatch, the misfit parameter (ε) is introduced, defined as the relative difference of lattice constants (a, b):

$$\varepsilon = \frac{b - a}{a}$$

$(1\text{-}11)$

Relatively low misfits can be accommodated in such a way, that the strained film adopts the periodicity of the primary material in the interfacial plane, but can be distorted in the perpendicular direction to preserve the volume of the unit cell (**Figure 1-3**). This kind of growth is called pseudomorphic growth.[98]
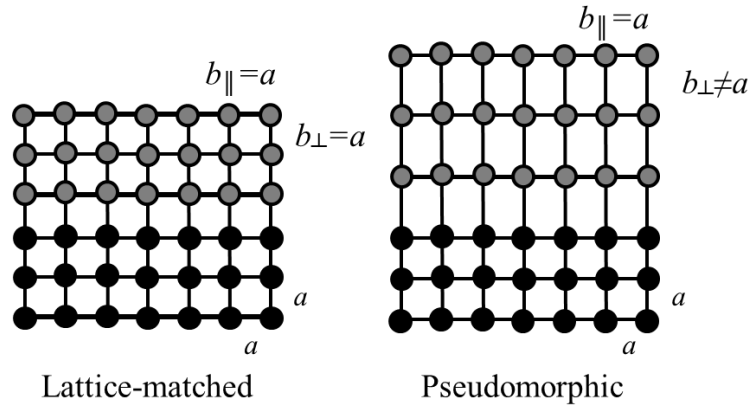
Figure 1-3. Schematic presentation of lattice-matched and strained pseudomorphic growth (reproduced from [98]**).**

Heterogeneous nucleation or seed-growth nucleation is described in terms of Classical Nucleation Theory. For a smooth infinite plane with a uniform surface the equation derived by Volmer is

$$\Delta F^* = \Delta F^*_{\text{Homo}} f(\theta_c)$$

$(1\text{-}12)$

Where ΔF^* is the nucleation barrier and ΔF^*_{Homo} is the homogeneous nucleation energy. The function $f(\theta_c)$ of the contact angle θ_c is derived as

$$f(\theta) = \frac{1}{2} - \frac{3}{4}\cos(\theta_c) + \frac{1}{4}\cos^3(\theta_c)$$

$(1\text{-}13)^{[99]}$

Despite a large theoretical background about heterogeneous nucleation, data on formation of dumbbell-like particles is still scarce and none of the models has been approved.

1.3. Magnetic nanoparticles

Magnetic nanoparticles below a critical diameter cannot support more than one domain, and are thus called single-domain nanoparticles. The critical diameter is approximately $2A^{1/2}/M$, where A is the exchange constant and M is magnetic moment per unit volume.[100] A particle above this critical diameter exhibits hysteresis properties similar to multidomain particles, but are capable of having remanence and coercivity similar to those of single-domain grains. Such particles are denoted as pseudo-single-domain.[101] A dispersion of magnetic nanoparticles will have a superparamagnetic character in case that there is no interaction between them. The magnetic behavior of the dispersion can thus be described by Langevin's equation for the magnetization of paramagnetic systems:

$$M = M_S \left(ctgh\alpha_L - \frac{1}{\alpha_L} \right)$$

(1-14)[102]

Where M is the magnetization of the ferrofluid, M_S is the saturation magnetization, and α_L is the parameter, called Langevin parameter, denoting the relation between the thermal energy of the particle and its energy in the magnetic field H.

$$\alpha_L = \frac{\mu_0 \cdot m \cdot H}{k_B \cdot T}$$

(1-15)[102]

Where μ_0 is the magnetic vacuum permeability. For large magnetic fields, where saturation magnetization is reached, equation **(1-14)** can be approximated by

$$M = M_S \left(1 - \frac{1}{\alpha_L} \right) = M_S \left(1 - \frac{k_B \cdot T}{\mu_0 \cdot m \cdot H} \right)$$

(1-16)[102]

Thus, the saturation magnetization can be read from the magnetization at high field values. For weak magnetic fields, the Langevin equation can be approximated by

$$M = \frac{1}{3} M_S \frac{\mu_0 \cdot m \cdot H}{k_B \cdot T} \qquad \textbf{(1-17)}^{[102]}$$

Since for weak magnetic fields $\chi_{ini} = \left(\frac{M}{H}\right)_{H \to 0}$, where χ_{ini} is the susceptibility of the virgin curve (called initial susceptibility), from equation **(1-17)** can be derived

$$\chi_{ini} = \frac{1}{3} \frac{M_S \cdot m \cdot \mu_0}{k_B \cdot T} \qquad \textbf{(1-18)}^{[102]}$$

Chantrell[103] has shown, that assuming that particles have a log-normal distribution allows calculating the size distribution of the particles by fitting

$$M = M_S \int_0^\infty L(\alpha) f(y) dy \qquad \textbf{(1-19)}^{[102]}$$

Where $y = \frac{d}{\bar{d}}$ denotes a normalized particle diameter, *f(y)* represents the mentioned log-normal size distribution in the form

$$f(y) = \frac{1}{y \cdot \sigma \cdot \sqrt{2\pi}} e^{\frac{-(\ln y)^2}{2\sigma^2}} \qquad \textbf{(1-20)}^{[102]}$$

Where σ is the width of the distribution.

The relaxation of magnetization can occur in two different ways: the so-called Brownian relaxation lies in the rotation of the whole particle with the magnetic moment being fixed relative to the particle. The respective relaxation time (τ_B) is defined as

$$\tau_B = \frac{3\tilde{V} \cdot \eta}{k_B \cdot T} \qquad \textbf{(1-21)}^{[102]}$$

Where $\tilde{V}$ the hydrodynamic volume of the particle, η is the dynamic viscosity of the dispersant.

The other case is the relaxation via rotation of the magnetic moment relative to the crystal structure of the particle without the rotation of the particle itself. This relaxation is called Néelian relaxation and is characterized by the energy barrier the magnetic moment has to overcome to flip relative to the crystal structure. The Néel relaxation time is calculated as

$$\tau_N = f_0^{-1} e^{\frac{K \cdot V}{k_B \cdot T}} \qquad\qquad \textbf{(1-22)}^{[104]}$$

Where K is the anisotropy constant of the particle, V is the volume and f_0 is the Larmor frequency of the magnetic moment in the anisotropy field of the particle. The magnetic relaxation behavior is then dominated by the process with the smaller relaxation time. The smaller particles, where relaxation occurs by Néel mechanism are called magnetically soft. The particles, where Brownian relaxation becomes faster than the Néel process are called magnetically hard particles. The critical size, at which the transition from one mechanism to another takes place, is dependent on the viscosity of the dispersant and on the anisotropy constant of the magnetic material.

Hard magnetic materials are characterized by high coercivities and high remanent magnetizations. If the magnetization M of a hard magnetic material in its solid state is plotted against the applied field H a hysteresis loop will be obtained in which magnetization depends on the direction and magnitude of previously applied fields. The initial magnetization (virgin curve) is obtained when the material is in thermally demagnetized state. When the magnetic field is sufficient to saturate the material the loop is referred to as a saturation loop and the magnetization is called saturation magnetization (M_S). When the applied magnetic field is removed, the magnetization decreases to a remanent magnetization M_r, which is generally less, than M_S. If demagnetizing field is applied the magnetization is gradually reduced and at a critical field value the magnetization is zero. This critical field is known as coercive field (H_c) and is defined as the reverse field required to reduce the net magnetization of the

material to zero in the presence of the field. If the field is removed however the specimen might return to a small positive remanent magnetization.[105]
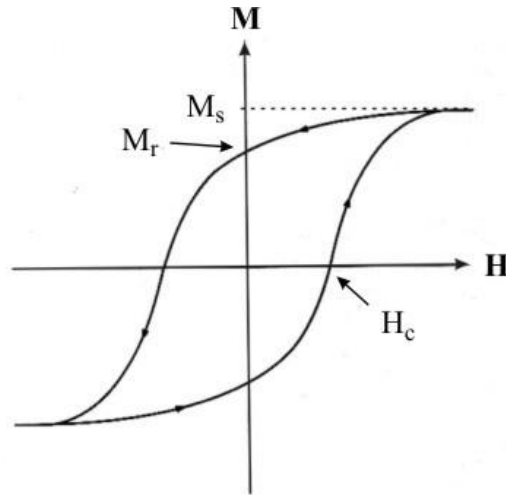
Figure 1-4. Example of the magnetic hysteresis loop (taken from[106]**).**

The superparamagnetic particles, in which Néel relaxation times are small and magnetization can randomly flip direction under the influence of temperature, are characterized by zero remanence and zero coercive field. Single-domain particles larger than d_S (superparamagnetic – ferromagnetic transition size) have a theoretical remanence magnetization $M_r = \frac{1}{2}M_S$ until reaching d_0 (single-domain – multidomain transition size), at which remanence magnetization drops.[107] The size range between d_S and d_0 can be rather narrow, the approximate values are given on **Figure 1-5**.
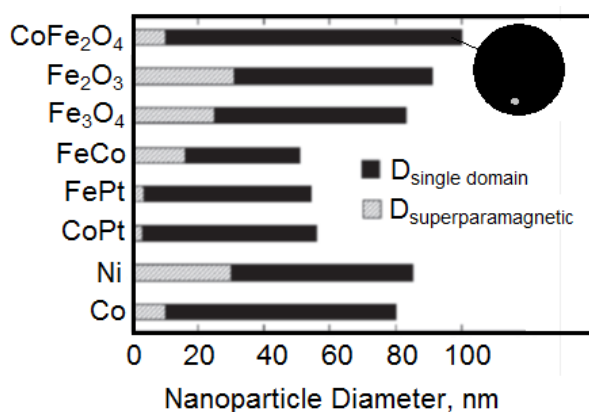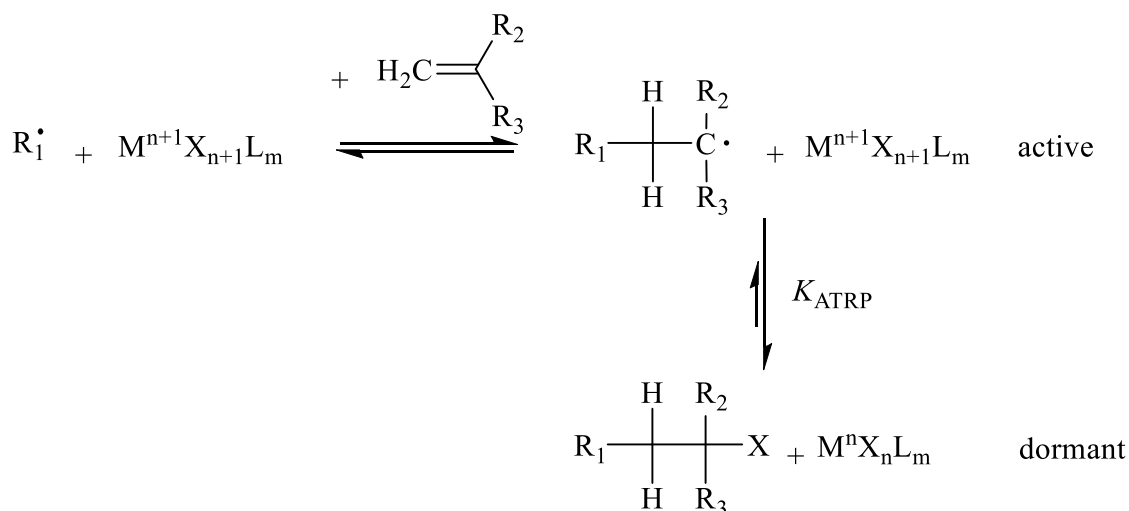
Figure 1-5. Size ranges of d_S and d_0 for different materials (illustration taken from [108]).

1.4. Polyelectrolytes

Flagella, mentioned in **Chapter 1.1** consist of polymers. A polymer molecule is a molecule of high relative molecular mass, the structure of which essentially comprises the multiple repetition of units derived, actually or conceptually, from molecules of low relative molecular mass.[109] One of the synthetic approaches towards polymer chains is atom transfer radical polymerization (ATRP), which is a living radical polymerization discovered and investigated by Krzysztof Matyjaszewski in 1995.[110] The initiation of the reaction occurs via a redox reaction between an alkyl halide and a complex of a transition metal, serving as a catalyst.

$$R\text{-}X \ + \ M^n X_n L_m \ \rightleftharpoons \ R^{\cdot} \ + \ M^{n+1} X_{n+1} L_m$$
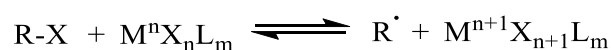
The emerging alkyl radical starts the polymerization, and the halogen atom is transferred to the oxidized transition metal complex. First, the addition of a monomer to an alkyl radical takes place. The product of the reaction is in equilibrium with the halogenated form, which doesn't react further with monomers, since there is no free radical. These forms are called active and dormant species respectively. The metal is reduced during the deactivation of the radical and the halogen is transferred to the chain.

$$R_1^{\bullet} \; + \; M^{n+1}X_{n+1}L_m \; \underset{+ \; H_2C=\overset{R_2}{\underset{R_3}{\diagdown}}}{\rightleftharpoons} \; R_1 \underset{H}{\overset{H}{-}} \underset{R_3}{\overset{R_2}{\underset{|}{\overset{|}{C}}}}{}^{\bullet} \; + \; M^{n+1}X_{n+1}L_m \quad \text{active}$$

$$\Big\updownarrow K_{\text{ATRP}}$$

$$R_1 \underset{H}{\overset{H}{-}} \underset{R_3}{\overset{R_2}{-}} X \; + \; M^n X_n L_m \qquad \text{dormant}$$

Chain growth takes place via the addition of the monomers to the free radicals of the chain. After each addition the equilibrium is established. The reaction continues until the monomer supply exhausts.

$$R_1 \underset{H}{\overset{H}{-}} \underset{R_3}{\overset{R_2}{\underset{|}{\overset{|}{C}}}}{}^{\bullet} \; + \; M^{n+1}X_{n+1}L_m \; \underset{+ \; \text{n-1} \; H_2C=\overset{R_2}{\underset{R_3}{\diagdown}}}{\rightleftharpoons} \; R_1 {\left[\underset{H}{\overset{H}{-}} \underset{R_3}{\overset{R_2}{-}} \right]}_n{}^{\bullet} \; + \; M^{n+1}X_{n+1}L_m$$

$$\Big\updownarrow K_{\text{ATRP}}$$

$$R_1 {\left[\underset{H}{\overset{H}{-}} \underset{R_3}{\overset{R_2}{-}} \right]}_n X \; + \; M^n X_n L_m$$
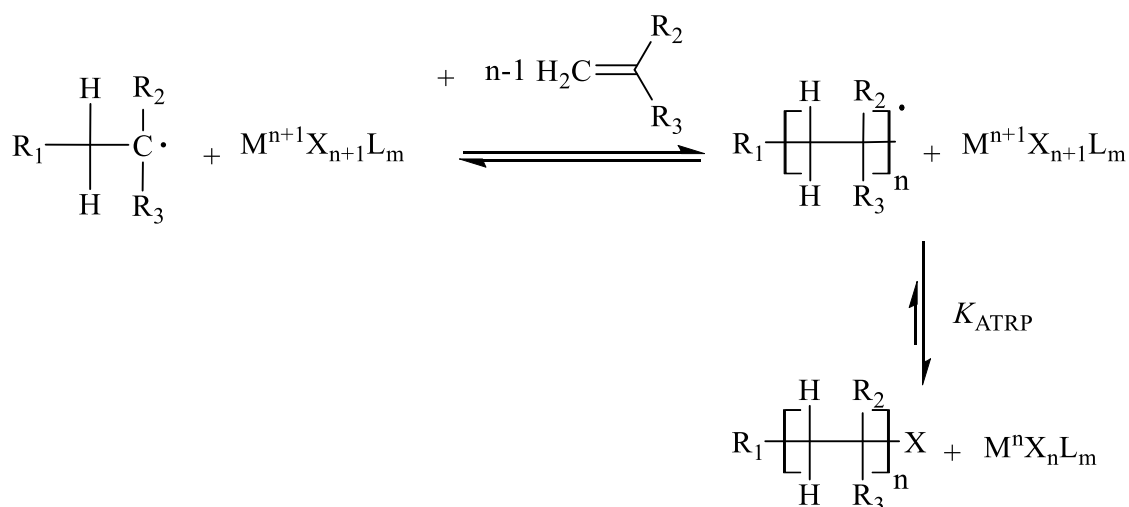
Since all the chains are growing simultaneously, ATRP is characterized by a narrow size distribution. The equilibrium is shifted towards the dormant form, so the concentration of free radicals remains low throughout the reaction and recombination is rather unlikely. Matyjaszewski et al. investigated the details of the reaction.[111–114] It was found, that the number of the initiator molecules defines the number of the growing chains and the molar mass can be controlled over the ration between the initiator and the monomer. Quick

initiation is preferred to keep the polydispersity low. The halogen atom needs to have a certain mobility to move between the catalyst and the growing chain. Bromine and chlorine give the best fit. The position of the halogen atom at α-carbon of an aryl, alkyl or carbonyl group is favorable. All compounds containing a vinyl group, where the substituents stabilize the forming radical, are suitable as monomers for polymerization. Copper, iron and ruthenium based catalysts are usually used. It is important, that the metal atom is stable in two oxidation levels differing by one. Furthermore, a certain affinity to the halogen atom is required. This is important for quick deactivation of the free radicals and activation of the dormant chains. The catalysts are usually present in form of a metal complex, in which the ligand serves as a stabilizer and increases the solubility of the catalyst in organic solvents. The polydispersity index (PDI) of a polymer is calculated as following:

$$PDI = \frac{M_\mathrm{w}}{M_\mathrm{n}} = 1 + \left(\frac{[PX] \cdot k_\mathrm{p}}{k_\mathrm{d}[M^{n+1}X_{n+1}L_m]} \right) \left(\frac{2}{P} - 1 \right) \tag{1-23}$$

Where M_w is the weight average molar mass, M_n is the number average molar mass, $[PX]$ is the concentration of the dormant species, k_p is the polymerization rate constant, k_d is the deactivation rate constant, $[M^{(n+1)}X_{n+1}L_m]$ is the concentration of the oxidized metal complex, P is the monomer conversion.

The polymerization rate (Rp) is then

$$R_\mathrm{p} = \frac{-d[Mo]}{dt} = k_\mathrm{p}[Mo][P^\cdot] = k_\mathrm{p} \cdot K_\mathrm{ATRP} \frac{[Mo][PX][M^n X_n L_m]}{[M^{n+1}X_n L_m]} \tag{1-24}$$

Where $[Mo]$ is the concentration of the monomer, $[P^\cdot]$ is the concentration of the active species, K_ATRP is the ratio between k_p and k_d, $[M^n X_n L_m]$ is the concentration of the catalyst.

A polyelectrolyte is a polymer, composed of polyelectrolyte molecules, i. e. macromolecules in which a substantial portion of the constitutional units have ionizable or ionic groups or both.[115] The effects of coulomb repulsions between the ionized groups in such polymers are

strong and can be rather complex. Thus, the polyelectrolytes can be considered as stretched electrostatic blobs in dilute solutions. The electrostatic blob is defined as the typical size at which the conformation of the chain starts being perturbed by the electrostatic interactions between the monomers.[116] The stretching of the chain is maximal, when the polymer is 100% deionized. Further addition of the base has the same effect as of an addition of a salt: higher concentration of ions in the solution lowers the electrostatic repulsion along the chain by electrostatic shielding and the chain conformation becomes more coiled.[117]

Solutions of polyelectrolytes show unusual correlation between the viscosity of the solution and the concentration of the polymer. The viscosity increases with decreasing concentration of the polymer, till it drops again at very small concentrations. The increase of the viscosity is attributed to increasing dissociation and electrostatic repulsion between the ionic groups.[117]

The electrostatic interactions in polyelectrolytes are described by polyelectrolyte theory using the Debye-Hückel potential and introducing the screening effect of the surrounding local charges (equation (**1-25**)).[118]

$$\Phi_{\text{electrostatic}} = C_{\text{E}} \frac{q_{ci} \cdot q_{cj}}{r_{ij}} \cdot e^{-kr_{ij}}$$

(**1-25**)[119]

Where C_{E} is the energy conversion constant, q_{ci} and q_{cj} are the electric charges on two objects, r_{ij} is the distance between the charges, k^{-1} is the Debye-Hückel screening length. $\Phi_{\text{electrostatic}}$ is referred to as screened Debye-Hückel potential. The screening length is a function of charge density and is defined as the distance by which the action of an electric field of a separate charge placed in the medium containing other charges is spread:

$$k^{-1} = (8\pi \cdot l_{\text{B}} \cdot \mu_{\text{I}})^{1/2}$$

(**1-26**)[119]

Where l_{B} is the Bjerrum length, characterizing the screenin action of the solvent, μ_{I} is the ionic strength of the solvent.

The persistence length l_p describes the stiffness of the polymer chain, i.e. the maximum length, at which the polymer can be considered inflexible. It can be calculated from the so-called Worm-like Chain Model (WLC). To stretch a worm-like chain with length L_0 to length x, force F is required. In range of $F < 10$ pN F is a linear function of x. This function was derived by Bustamante et al.[120]

$$F = \frac{k_B \cdot T}{l_p} \left(\frac{1}{4 \cdot \left(1 - \frac{x}{L_0}\right)^2} - \frac{1}{4} + \frac{x}{L_0} \right)$$

(1-27)

In the case of polyelectrolytes the persistence length is a sum of two contributions, namely the intrinsic polymer length, arising from the rigidity of the polymer backbone, and the electrostatic persistence length, arising from the electrostatic repulsion of the adjacent ionic groups.[121] Odijk-Skolnick-Fixman theory considers a WLC characterized by its uncharged intrinsic persistence length, carrying uniform charges, separated by a distance a along its contour.[121,122] The electrostatic persistence length l_e, according to this model is then:

$$l_e = \frac{l_B}{4 \cdot k^2 \cdot a^2}$$

(1-28)[121]

Where l_B is the Bjerrum length. The persistence length of a polyelectrolyte can be defined differently and other models can be applied.[123] Though pH is not considered important for persistence length of the strong polyelectrolytes[124,125], for weak polyelectrolytes, such as polyacrylic acid or poly(allylamine hydrochloride) it plays a major role in varying the ionization and thus persistence length.[119]

2. Task

The aim of this thesis is to synthesize anisotropic nanoscale objects that are of potential for the autonomous motion actuated by an external alternating magnetic field and investigate their diffusion behavior under the influence of the torque caused by this field. These objects are designed as asymmetric particles consisting of a hard part with certain magnetic properties and of a soft part in a flagellum-like form. The magnetic part is present in form of a single-domain magnetic nanoparticle core with prevailing Brownian relaxation and oxidation stability for application in aqueous media. The influence of the reaction parameters, such as temperature and reaction time on the morphology of the resulting particles should be investigated to optimize the synthetic approach towards shape anisotropy as well as uniform size and shape distribution. The soft part is present as a polymer of a certain molecular mass with an adjustable rigidity of the chain and a functional group for selective attachment.

The measurements of the hydrodynamic properties should be performed in media with adjustable parameters, such as polarity, viscosity, pH. To characterize diffusion behavior of the particles, the diffusion coefficients and mean squared displacement should be quantified and the directionality of the movement should be detected to be able to characterize the type of the diffusion. Since the particles are to be actuated by an external alternating magnetic field, the optimal conditions should be found based on the theoretical calculations for the motion exploiting the undulating oar-like beats and taking in account the capability of the instrumentation facilities.

3. Concept

To achieve the aims, formulated in the previous chapter, the principle of the dimeric Janus particles, the so-called dumbbell-like particles (DLP) will be synthesized with further attachment of the polymeric tail via functional group. A schematic concept of the architecture evolution is presented on **Figure 3-1**. DLP is a particle, consisting of two smaller particles, in case of this work a ferromagnetic nanoparticle and a noble metal particle are implied.[87] There are two possible synthetic approaches towards such particles: a growth of the noble metal particle on the surface of a primary magnetic particle[85,87,91,126,127] and a growth of the magnetic particle on the surface of a primary noble metal particle.[86] Since the magnetic properties of the particles are important and tuning of these properties by variation of the reaction parameters for primary particle is more convenient, it is reasonable to apply the approach starting with the synthesis of the magnetic nanoparticles.
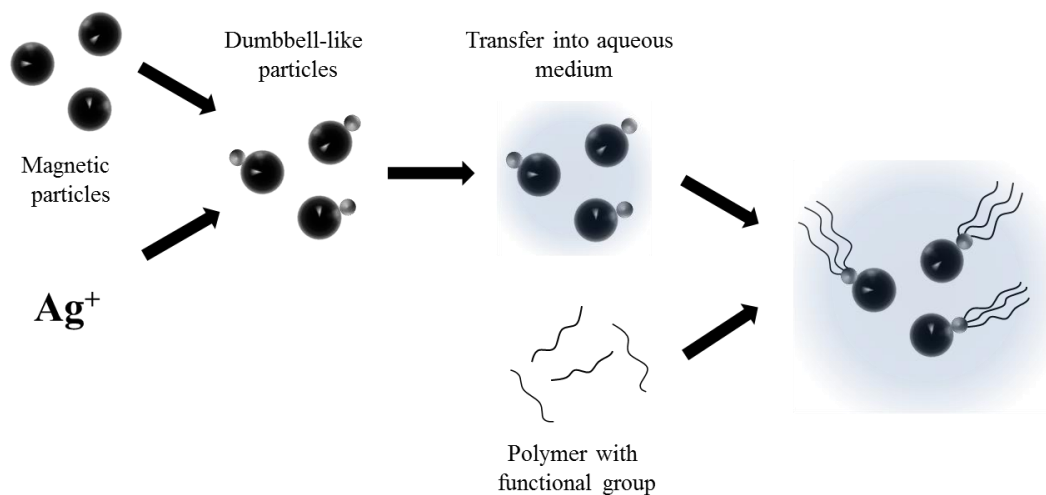
Figure 3-1. Schematic approach towards the magnetic particles with polymeric flagella.

A narrow size distribution of the magnetic nanoparticles is essential, since all the instrumentation methods suitable for the objects of such size range deal with the ensemble of the objects, rather than with the single ones. The magnetic nanoparticles will be synthesized

by the thermal decomposition of the complexes of metal ions with organic ligands. This method results in monodisperse nanoparticles with ability to tune the shape and the size of the resulting particles.[55,66,74–76] Cobalt ferrite ($CoFe_2O_4$) is proposed as a material for primary nanoparticles due to its high saturation magnetization,[128] magnetocrystalline anisotropy constant[129] and oxidation stability. The magnetic properties will be investigated by means of Vibrating sample magnetometry (VSM) and AC Susceptometry to obtain information on saturation magnetization, susceptibility, remanence and coercivity of the particles and characterize the relaxation of the magnetic moment in the particle.

The polymer flagella should show defined rigidity (characterized by the persistence length of the polymer) and possess a functional end-group for attachment to the magnetic counterpart. To obtain the structure, where the polymer chains serve as flagella and not as a brush on the surface of the particle, a point of asymmetry is required in the attachment of the polymer tail to the magnetic particle. For this purpose creation of the Janus particles with magnetic properties is required. Based on this, selective attachment of the polymer chains over the functional groups is necessary. For the polymeric tail the poly(tert-butyl acrylate) is proposed with further hydrolysis to polyacrylic acid for application in the aqueous media. This polymer can be synthesized by atom transfer radical polymerization (ATRP), characterized by conservation of the halogen group of the initiator transferred to the end of the polymer chain, in addition polymers synthesized by ATRP show narrow molecular mass distribution.[114] The polyelectrolyte nature of polyacrylic acid enables tuning the ionization degree of the chain, and thus the stiffness of the tail by variation of pH.[119]

Further modification of the particles involves an exchange of the surface group of the particles in order to transfer the particles into aqueous before the attachment of the polymeric tail.[76] Citric acid and polyacrylic acid are suggested as surface agents for electrostatic stabilization.

The asymmetric shape of the dumbbells along with the difference in physical and chemical properties of the magnetic particles and noble metal particles provides an opportunity for selective attachment of the polymeric tail with a definite functional group. The thiol group is known to have a high affinity to noble metals,[130] so a selective attachment to silver part is expected. The thiolization of the polymer can be performed by nucleophilic substitution of the polymer halogen end-group remaining after the polymerization. The magnetic properties of the particles can be exploited for purification of the particles dispersion from the unreacted polymer.

The particles synthesized according to the presented concept will be used for the measurement of their hydrodynamic properties in the external alternating magnetic fields. The information on the diffusion coefficients and diffusion behavior will be obtained by light scattering methods, such as dynamic light scattering (DLS) and light scattering microscopy (LSM). The instruments will be equipped with Helmholtz coils and a power supply unit to produce the alternating magnetic fields of various field strength and frequency. The LSM measurements are to detect the movement of the particles in the dispersion in a "live" mode and to reveal possible deviations in the diffusion behavior after the actuation by the magnetic field.
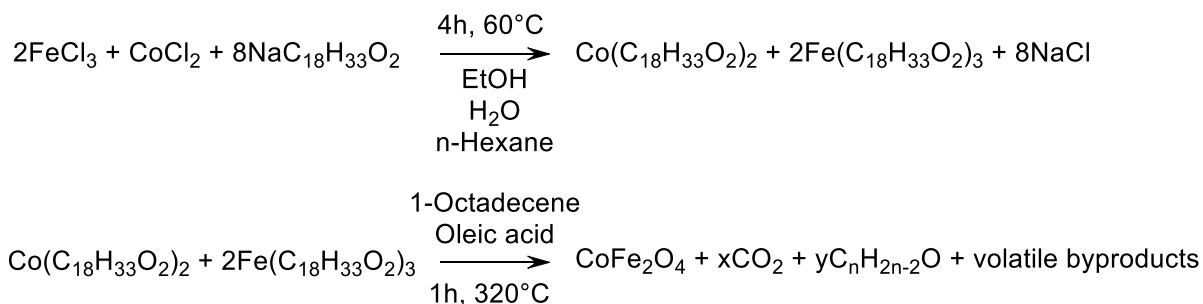
4. Synthesis of CoFe$_2$O$_4$ nanoparticles

In this chapter the synthesis of the primary magnetic nanoparticles is discussed. The goal is to obtain monodisperse ferromagnetic nanoparticles with defined hydrodynamic and magnetic properties. The cobalt ferrite (CoFe$_2$O$_4$) is considered to be most suitable for the set objectives due to its oxidation stability, high magnetocrystalline anisotropy constant (K_1=⊠20·10^4 J/m^3 for cobalt ferrite, compared to -1.1·10^4 J/m^3 for magnetite)[129] and high saturation magnetization (75.5 A·m^2·kg^{-1})[128]. The cobalt ferrite particles discussed here are synthesized by thermal decomposition of the mixture of iron and cobalt complexes with organic ligands. Two types of CoFe$_2$O$_4$ particles are being discussed in this chapter. The first species are the CoFe$_2$O$_4$ particles synthesized by decomposition of mixture of iron oleate and cobalt oleate (CFO). The second species are the particles synthesized by decomposition of mixture of iron acetylacetonate and cobalt acetylacetonate (CFA).

4.1. Synthesis of CoFe$_2$O$_4$ nanoparticles by thermal decomposition of iron oleate and cobalt oleate

This synthetic approach is based on the synthesis of mixture of iron oleate complex and cobalt oleate complex from corresponding chlorides and its subsequent decomposition.[55] The metal oleate complexes are prepared in a mixture of ethanol, hexane and water by reaction of metal chlorides with sodium salt of oleic acid. The dried mixture of iron oleate and cobalt oleate is then dissolved in 1-octadecene and heated up at a constant heating rate to a set temperature and held at this temperature for 1h. Since the decomposition undergoes the LaMer mechanism and subsequent Ostwald ripening[55], a proper control of the morphology is possible by controlling the reaction temperature, heating rate and reaction time. No investigation of the produced organic byproducts of this reaction can be found in literature. In general, metal carboxylate complexes decompose at temperature around 300 °C or higher to

produce a broad range of possible byproducts, such as CO, CO$_2$, H$_2$, H$_2$O, ketones, esters and various hydrocarbons.[131]

$$2FeCl_3 + CoCl_2 + 8NaC_{18}H_{33}O_2 \xrightarrow[\substack{EtOH \\ H_2O \\ n-Hexane}]{4h, 60°C} Co(C_{18}H_{33}O_2)_2 + 2Fe(C_{18}H_{33}O_2)_3 + 8NaCl$$

$$Co(C_{18}H_{33}O_2)_2 + 2Fe(C_{18}H_{33}O_2)_3 \xrightarrow[1h, 320°C]{\substack{1-Octadecene \\ Oleic\ acid}} CoFe_2O_4 + xCO_2 + yC_nH_{2n-2}O + volatile\ byproducts$$

To estimate the influence of the temperature on the morphology of the resulting particles, samples synthesized at constant heating rate 1 °C/min and temperatures of 310 °C, 315 °C and 320 °C are compared. The geometric size d and the shape of the resulting particles are investigated using Transition Electron Microscopy. The TEM images of the particles can be found on **Figure 4-1** and respective geometric size histograms on **Figure 4-2**. The geometric size of the cubic particles was measured along the face.

Table 4-1. Geometric sizes of the CoFe$_2$O$_4$ particles synthesized by oleate complex decomposition

Sample name	Synthesis temperature [°C]	Geometric size, d [nm]	σ
CFO-310	310	15.5	0.07
CFO-315	315	25.3	0.08
CFO-320	320	25.1	0.10

(a)　　　　　　　　　　(b)　　　　　　　　　　(c)
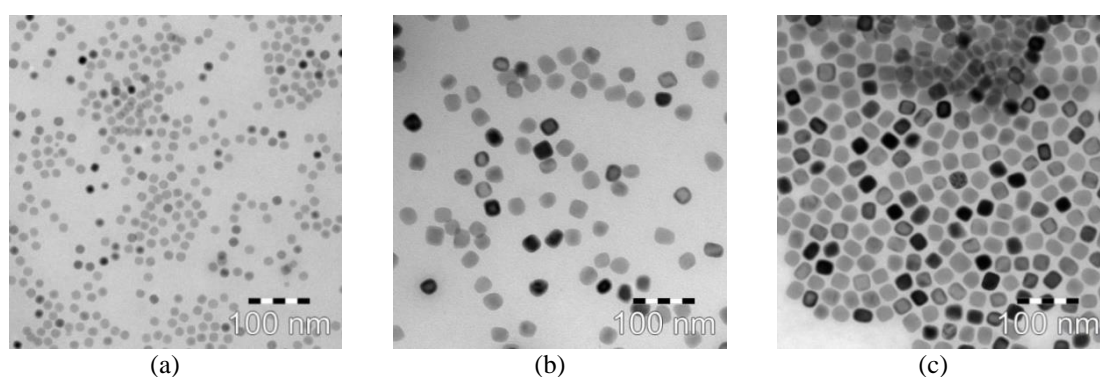
Figure 4-1. TEM images of CoFe$_2$O$_4$ samples CFO-310 (a), CFO-315 (b), and CFO-320 (c).
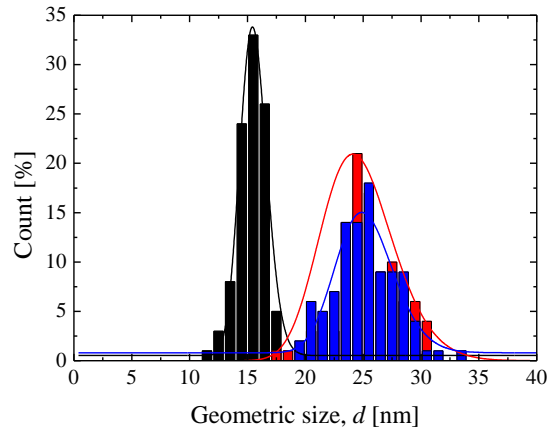
Figure 4-2. Size histograms of CoFe$_2$O$_4$ samples CFO-310 (black) CFO-315 (red) and CFO-320 (blue).

The histograms indicate an increase in the particles size between temperatures 310 °C and 315 °C, and no further growth between temperatures 315 °C and 320 °C. To characterize the change in the shape of the particles the aspect ratio, which is defined as a ratio between the particles diagonal (*a*) and its face length (*d*) is plotted against the reaction temperature (see **Figure 4-3**). For an ideal spherical particle all axes are equivalent, so the value of $\frac{a}{d}$ is obviously 1, and for an ideal cubic particle the value is $\sqrt{2}$, respectively. The **Figure 4-3** shows that the particles synthesized at 310 °C have an average aspect ratio of less than 1.1, thus having a rather spherical shape, whereas an increase in the reaction temperature results in the cubic shape of the particles.
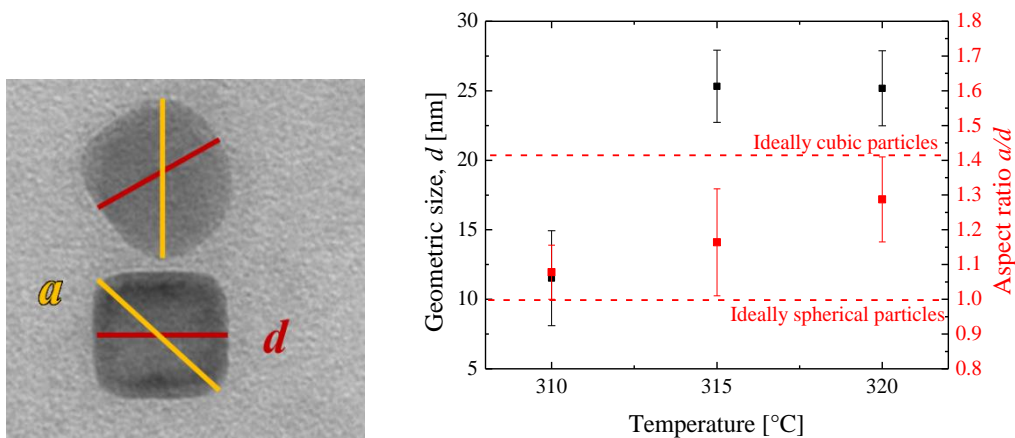
Figure 4-3. Correlation of the morphology of the particles (geometric size *d*, black, aspect ratio $\frac{a}{d}$ in red) with the reaction temperature.

This comes in agreement with the observations made by Bao et al.[55] According to it, below 314°C the monomers attach and grow isotropically from the nucleation sites with no specific growth direction leading to spherical particles. At a temperature of 320 °C a transition to formation of cubic particles is observed, which is caused by the quick growth along the {111} faces due to higher surface energies of {111} faces, than of {100} faces for an inverse spinel structure.[132] The structure of the particles synthesized at 315 °C represents an intermediate state between a cubic and a spherical shape.

4.2. Synthesis of CoFe$_2$O$_4$ by acetylacetonate complex thermal decomposition

This synthetic approach is based on thermal decomposition of a mixture of iron acetylacetonate (Fe(acac)$_3$) and cobalt acetylacetonate (Co(acac)$_2$) complexes, performed repeatedly for obtaining larger cobalt ferrite particles.[66] The process is similar to the decomposition of oleate complexes, except that the commercially available acetylacetonate complexes are taken and oleyl amine and oleyl alcohol are used along with oleic acid as the surface agents. The distinctive feature of this synthetic approach is that it consists of the preliminary seed particles synthesis and repeated growth steps. Thus, the control over the particle morphology takes place not only by controlling the reaction temperature and the reaction time, but also by the variation of the number of the growth steps. Thermal decomposition of acetylacetonate complexes of various metals is investigated by Von Hoene et. al.[133] According to it, acetone, and carbon dioxide are the only gaseous products for thermal decomposition of iron and cobalt acetylacetonate complexes. However, presence in the solution of the reduction agents such as oleyl alcohol[134], oleylamine[135] and oleic acid[136,137] might lead to a broader range of byproducts. The sum reaction can then be written the following way:

$$\text{I. 2h, 200°C}$$
$$\text{II. 1h, 300°C}$$
$$2Fe(acac)_3 + Co(acac)_2 \xrightarrow{\hspace{1.5cm}} CoFe_2O_4 + xC_3H_6O + yCO_2$$
$$\text{Oleyl alcohol}$$
$$\text{Oleylamine}$$
$$\text{Oleic acid}$$
$$\text{Dibenzyl ether}$$
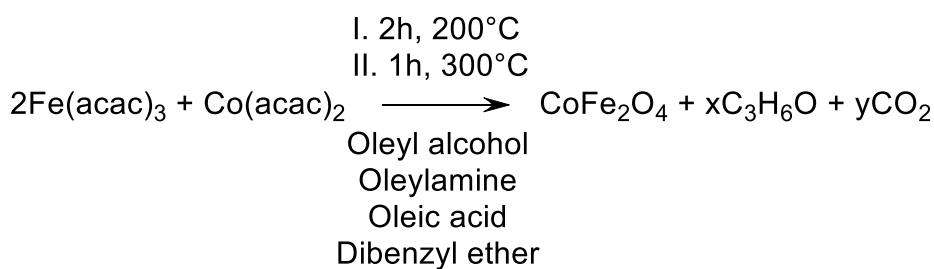
To investigate the influence of the temperature and reaction time on the size and shape of the resulting particles the sample synthesized at a temperature of 300 °C (samples **CFA-300/1h×n**) is compared with the samples synthesized at 280 °C (**CFA-280/1h×n** and **CFA-280/2h×n**).

Table 4-2. Overview on the CoFe$_2$O$_4$ particles synthesized by acetylacetonate complex decomposition

Sample name	Synthesis temperature [°C]	Growth step time [h]	Growth iterations
CFA-300/1h×2	300	1	2
CFA-280/1h×8	280	1	8
CFA-280/2h×5	280	2	5
CFA-280/2h×2	280	2	2

TEM images of the samples CFA-300/1h×1 and CFA-280/2h×1 are shown on **Figure 4-4**. Seed particles synthesized at both temperatures have spherical shape. The CoFe$_2$O$_4$ seeds, synthesized at 280°C/1h have more narrow geometric size distribution, than the seeds synthesized at 280°C/2h (see **Figure 4-5 a**). However, further growth steps lead to narrowing of the geometric size distribution for sample **CFA-280/2h×5** ($d = 11.3$nm $\sigma = 0.10$) compared to sample **CFA-280/1h×8** ($d = 14.7$nm $\sigma = 0.23$) and sample **CFA-300/1h×2** ($d = 11.5$nm $\sigma = 0.17$) (**Figure 4-5 b**). The particles synthesized at 280°C have a smaller geometric size and require more growth steps to achieve the same geometric size as the particles synthesized at 300°C. Prolonging the reaction time leads to a narrowing of the size distribution. This can be explained by the Ostwald ripening process taking place after the monomer concentration exhausts for LaMer growth. The smaller particles are consumed by the bigger ones, resulting in a narrower size distribution. Another important observation refers to the washing procedure and redispersion: the particles synthesized at 280 °C require only 1:4 excess of EtOH instead of 1:20 required to wash the particles synthesized at 300 °C.

a)   b)
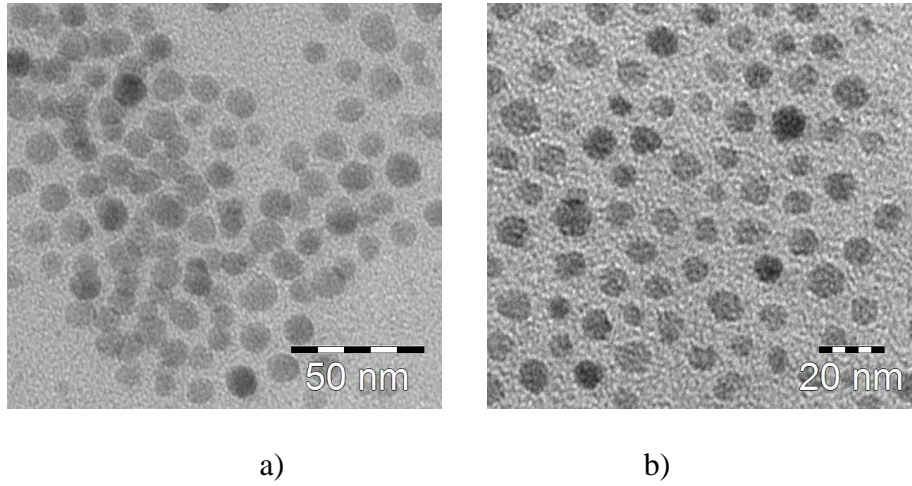
**Figure 4-4. TEM images of the seed CoFe$_2$O$_4$ particles for samples CFA-280/1h×8 (a) and CFA-280/2h×5 (b)**
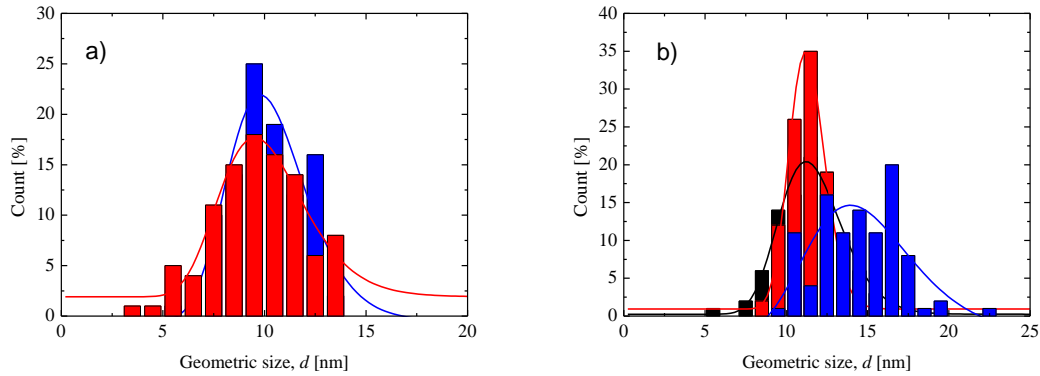
Figure 4-5. Geometric size histograms for samples synthesized at different temperature and reaction time a) after the seed formation (CFA-280/1h×8, blue; CFA-280/2h×5, red) b) after growth iterations (CFA-300/1h×2, black; CFA-280/1h×8, blue; CFA-280/2h×5, red)

Another parameter suitable for characterization of the particles growth is the size of the magnetic core (d_{mag}). First, the initial susceptibility (χ_{ini}) is read from the slope of the magnetization virgin curve of a particles dispersion Vibrating sample magnetometry measurement at room temperature and the magnetic moment (m) is calculated using equation (**1-18**). Using equation (**4-1**) the size of the magnetic core for an equivalent spherical particle can be calculated.

$$d_{mag} = \left(\frac{6 \cdot m}{\pi \cdot M_S} \right)^{\frac{1}{3}} \qquad \textbf{(4-1)}$$

27

Figure 4-6 shows the difference in the size of the magnetic core after each growth step for the described samples. For sample **CFA-300/1h**, d_{mag} of the seed particles shows the highest value (8.2 nm) and the single growth steps leads to an increase of d_{mag} by 0.8 nm. The seed particles of sample **CFA-280/2h** show the smallest value of d_{mag} (6.9 nm), however the average increase of d_{mag} per a growth step is 0.7 nm, comparable with the sample **CFA-300/1h**. The value of d_{mag} for the seed particles sample **CFA-280/1h** is 7.6 nm. The average increase of d_{mag} per a growth step is the smallest: only 0.3 nm.
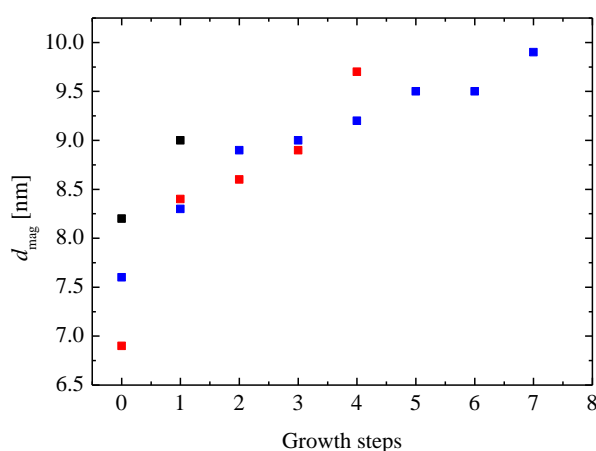
Figure 4-6. Dependence of the magnetic core size, depending on growth step time and temperature of samples CFA-300/1h×2, black; CFA-280/1h×8, blue; CFA-280/2h×5, red.

The data obtained from TEM and VSM on the growth character of the CoFe$_2$O$_4$ nanoparticles synthesized by decomposition of the mixture of Fe(acac)$_3$ and Co(acac)$_2$ allows to make following conclusions. The higher temperature (300 °C) leads to a formation of the larger seed particles and to the highest growth per a growth step. Lower temperature (280 °C) leads to the smaller seed particles and significant deceleration of the further growth. The geometric size distribution is also broadened. Increasing the reaction time at temperature of 280 °C from 1 h to 2 h leads to an even smaller seed particles, but the geometric size distribution is the narrowest after the growth iterations and the growth rate is comparable to the growth rate at 300 °C.

4.3. Physical properties comparison of CoFe$_2$O$_4$ nanoparticles synthesized by different methods

4.3.1. Investigation of the magnetic properties of CoFe$_2$O$_4$ nanoparticles

Since the further application of the CoFe$_2$O$_4$ nanoparticles involves their magnetic properties a closer study of their magnetic behavior is required. Among the important parameters, which must be defined are the magnetization behavior in dispersion and in solid state, saturation magnetization (M_S), coercivity (H_c), remanence (M_r) as well as magnetic relaxation in alternating magnetic fields. The magnetic properties of the particles were investigated using the Vibrating sample magnetometry (VSM) and AC-Susceptometry.

The magnetization curves measured at room temperature of samples **CFO-320** and **CFA-280/2h×5** both in form of a powder and as dispersion in toluene are shown on **Figure 4-7**. The concentration of the magnetic particles in the measured dispersions is equal. Both types of the particles show superparamagnetic behavior as a dispersion and hysteretic ferromagnetic behavior as powder. The magnetization curve of CFO-320 dispersion shows slight deviation between ascending and descending magnetization branches in range from 0 to 500 kA·m^{-1} and from -500 to 0 kA·m^{-1} (also known as "wasp-waist")[138–140], but no remanence magnetization and coercivity at zero magnetization. Normally, such type of magnetization behavior is observed, when species with different magnetic properties (for example, ferromagnetic and superparamagnetic) are found in the sample.[138] In the case of the measured nanoparticles this might indicate the reversible formation of superstructures, such as chains or particle clusters, induced by the magnetic field, which show high Brownian relaxation time (τ_B) and thus a hysteretic behavior as opposed to the single nanoparticles, which have τ_B small enough to show superparamagnetic behavior in the dispersion at room temperature. Magnetization curve of **CFA-280/2h×5** dispersion shows sharper superparamagnetic curve and no sign of hysteresis.
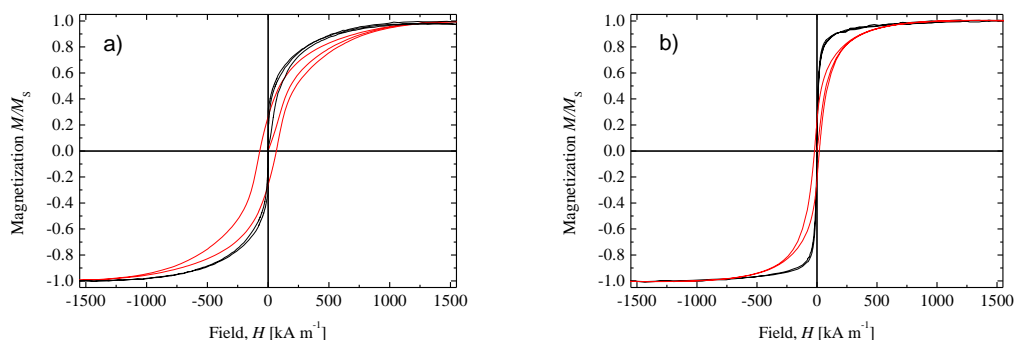
Figure 4-7. VSM magnetization curves measured at 298K for dispersions in toluene (black) and solid samples (red) of samples CFO-320 (a) and CFA-280/2h×5 (b).

For sample **CFA-280/2h×5** the distribution of d_{mag} was calculated using the Langevin fit (see equation (**1-19**). The d_{mag} distribution curve and histogram of the geometric size d are compared on **Figure 4-8**.
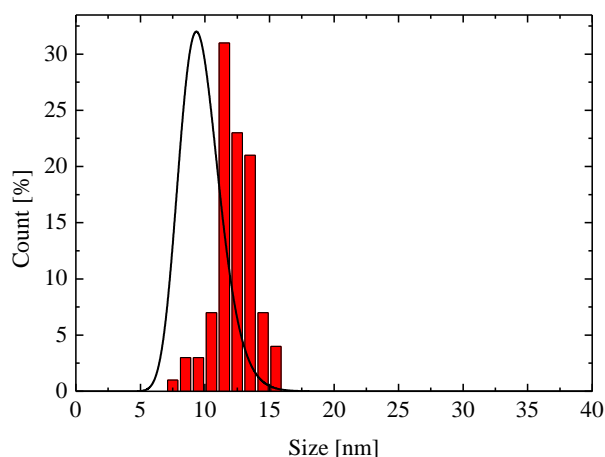
Figure 4-8. Distribution of the magnetic core size d_{mag} obtained from VSM (black) and geometric size d histogram obtained from TEM (red) for sample CFA-280/2h×5.

The value of d_{mag} is substantially lower, than the value of d. For sample **CFA-280/2h×5** d_{mag} is (9.6±1.2) nm (the value of d_{mag} calculated from χ_{ini} is 9.7), and the value of d is (12.2±1.5) nm. There possible explanation for such discrepancy might be the formation of amorphous non-magnetic phase or defects in the crystal structure, leading to lower magnetic moment of the particle and thus to smaller size of the magnetic core. The presence of a non-spinel iron

oxide structures in the core of the nanoparticles for magnetite was observed by Wetterskog et al.[137]
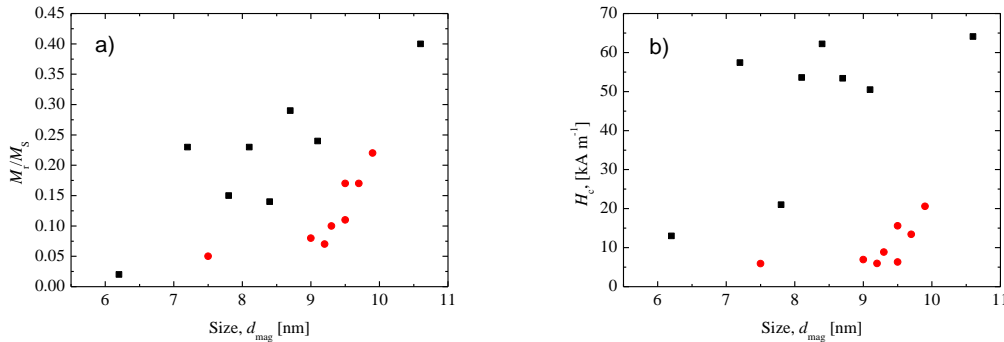
Figure 4-9. Correlation of remanence magnetization (a) and coercivity (b) with the size of the magnetic core as calculated from VSM measurements for samples synthesized using oleate complex decomposition (black) and acetylacetonate complex decomposition (red).

The magnetic properties of the solid samples are shown on figures on **Figure 4-7** and **Figure 4-9**. Both particles species show hysteretic behavior as a solid. The M_r and H_c values of the particles synthesized using decomposition of oleate complexes are higher, than of particles, synthesized over acetylacetonate complex decomposition, when the samples with equal d_{mag} value are compared. The values of M_r and H_c grow with increasing d_{mag}. This correlation is typical for single domain magnetic particles.[107] The results of the VSM measurements are gathered in **Table 4-3**. It can be seen that samples synthesized using the decomposition of oleate complexes show high remanence and coercivity, but small saturation magnetization. The magnetic content of cobalt ferrite ($\mu_{CoFe2O4}$) calculated basing on the saturation magnetization of bulk CoFe$_2$O$_4$ (75.5 A·m^2·kg^{-1})[128] is only 6.5 % for the spherical particles (**CFO-310**). The samples synthesized using the decomposition of oleate complexes show high saturation magnetization, but lower remanence and coercivity, when compared with samples synthesized using decomposition of oleate complexes.

Table 4-3. Overview on the results of the VSM measurements of CoFe$_2$O$_4$ nanoparticles synthesized using different synthetic approaches

Sample name	d_{mag} [nm]	Mr/M$_S$	Hc, [kA·m^{-1}]	M$_S$, [A·m^2·kg^{-1}]	$\mu_{CoFe2O4}$ [%]
CFO-310	7.2	0.23	54.7	4.9	6.5
CFO-315	9.1	0.24	50.5	9.4	12.5
CFO-320	8.1	0.23	53.6	30.6	40.5
CFA-300/1h×2	9.0	0.08	6.93	64.6	85.5
CFA-280/1h×8	9.9	0.21	20.6	54.3	72.0
CFA-280/2h×5	9.7	0.17	13.4	65.8	87.2
CFA-280/2h×2	9.5	0.11	6.3	72.3	95.7

The AC Susceptometry measurements of particles dispersions in toluene were performed to obtain information about the magnetization and relaxation processes in the particles and their hydrodynamic properties. To calculate the hydrodynamic size distribution from the AC Susceptometry measurements all data sets are quantitatively described as a single relaxation time Debye process extended for a lognormal distribution of the particle radius.[141,142]

$$\chi^* = \chi_{ini} \int_0^\infty \frac{1}{1 - i\omega\tau_B(r_h)} f(r_h) dr_h \qquad \textbf{(4-2)}^{[143]}$$

$$f(r_h) = \frac{1}{\sqrt{2\pi}\sigma r_h} \exp\left(-\frac{\ln^2(\frac{r_h}{r_{eff}})}{2\sigma^2}\right) \qquad \textbf{(4-3)}^{[143]}$$

Where χ^* is the complex magnetic susceptibility, χ_{ini} the initial susceptibility, ω the angular frequency, τ_B is the Brownian relaxation time, r_h the hydrodynamic particle radius, r_{eff} is the effective median radius, σ is the standard deviation. Then, $d_{AC} = 2r_h$.

The measurement curves for samples **CFO-320** and **CFA-280/2h×5** are shown on **Figure 4-10**. The samples synthesized using the oleate complexes decomposition show no susceptibility peak in the frequency range from 10 to 10^5 Hz, with the susceptibility decreasing starting from the frequency of 1 Hz. This might indicate that the susceptibility peak is located at lower frequencies, what is characteristic for large objects. According to this some superstructures, such as agglomerates or chains might be present in the solution, which

were not destroyed by preliminary sonication. The results from the VSM measurements hint at reversible formation of such structures already at low external fields. Fitting these curves with extended Debye model is not possible.
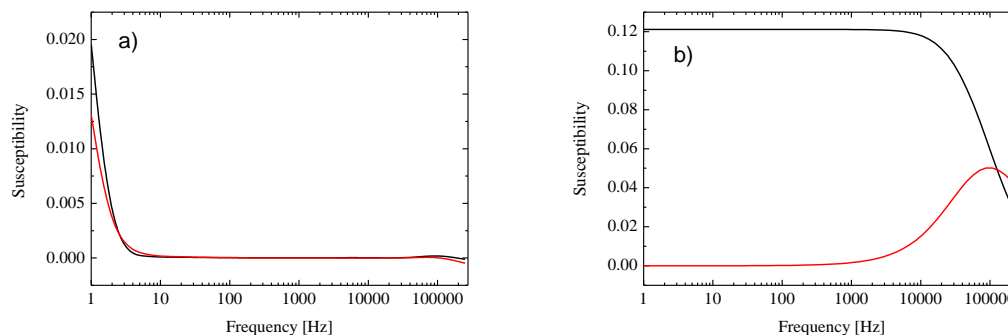

Figure 4-10. AC-Susceptometry curves of dispersions in toluene (real susceptibility in black, imaginary susceptibility in red) for samples CFO-320 (a) and CFA-280/2h×5 (b).

The measurement of sample **CFA-280/2h×5** corresponds to prevailing Brownian relaxation. The magnetic susceptibility of the sample measured by VSM and AC-Susceptometry differs by less than 10 %.

4.3.2.   Investigation of the crystal structure of CoFe$_2$O$_4$ nanoparticles

To obtain the information about the crystal structure of the synthesized particles, X-Ray powder diffractometry measurements were performed. To achieve higher resolution of the reflexes, a molybdenum cathode ($K\alpha = 0.71$ Å) instead of copper cathode ($K\alpha = 1.54$ Å) was used. The reflexes of the samples are shown on **Figure 4-11**. The position of the reflexes and their intensities were compared to the values found in literature for CoFe$_2$O$_4$ [144] and with the values for CoO and FeO (wüstite) calculated using Mercury 3.6 software (see **Table 4-4**).

Other cobalt oxides and iron oxides do not have reflexes, which would match with the measured ones. The reflex at 13.7-13.8 was taken as a reference for calculating the relative intensities, since both CoO and FeO do not have a reflex at this 2θ value.
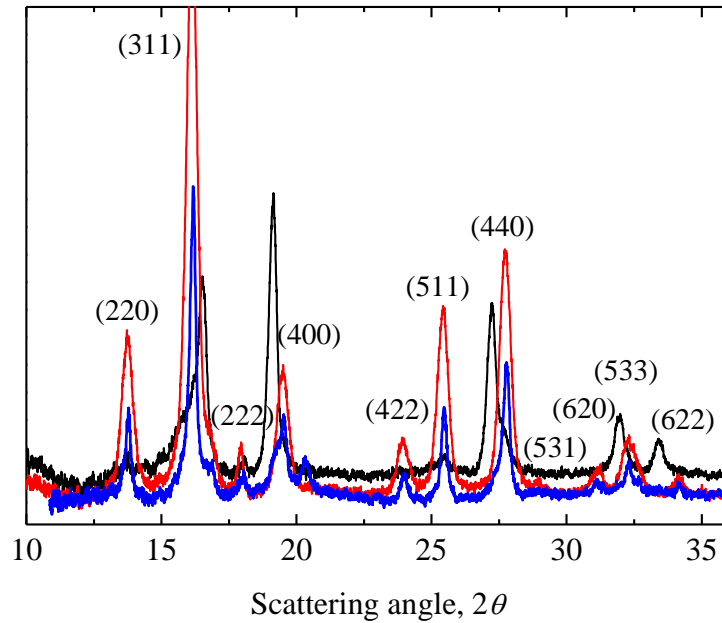
Figure 4-11. XRD measurement of samples CFO-310 (black) CFO-320 (blue) and CFA-280/2h×5 (red)

The comparison shows that the reflexes of sample **CFA-280/2h×5** come in good agreement with the literature values both in position and intensity. The deviation in reflex position does not exceed 5%, and deviations in relative intensities about 10 %. The comparison of reflexes for sample **CFO-310** with literature values shows, that reflexes for faces {422} and {620} expected at 2θ values of 24.54° and 32.57° respectively are not found at all, and that the intensities of the reflexes for the faces {311} and {400} differ strongly from what is expected for cobalt ferrite structure. Wetterskog et alt. have shown, that formation of FeO$_{1-x}$ is possible during the synthesis of Fe$_3$O$_4$ nanocubes as a result of crystal defects on the surface.[145] However, the content of this phase did not exceed 5 % of the mass weight.[146] The content of the possible FeO found in sample **CFO-310** is up to 40 % as calculated from the peak intensities. This would explain the low saturation magnetization of the sample, since saturation magnetization of bulk spinel-structured wüstite is reported to be in range from 36 to 50 A·m^2·kg^{-1},[147] (compared to saturation magnetization of a bulk CoFeO$_4$ of 75.5 A·m^2·kg^{-1})[128]. The reflexes at 2θ values of 32.1° and 33.5° indicate that presence CoO is also possible.

Table 4-4. Comparison of XRD reflex positions and intensities of samples CFO-310, CFO-320 and CFA-280/2h×5 with literature values for CoFe$_2$O$_4$, FeO and CoO.
* – calculated using Mercury 3.6 software for data obtained from respective sources

CFA-280/2h×5		CFO-310		CFO-320		CoFe$_2$O$_4$[144]		FeO *[148]		CoO *[149]	
2θ	I	2θ	I	2θ	I	2θ	I	2θ	I	2θ	I
13.7	30.0	9.8	30.0	13.8	30.0	13.81	30				
16.2	107.5	16.5	100	16.2	95.2	16.27	100	16.3	70	16.6	100
17.9	5.5	18.0	n/a	18.0	n/a	17.01	8				
19.6	25.4	19.2	77.7	19.5	24.9	19.77	20	18.8	100	19.3	50
				20.3	10.9						
23.9	10.3	25.4	18.8	24.0	11.5	24.54	10				
25.4	32.8			25.5	24.7	26.15	30	26.7	40		
27.7	43.3	27.3	61.5	27.9	49.4	28.73	40			27.3	60
31.2	3.8			31.2	n/a	32.57	4	31.4			
32.4	10.6	32.1	22.0	32.3	n/a	33.98	9	32.9	9	32.0	30
34.2	1.8	33.5	13.3	34.2	n/a	34.44	4			33.5	26

The XRD measurements were supported by Mössbauer spectroscopy. The spectra of the cobalt ferrite samples are shown on **Figure 4-12**. All measurements were performed at room temperature.

The spectrum of sample **CFO-310** shows a broad distribution of hyperfine fields (proportional to a sextet splitting) and a relaxated state. This indicates that the sample has significantly lower anisotropy energy. The sextet structure of the spectrum corresponds to magnetically blocked material. A doublet is observed in the middle with a shift to the right. Such doublet corresponds to a paramagnetic or a superparamagnetic material. Also a shift in the isomerism of the doublet can indicate a different valence for iron atom, for example, Fe^{2+}. This confirms the assumption, that in this sample a wüstite phase is present.

The spectrum of sample **CFO-320** shows a strong noise, caused presumably by a small amount of measured material. A small sextet splitting is observed, compared to a dominant sextet. This can be a sequence of an exchange interaction, though the strong noise hinders the exact interpretation. The inner side of line 1 shows an additional spectral contribution. This might indicate the beginning of the relaxation. This comes in agreement with the fact that the basis line between lines 3 and 4 does not return to 100 % transmission.

The spectrum of sample **CFA-280/2h×5** shows a clear magnetically blocked sextet. The lines are not Lorentz-shaped, but slightly asymmetric with a small contraction, which corresponds to the Néelian relaxation, being the cause of nuclear levels degeneracy, characterized by the signal lines shrinkage.
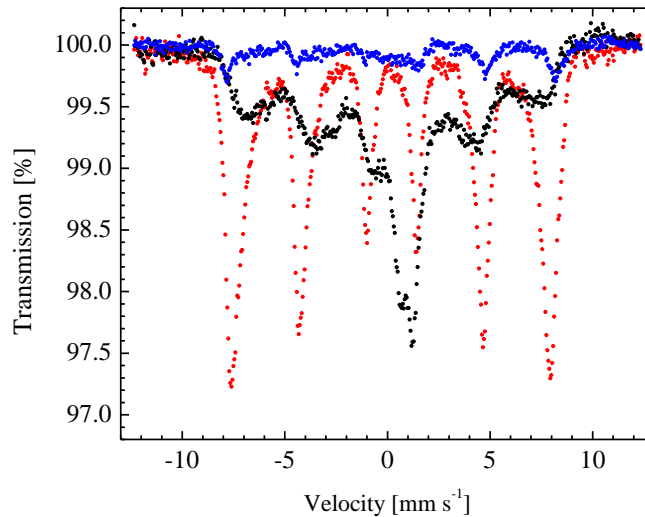

Figure 4-12. Mössbauer spectra of samples CFO-310 (black) CFO-320 (blue) and CFA-280/2h×5 (red), measured at 295K.

4.3.3. Investigation of the hydrodynamic properties of CoFe$_2$O$_4$ nanoparticles

To determine the hydrodynamic properties of the particles and to compare it with the data, obtained by other methods, the Dynamic light scattering experiments are performed. The toluene dispersions of the nanoparticles were measured at room temperature. In these measurements, hydrodynamic diameter d_h and its distribution are determined. The geometric size d histograms shown previously in are compared with the hydrodynamic size distributions on **Figure 4-13**.
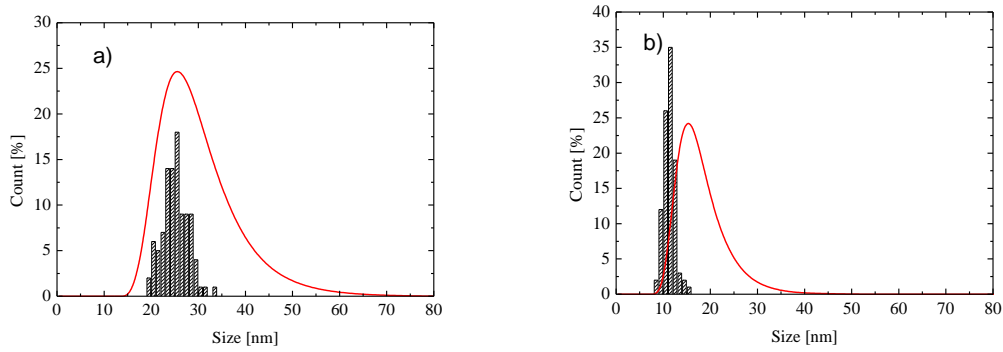
Figure 4-13. Comparison of the geometric size histogram (black) with DLS size distribution (red) for samples CFO-320 (a) and CFA-280/2h×5 (b).

The DLS measurement of sample **CFO-320** shows that mean number $d_h = 27.5$ nm, $\sigma = 0.22$) (compared to $d = 25.1$ nm $\sigma = 0.10$) and d_h distribution is slightly broader than the geometric size distribution (see **Figure 4-13 a**). In contrast to what have been seen in AC Susceptometry measurements (**Chapter 4.3.1**), no large objects are observed is observed, leading to a conclusion that the assumed aggregates form only in magnetic fields. The sample **CFA-280/2h×5** shows larger hydrodynamic diameter ($d_h = 16.5$ nm, $\sigma = 0.22$) than the geometric size ($d = 11.3$ nm, $\sigma = 0.10$).

The **Figure 4-14** shows the size distributions, obtained from DLS and AC Susceptometry measurements. The hydrodynamic diameter d_h deviates from d_{AC} by approximately 15% and the distribution curves correlate well with each other.
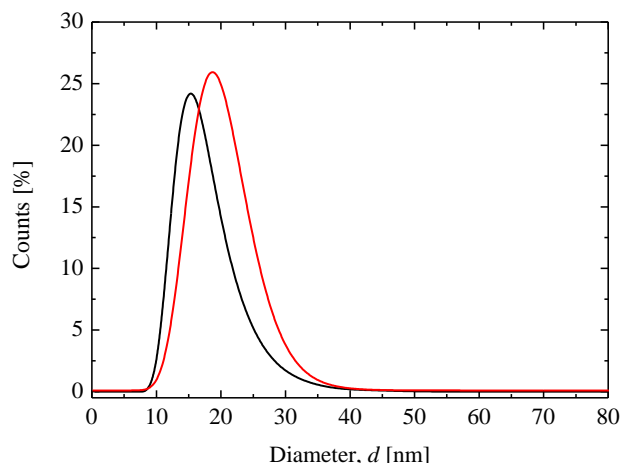
Figure 4-14. Distribution curve for DLS (black) and AC Susceptometry (red) experiments for sample CFA-280/2h×5.

The measurements results, obtained by using different measurement techniques are gathered in **Table 4-5**. All the size distributions except for the size of the magnetic core (d_{mag}) are fitted with the log-normal distribution fit. The hydrodynamic diameter obtained from both AC Susceptometry and DLS is slightly larger, than the geometric size d obtained from TEM.

Table 4-5. Overview on the size measurement results, obtained by different measurement techniques.

Sample name	Geometric size, d [nm]		Magnetic core size, d_{mag} [nm]	Hydrodynamic diameter, d_{AC} [nm]		Hydrodynamic diameter, d_{hyd} [nm]	
	d	σ	d_{mag}	d_{AC}	σ	d_{hyd}	σ
CFO-310	15.5	0.07	8.2	-	-	18.5	0.24
CFO-315	25.3	0.08	9.2	-	-	29.3	0.31
CFO-320	25.1	0.10	8.1	-	-	27.5	0.22
CFA-300/1h×2	11.5	0.17	9.0	19.9	0.46	12.7	0.22
CFA-280/1h×8	14.7	0.23	9.9	14.1	0.46	-	-
CFA-280/2h×5	11.3	0.10	9.7	19.8	0.24	16.5	0.22

4.4. Summary on the synthesis of CoFe$_2$O$_4$ nanoparticles

Two approaches for synthesis of CoFe$_2$O$_4$ nanoparticles were investigated. Both synthetic approaches using the mixture of oleate complexes and mixture of acetylacetonate complexes result in well-dispersed ferromagnetic particle batches with acceptable yields.

The particles synthesized using oleate complexes decomposition have larger size and more uniform shape and size distributions. The possibility to control the shape of the resulting

particles is an important tool for further functionalization with noble metal counterpart. Considering the magnetic properties of these samples it is important to mention that the saturation magnetization is much lower than of bulk cobalt ferrite. Deviation from the cobalt ferrite crystal structure is assumed to be the cause. Remanent magnetization and coercivity are nevertheless large. Though hydrodynamics properties investigated by DLS are suitable for further application of these particles in the synthesis of hybrid systems, possible formation of the superstructures in external magnetic fields is not to be neglected, since it limits the investigation using AC Susceptometry. The further development of this synthetic approach would be to clarify the prerequisites leading to formation of wüstite. Formation of superstructures in the external magnetic field may also be a promising research topic. Though these particles have certain drawbacks in their properties, their fine morphology and size range are important for synthesis of the dumbbell-like structures in the next chapter.

The particles synthesized over acetylacetonate complexes decomposition require more time for synthesis. The size control is more accurate; however, the particles produced this way have smaller size, than the particles synthesized by oleate complexes decomposition. Both magnetic and hydrodynamic properties are well enough to meet the requirements for further noble metal attachment and characterization.

In general, the goal to synthesize monodisperse ferromagnetic nanoparticles with defined hydrodynamic and magnetic properties is considered fulfilled.

5. Synthesis and characterization of the Ag@CoFe₂O₄ dumbbell-like particles

In this chapter, different synthetic approaches towards synthesis of dimeric particles with asymmetric architecture, the so-called dumbbell-like particles (DLP), consisting of a magnetic particle ($CoFe_2O_4$) and a noble metal counterpart (Ag), are investigated and optimized. The goal is to synthesize the particles, which will show asymmetry in both geometry and reactivity for further functionalization with soft matter. The particles should be stable against degradation, be uniform in their size and architecture. The new properties, such as surface plasmon resonance, coming from the noble metal counterpart should be investigated. Lack of information on the formation mechanism and properties of these particles make a series of detailed experiments, such as kinetic experiments, necessary for a better understanding of the synthetic process.

5.1. Optimization of the Ag@CoFe₂O₄ dumbbell-like particle synthesis

A broad range of dumbbell-like particles synthetic approaches[83–87,91–93,126,127,150–152] include the reduction of noble metal precursor on the surface of a magnetic particle. Two synthetic procedures are optimized by adjusting the reaction parameters, such as reaction temperature, reaction time, solvent, magnetic particles and noble metal precursor concentrations and their ratios. The functionalization degree (defined as the percentage of $CoFe_2O_4$ particles functionalized with at least one Ag counterpart), presence of free Ag particles in the solution, the size of the attached Ag particles and morphology of the resulting particles are investigated.

5.1.1. Synthesis of Ag@CoFe$_2$O$_4$ by reduction of silver salt in 1,2,3,4-tetrahydronaphthalene

The experiments towards synthesizing the dumbbell-like nanoparticles involve the cobalt ferrite nanoparticles obtained by the oleate complexes decomposition synthesis from **Chapter 4.1** as primary particles. The synthetic procedure bases on the slow reduction of silver salt in 1,2,3,4-tetrahydronaphthalene (tetralin) on the surface of magnetic nanoparticles.[92] In this synthetic procedure the influence of the precursor injection way and the influence of the precursor concentrations, ratios and temperature is investigated and optimized.

5.1.1.1. Influence of the silver salt addition way on the size of the Ag particles

The first investigated reaction parameter is the addition way of the silver salt (AgNO$_3$) into the reaction medium. To a dispersion of CoFe$_2$O$_4$ nanoparticles in tetralin (sample CFO-320) are added and heated to 100 °C for 1h under N$_2$. Three approaches of silver salt addition are considered: 1) the silver salt is mixed with the dispersion of the cobalt ferrite nanoparticles and heated up; 2) the silver salt solution in tetralin (0.2 mg·ml^{-1}) is injected into the hot cobalt ferrite dispersion; 3) the silver salt solution in tetralin (0.2 mg·ml^{-1}) is added dropwise into the hot cobalt ferrite dispersion. The end concentration of the CoFe$_2$O$_4$ and of Ag is 0.1 mg·ml^{-1}. For convenience the concentration of Ag atoms in the solution and not of the silver salt is considered for further calculations.

Figure 5-1 shows the geometric size distribution of the attached Ag particles for different precursor injection ways. It can be observed that the geometric size of the silver particles does not differ much for the two approaches (2 and 3), when the silver salt is added into a hot dispersion, independently if it is injected at once or dropwise. The geometric size $d = 2.5$ nm, $\sigma = 0.21$ in case of the immediate injection and $d = 2.4$ nm, $\sigma = 0.23$ in case of the dropwise

addition. However the diameter of the silver particles obtained in the reaction approach, when the silver salt is heated together with the cobalt ferrite dispersion (approach 1), are bigger (d = 3.4 nm, σ = 0.15) and its distribution is more narrow. For the further syntheses the hot injection approach is chosen.
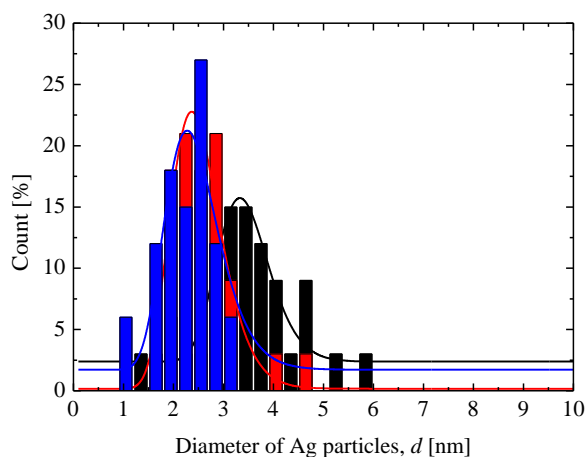
Figure 5-1. Dependence of the geometric size of the attached Ag particles from the precursor addition approach: before heating (black; d = 3.4 nm, σ = 0.15), hot injection (red; d = 2.5 nm, σ = 0.21) and slow addition (blue; d = 2.4 nm, σ = 0.23).

5.1.1.2. Influence of the CoFe$_2$O$_4$ and Ag concentrations and their ratio on the size and the morphology of the Ag particles

The influence of the magnetic particles and silver salt concentrations on the the size and architecture control of the resulting particles is investigated in this part. Since the formation mechanism of the noble metal particles is not clear, it is essential to understand the possibilities to control the size and architecture of the resulting particles. A series of syntheses with varying CoFe$_2$O$_4$ concentration and a series of syntheses with varying silver salt concentrations were done. In this part silver acetate (AgAc) is used instead of silver nitrate (AgNO$_3$) to due to its better solubility in organic solvents.

a)   b)   c)
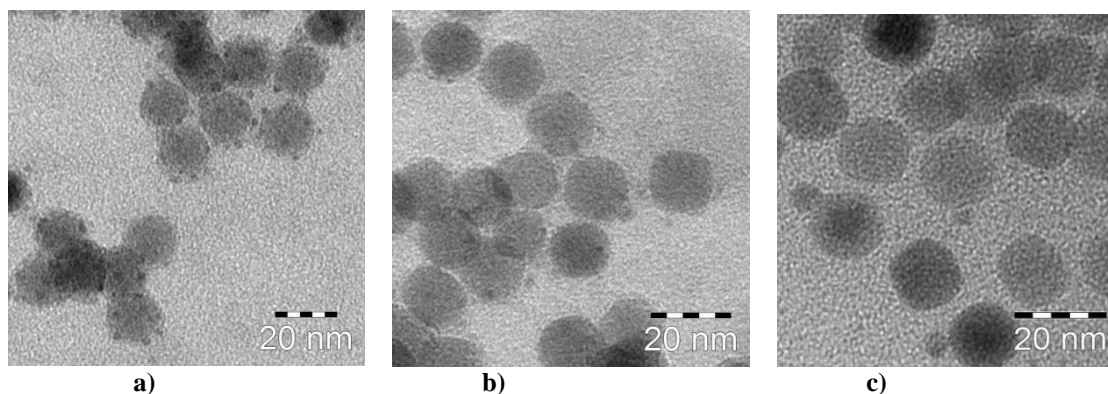
Figure 5-2. TEM images showing the architecture of the resulting particles at a constant Ag concentration of 0.1 mg·ml^{-1}, depending on CoFe$_2$O$_4$ concentration: a) 0.1mg·ml^{-1}, b) 0.4 mg·ml^{-1}, c) 0.8 mg·ml^{-1}.
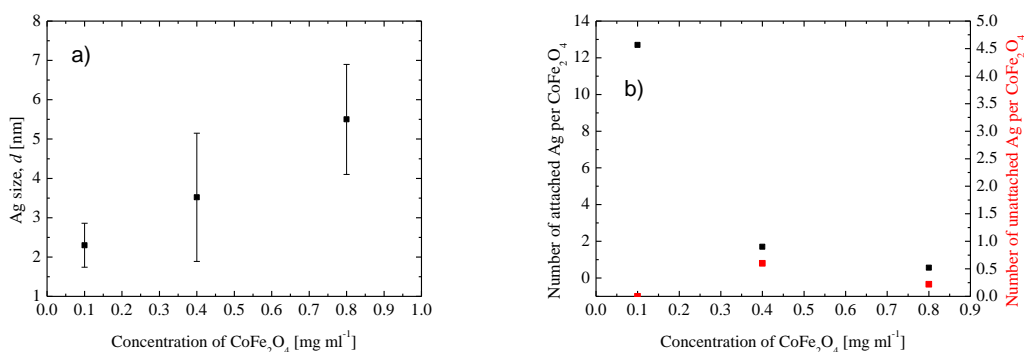
Figure 5-3. Influence of the cobalt ferrite concentration on the a) size and b) number of the resulting Ag particles at a constant Ag concentration of 0.1 mg·ml^{-1}.

In **Figure 5-2** TEM images of the resulting particles with increasing CoFe$_2$O$_4$ concentration are shown. It can be seen that low concentrations (0.1 mg·ml^{-1} and partially 0.4 mg·ml^{-1}) lead to a formation of particles with what can be called a raspberry-like architecture: multiple Ag particles are attached to each CoFe$_2$O$_4$ particle. With increasing concentration of CoFe$_2$O$_4$ particles the size of the resulting silver particles grows, while the number of the Ag particles per CoFe$_2$O$_4$ particle reduces. This can be better observed in **Figure 5-3** which quantifies the influence of the CoFe$_2$O$_4$ concentration on the size (**Figure 5-3 a**) and number of the resulting Ag particles (**Figure 5-3 b**) at a constant Ag concentration of 0.1 mg·ml^{-1} observed in the TEM images. At a CoFe$_2$O$_4$ concentration of 0.8 mg·ml^{-1} the diameter of the Ag particles reaches 5.5 nm ± 1.4 nm, but only 60% of the CoFe$_2$O$_4$ particles are functionalized. It can be seen that not only the size of the resulting Ag particles is dependent on the variation of the CoFe$_2$O$_4$ concentration with a constant Ag concentration of 0.1 mg·ml^{-1}, but also the

number of the CoFe$_2$O$_4$ particles with an attached Ag counterpart and the number of the free Ag particles.

a)   **b)**   **c)**
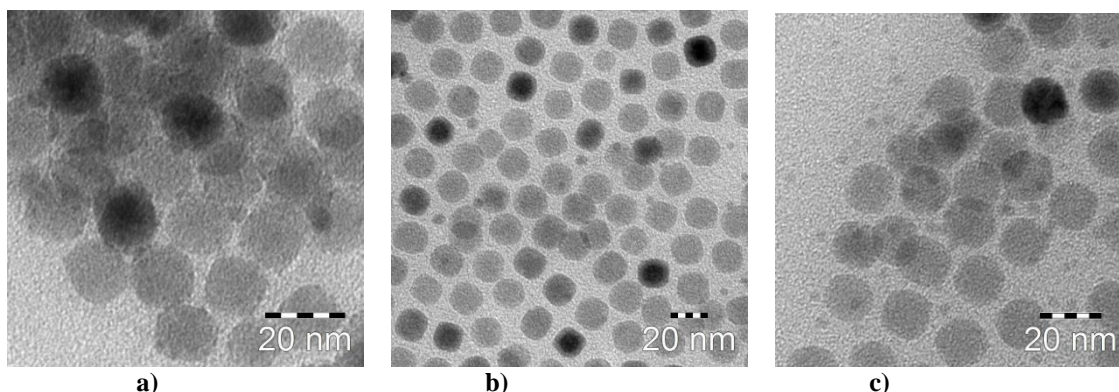
Figure 5-4. TEM images showing the architecture of the resulting particles at a constant CoFe$_2$O$_4$ concentration of 0.4 mg·ml^{-1}, depending on silver salt concentration concentration: a) 0.1mg·ml^{-1}, b) 0.2 mg·ml^{-1}, c) 0.4 mg·ml^{-1}.
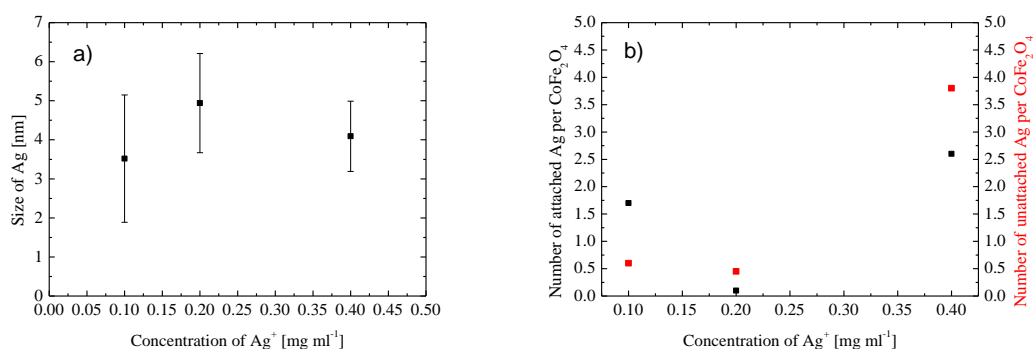
Figure 5-5. Influence of silver salt precursor concentration on the size and number of the resulting Ag particles at a CoFe$_2$O$_4$ concentration of 0.4 mg·ml^{-1}.

a)   b)   c)

Figure 5-4 shows again TEM images of the resulting particles but this time with increasing Ag concentration at constant CoFe$_2$O$_4$ concentration. The variation of Ag concentration was performed with concentrations of CoFe$_2$O$_4$ of 0.4 mg·ml^{-1} and 0.8 mg·ml^{-1}. The Ag concentration of 0.1 mg·ml^{-1} results in smaller Ag particles with the architecture strongly dependent from the CoFe$_2$O$_4$ concentration. Further increase of the Ag concentration to 0.4 mg·ml^{-1} leads to an increase of the size of the resulting particles, as well as of a number of the functionalized CoFe$_2$O$_4$ particles. Formation of unattached Ag particles in growing numbers is also observed at high Ag concentration. The quantification of the number of attached Ag particles per a CoFe$_2$O$_4$ particle is more difficult at high Ag concentration, since it is hard to distinguish an attached Ag particle from a random unattached one placed near a

CoFe$_2$O$_4$ particle. The quantification of what is measured in the TEM images is presented in **Figure 5-1 a) and b)** that computes the influence of the Ag$^+$ concentration on the size (**Figure 5-1 a**) and number of the resulting Ag particles (**Figure 5-1 b**) at a constant CoFe$_2$O$_4$ concentration of 0.4 mg·ml^{-1}.
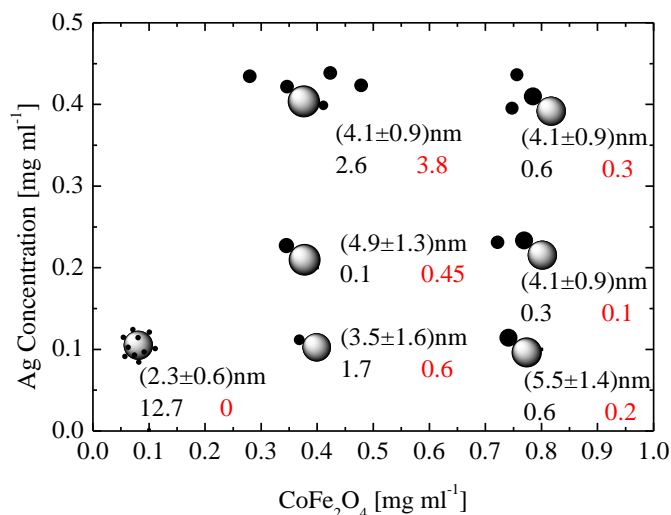
Figure 5-6. Overview of the architecture of the particles, depending on the precursor concentrations. In brackets the average geometric size is given, black number on the left is the average number of attached Ag particles per CoFe$_2$O$_4$ particle, red number is the average of unattached Ag particles per CoFe$_2$O$_4$ particle.

The summary of the observations made during the optimization of the synthesis of the dumbbell-like particles in tetralin are schematically shown in **Figure 5-6**. The synthetic approach leads to formation of the dumbbell-like particles under certain parameters. These are optimized towards the required architecture of the particles. It can be seen that not only the concentration of the single precursors is important, but also its ratio. As can be concluded the best samples are produced when the ratio between CoFe$_2$O$_4$ and Ag is in range from 1:1 to 1:2. High concentrations of both precursors are required to avoid raspberry-like structures and for the formation of larger Ag particles at equal precursors ratio. However, further increasing of the Ag salt concentration fails due to its poor solubility in tetralin. The content of dumbbells does not exceed 60%, what can't be considered as a uniform architecture of the particles.

5.1.2. Synthesis of Ag@CoFe$_2$O$_4$ by reduction of silver salt in toluene with oleylamine

The alternative synthetic approach was found in the literature[93] and is proposed for the synthesis of Ag@Fe$_3$O$_4$. The main difference to the synthetic approach in tetralin is the large amount of oleylamine in the reaction medium, which enhances the solubility of the silver acetate and increases the stability of the particles acting both as a surface agent and as a reduction agent. A typical reaction consists in mixing of a dispersion of magnetic nanoparticles in toluene with silver salt and heating it up to 70°C for 12 h under N$_2$. The concentration of cobalt ferrite and Ag was set to 0.85 mg·ml^{-1} with the ratio of the precursors 1:1. A series of experiments were done to estimate the impact of the temperature, reaction time and precursor ratio on the architecture and size of the resulting particles. For these syntheses particles synthesized in **Chapter 4.2** was used as the primary magnetic nanoparticles. The overview of the samples synthesized in this part is given in **Table 5-1**.

Table 5-1. Overview on the Ag@CoFe$_2$O$_4$ particle samples synthesized in toluene with oleylamine

Sample name	Primary particles	Synthesis temperature [°C]	CoFe$_2$O$_4$ conc. [mg·ml^{-1}]	Ag conc. [mg·ml^{-1}]	CoFe/Ag ratio
DLP-70/12h 1:1	CFA-300/1h×2	70	0.85	0.85	1:1
DLP-70/24h 1:1	CFA-300/1h×2	70	0.85	0.85	1:1
DLP-70/12h 1:1.8	CFA-300/1h×2	70	0.85	1.55	1:1.8
DLP-70/24h 1:1.8	CFA-300/1h×2	70	0.85	1.55	1:1.8
DLP-70/24h 1:1.8 II	CFA-280/2h×5	70	1.2	2.2	1:1.8
DLP-70/24h 1:1.8 III	CFA-280/2h×2	70	1.2	2.2	1:1.8

The reaction mechanism of Ag$^+$ reduction in absence of water and oxygen with oleylamine as a reduction agent on presented **Figure 5-7** was proposed by Chen et al.[153]. The mechanism involves the formation of stable complexes of Ag(I) salts with amines and then a one-electron transfer of the amines to the Ag(I) species and formation of amino radicals. The latter is the deprotonation from the amino radicals to imines or from imine to nitriles, which is followed by passivating and stabilizing silver nanoparticles.
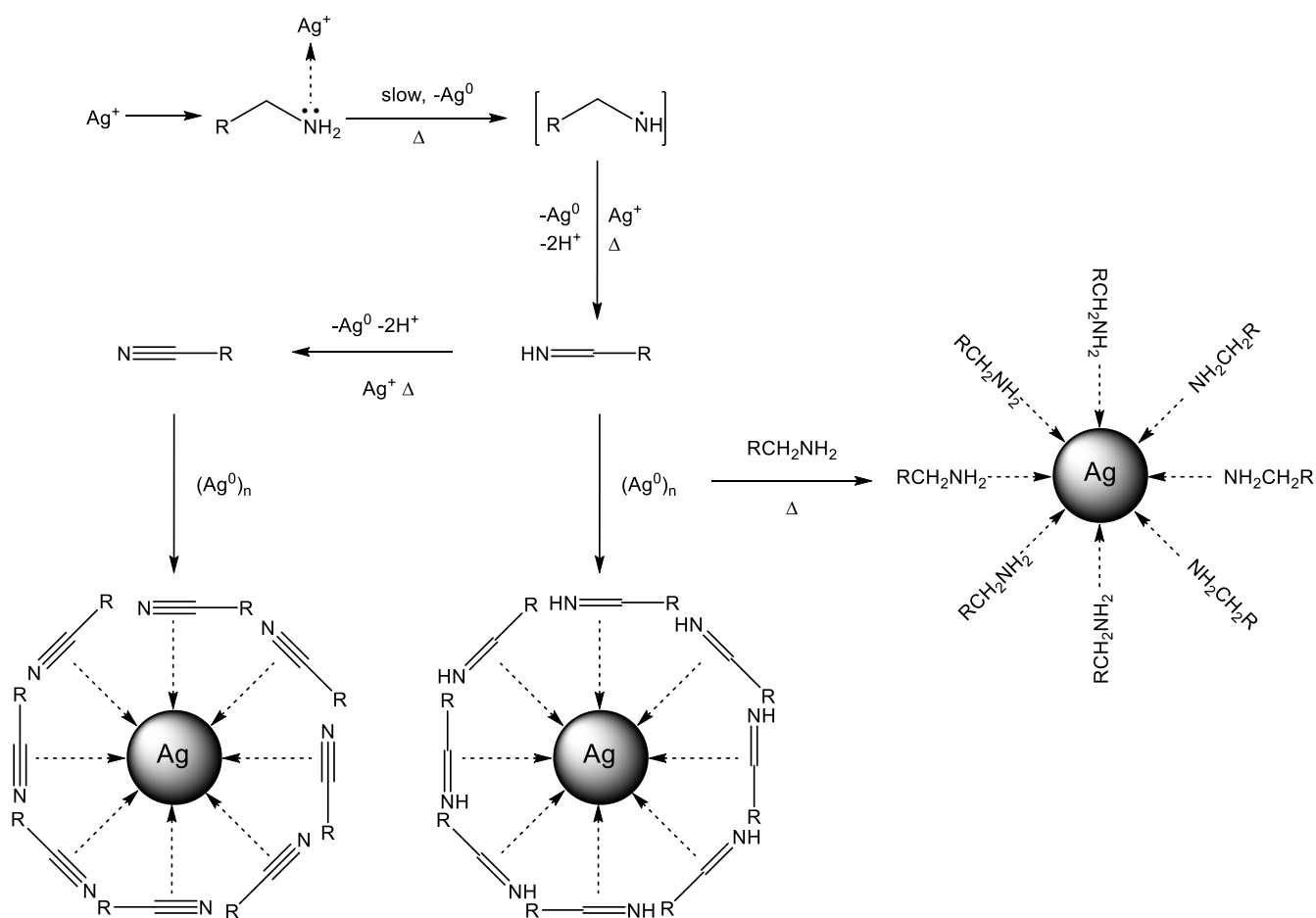
Figure 5-7. Proposed mechanism of silver reduction with oleylamine (reproduced from[153]).

5.1.2.1. Influence of the reaction time

The first parameter to be investigated is the influence of the reaction time. To investigate, if the conversion of Ag salt was complete, the reaction time was extended from 12 hours to 24 hours. This resulted in the increase of the size of $CoFe_2O_4$ from 3.7 nm, $\sigma = 0.19$; to 5.5 nm, $\sigma = 0.12$, but the functionalization degree of $CoFe_2O_4$ particles dropped from 83 % to 30 % as observed in **Figure 5-8** that shows the TEM images of both samples after 12h and 24h reaction time and the respective geometric size distributions of the attached Ag particles obtained from the TEM images. Since almost no free particles were found, this behavior can be attributed to Ostwald ripening process, when the number of the particles is reduced and their size increases. More discussion on the growth mechanism is found in **Chapter 5.2**.
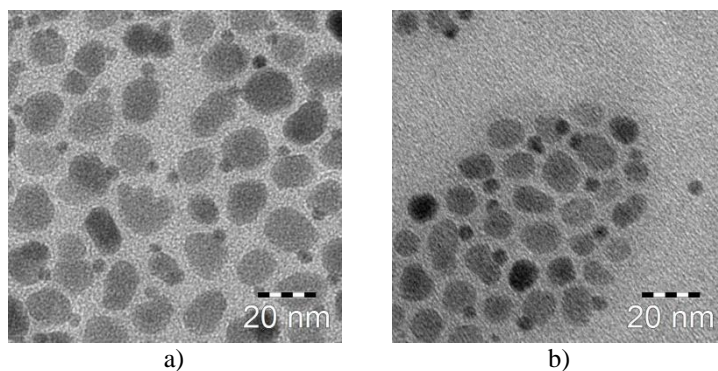
Figure 5-8. TEM images of samples DLP-70/12 (a, black) and DLP-70/24 (b, red) and respective geometric size distributions of attached Ag particles.

5.1.2.2. Influence of the precursor ratio

The next parameter of investigation is the precursor ratio. To compensate that, the samples with $CoFe_2O_4$/Ag ratio of 1:1 and 1:1.8 are compared. **Figure 5-9** shows the TEM images of the samples **DLP-70/24h 1:1** and **DLP-70/24h 1:1.8** and the geometric size distributions of the attached Ag particles. The mean diameter as well as the distribution remain unchanged (d = 5.5 nm, σ = 0.12 for sample **DLP-70/24h 1:1** and d = 5.4 nm, σ = 0.13, respectively), but the functionalization degree of $CoFe_2O_4$ particles has increased from 30 % to 85 %. Thus, extending the reaction time along with increasing the $CoFe_2O_4$/Ag ratio leads to an increase of the Ag particles diameter and precursor ratio concentration to increase of functionalization degree. Presumably, the high concentration of Ag suppresses the Ostwald ripening process, putting the system in "kinetic overdrive"[154] mode, when the Ag monomer concentration is

maintained at levels higher than the solubility of the Ag particles, leaving all the CoFe$_2$O$_4$ functionalized. Since a large number of free Ag particles is observed on the TEM images, it is possible to assume that the excess of Ag leads also to the formation of the free Ag particles.
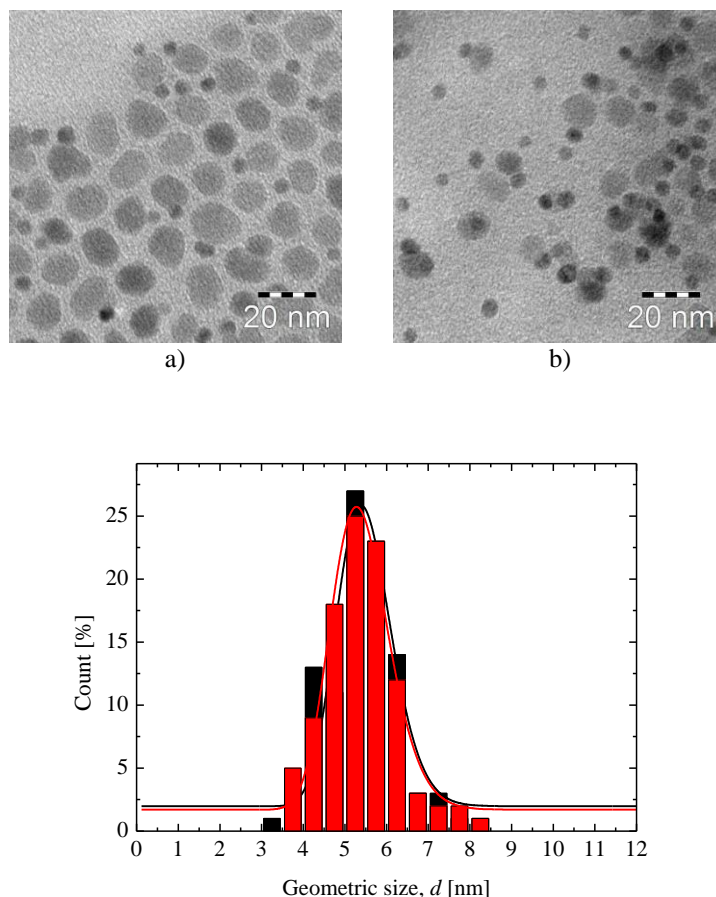
Figure 5-9 TEM images of samples DLP-70/24h 1:1 (a, black) and DLP-70/24h 1:1.8 (b, red) and respective geometric size distributions of attached Ag particles.

5.1.2.3. Influence of the temperature

In this part the influence of reaction temperature on the resulting particles is discussed. According to Zhang[85], that higher temperature can inhibit the formation of dumbbell-like particles was investigated in this subchapter. The synthesis was performed at 200 °C for 12 hours with precursor ratio 1:1.8. The resulting particles observed on TEM-images were compared to the sample **DLP-70/12h II**. **Figure 5-10** shows the geometric size distributions

of attached Ag particles for both samples. It was observed that not only the formation of dumbbell-like structures has occurred, but also the size distributions are nearly equal ($d = 4.0$ nm, $\sigma = 0.18$ for sample **DLP-70/12h II** and $d = 4.0$ nm, $\sigma = 0.20$, for sample **DLP-200/12h**). The functionalization degree has dropped however from 98 % to 73 %. The number of free Ag particles has visibly dropped.
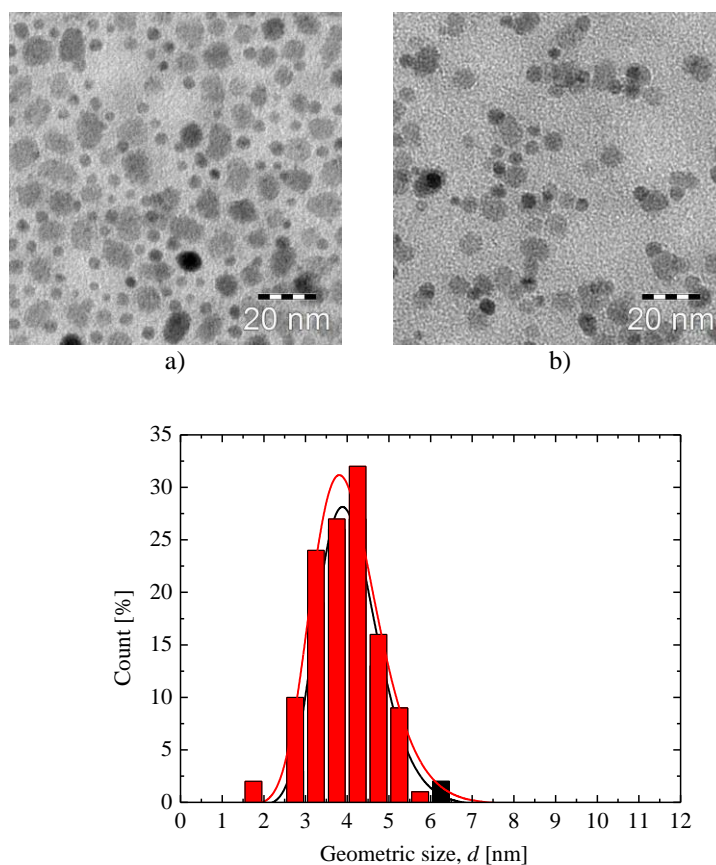
Figure 5-10. TEM images of samples DLP-70/12h II (a, black) and DLP-200/12h (b, red) and respective geometric size distributions of attached Ag particles.

5.1.2.4. Influence of the size of CoFe$_2$O$_4$ particles on the size of Ag part

The correlation between the size of the primary CoFe$_2$O$_4$ particle and the size of the Ag particle is investigated in this part. For this purpose the dumbbell-like particles synthesized under the same reaction conditions, but using different CoFe$_2$O$_4$ particle are compared. **Figure 5-11** plots the size of the Ag particle against the size of the CoFe$_2$O$_4$ particle it is attached to. On **Figure 5-11 a)** two samples synthesized at 70 °C, 12 h, precursor ratio 1:1

are compared and on **Figure 5-11 b)** two samples synthesized at 70 °C, 24 h, precursor ratio 1:1.8 are compared. A certain tendency of the Ag particles to reach larger diameter when growing on the bigger $CoFe_2O_4$ particle can be seen.
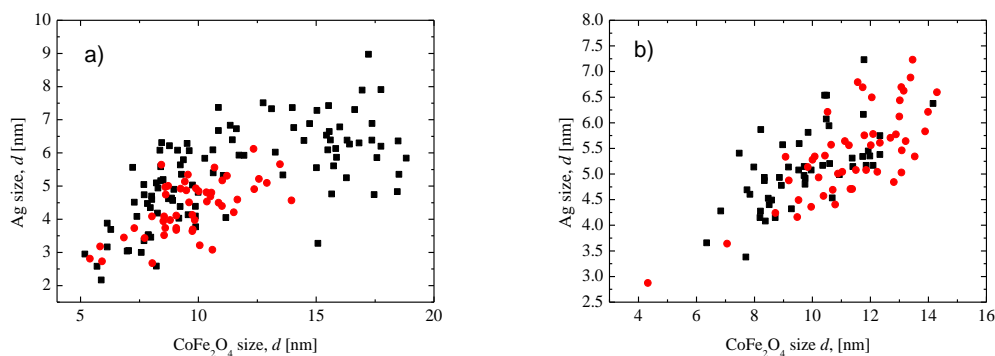
Figure 5-11. Correlation between the size of the Ag counterpart and the size of the CoFe₂O₄ particle it is attached to for samples made from different CoFe₂O₄ particles under the same reaction conditions: a) 70°C, 12h, precursor ratio 1:1, b) 70°C, 24h, precursor ratio 1:1.8

5.1.2.5. Influence of the size of the primary $CoFe_2O_4$ particles on the functionalization degree of the resulting dumbbell-like particles

Here the influence of the geometric size of the primary $CoFe_2O_4$ particles on the functionalization degree for samples synthesized under the same reaction conditions is discussed. **Figure 5-12** presents the correlation between the functionalization degree of $CoFe_2O_4$ with Ag and its geometric size for samples synthesized at 70 °C, 24 h, precursors ratio 1:1.8. For each Ag@$CoFe_2O_4$ particle batch the functionalization degree of the $CoFe_2O_4$ particles is plotted against the size distribution of the primary $CoFe_2O_4$ particles. It can be seen that $CoFe_2O_4$ particles with a smaller average diameter result in a higher functionalization degrees than in the case of the bigger $CoFe_2O_4$ particles. Using the $CoFe_2O_4$ particles with an average diameter above 18 nm results in almost no dumbbells. There is no clear evidence, if the growth on the surface of the $CoFe_2O_4$ particle does not occur at all or if the Ag particles detach after reaching some critical diameter. In the case of the later, low attachment rate can be explained by the fact that larger $CoFe_2O_4$ particles lead to formation of larger Ag particles, which was observed earlier in subchapter **5.1.2.4**.

51
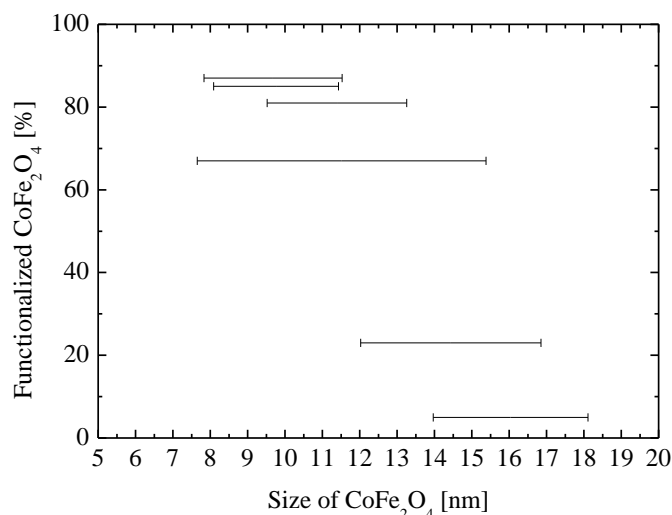
Figure 5-12. Correlation between the functionalization degree of CoFe$_2$O$_4$ with Ag and its diameter.

5.2. Kinetics of the Ag@CoFe$_2$O$_4$ formation for different synthetic approaches

In order to better understand the mechanism of formation of the dumbbell-like particles, kinetic experiments were performed for both synthetic approaches. The resulting particles were investigated by means of UV-vis spectroscopy, and selected samples were investigated by TEM.

Figure 5-13 shows the TEM images taken after 30, 60 and 120 min for the particles synthesized in tetralin from **CFO-310** (the synthesis was performed at 100 °C with concentration of CoFe$_2$O$_4$ 0.8 mg·ml^{-1} and concentration of Ag 0.1 mg·ml^{-1}). From TEM images the information on the geometric size of the attached particles, functionalization degree of CoFe$_2$O$_4$ and attachment degree of Ag (calculated as the percentage of Ag particles attached to CoFe$_2$O$_4$ from all Ag particles found on the image). TEM images show that after 30 minutes several smaller Ag particles per CoFe$_2$O$_4$ particle can be found. With the time the number of Ag particles per CoFe$_2$O$_4$ particle decreases, while the size of the Ag particles increases from 2.5 nm ± 0.8 nm to 3.1 nm ± 0.7nm. After 120 minutes the number of CoFe$_2$O$_4$ particles functionalized with Ag counterpart is as low as 10 %, no multiple Ag

particles on a CoFe$_2$O$_4$ particle are found, and the size of the Ag particles reaches 4.9±1.7 nm. It is important to mention, that free Ag particles are observed along the whole synthesis progress.
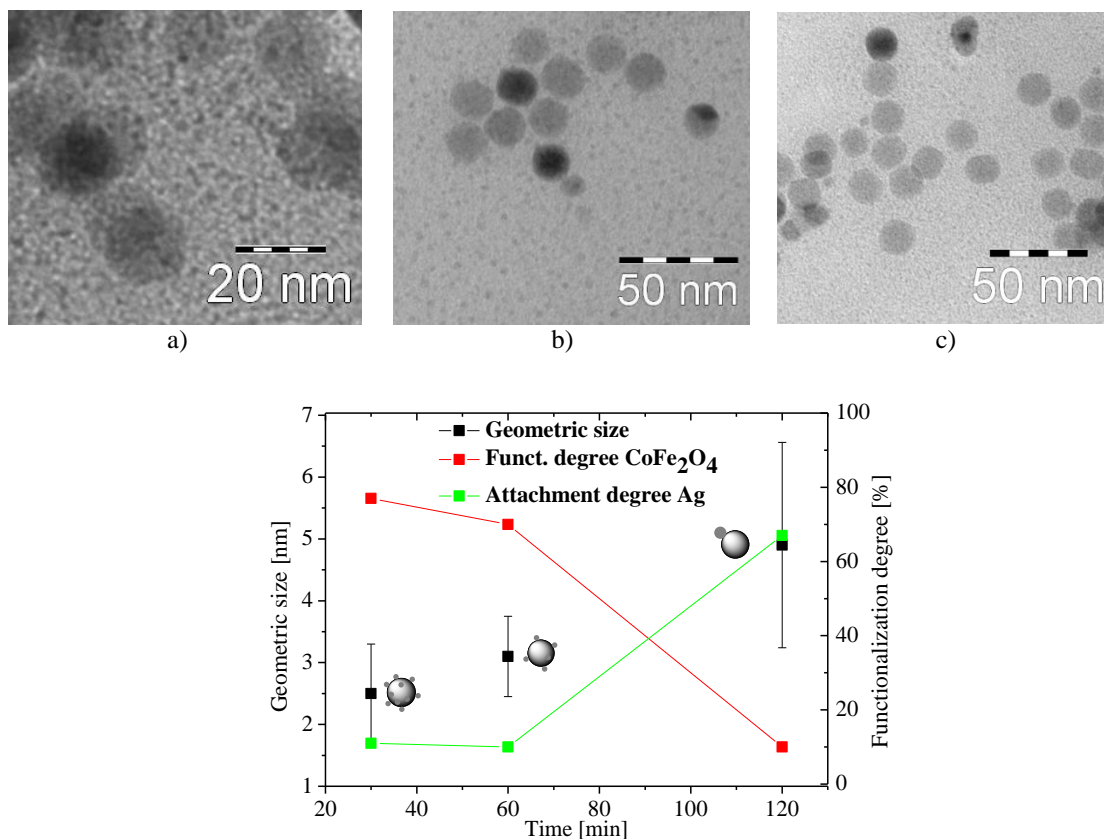
Figure 5-13. Evolution of the particles architecture, depending on the time in tetralin. TEM images are taken after a) 30 min, b) 60 min, c) 120 min

Such behavior confirms the assumption of the Ostwald ripening nature of the dumbbells formation. Contrary to the theory proposed by Zeng and Sun[155], according to which only single growth site per particle is available due to the surface charge gradient, the observations above show results similar to the formation of Ag particles on the surface of Fe/Fe$_x$O$_y$ particles, where amorphous Fe$_x$O$_y$ provides multiple growth sites for Ag nanodomains.[84] Ag atoms are known to have high mobility on metallic and metal oxide surfaces[156,157] at high temperatures, resulting in ripening of the most stable Ag domain on the particle by consuming the others leading to a dumbbell formation. According to data obtained from

XRD and VSM measurements of the sample CFO-310, the CoFe$_2$O$_4$ particles have a low content of crystal phase and low saturation magnetization. This might indicate a presence of the amorphous phase on the surface of the particles, which might make multiple growth site occurrences per particle possible. Thus, the reaction mechanism seems to be determined not only by reaction conditions, but also by the properties of the primary particles involved in the reaction.

The UV-vis spectra presented on **Figure 5-14** of the kinetic experiment show the appearance of the signals at 410 nm and 437 nm right after the injection of the Ag salt. The signal decays with time and almost vanishes after 30 min. The signal at 410 nm corresponds to particles of size of about 5-10 nm, whereas the signal at 437 nm corresponds to larger particles (surface plasmon resonance and optical properties will be discussed more detailed in **Chapter 5.3.1**). This is in accordance the TEM observations, where smaller particles are followed by ripening into the fewer bigger particles.
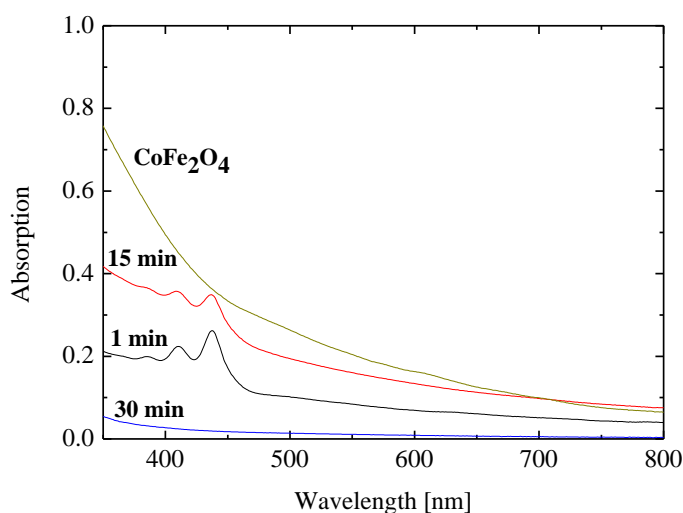
Figure 5-14. UV-vis spectra of the particles during the kinetic experiment in tetraline.

The kinetic experiment for the reaction in toluene with oleylamine shows a slightly different course of the reaction. The reaction was performed at 70 °C for 24 hours with precursor

concentration ratio 1:1.8 (sample **DLP-70/24h 1:1.8 III**). **Figure 5-15** shows the TEM images of kinetic experiments in toluene after 15 min (a), 8h (b) and 24h (c). Unlike in the reaction in tetralin, in this synthetic approach multiple growth sites on CoFe$_2$O$_4$ particles are not observed. In the course of the reaction, the Ag particles on the surface of the CoFe$_2$O$_4$ particles become larger until reaching a certain critical size. Parallel to this, occurrence of free Ag particles in the solution is observed. These free Ag particles grow then along with the particles on the surface of CoFe$_2$O$_4$ particles.
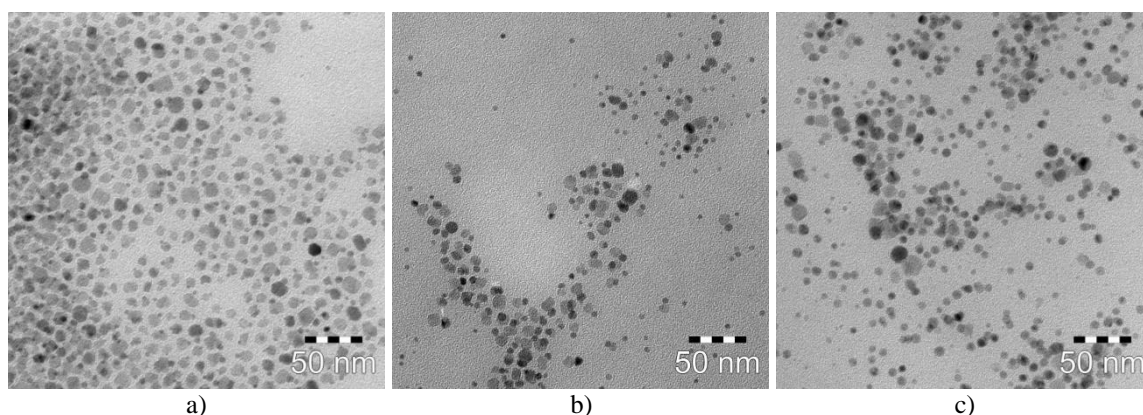
Figure 5-15. TEM images of kinetic experiment in toluene after 15 min (a), 8h (b) and 24h (c).

There are two proposed mechanisms of Ag nucleation: the first one admits the homonucleation of Ag particles in the solution. The second mechanism admits that Ag can nucleate only heterogeneously on the surface of CoFe$_2$O$_4$ particles. The observed free Ag particles are then the particles which detached from CoFe$_2$O$_4$ particles in the course of the reaction and continued to grow in the solution. However, the geometric size distribution of attached Ag particles is relatively narrow and correlates with the size of the primary CoFe$_2$O$_4$ particles they are attached to, meaning that all the attached Ag particles should have started to grow in the same moment. This makes the first proposed mechanism more likely.
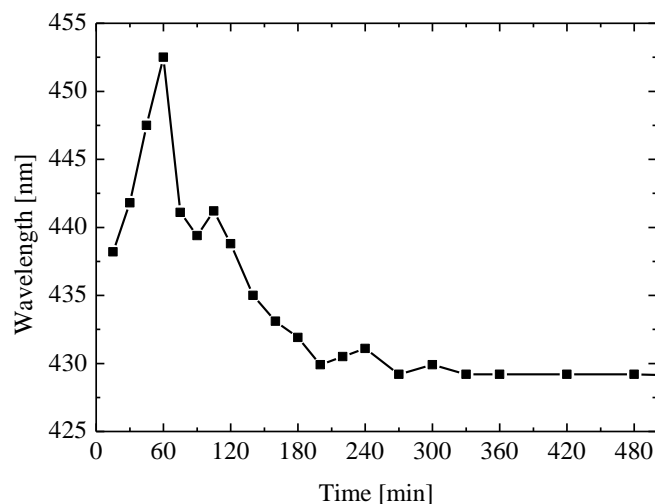
Figure 5-16. Shifting of the absorption peak of the sample DLP-70/24h with time.

Figure 5-16 shows the changing of the position of the UV-light absorption peak in course of the experimental is shown. In the beginning of the reaction the signal is observed at 438 nm, shifting with time up to 452 nm after 60 minutes. After reaching the longest wavelength, peak position shifts back with time until wavelength of 430 nm is reached. The shift to the longer wavelength in the first 60 minutes might correspond to the growth of the particles on the surface of CoFe₂O₄ particles. The subsequent shift back should indicate the nucleation of the free Ag particles in the solution. Since the number of smaller free Ag particles is higher than of attached Ag particles, the absorption peak intensity of the latter is lower.
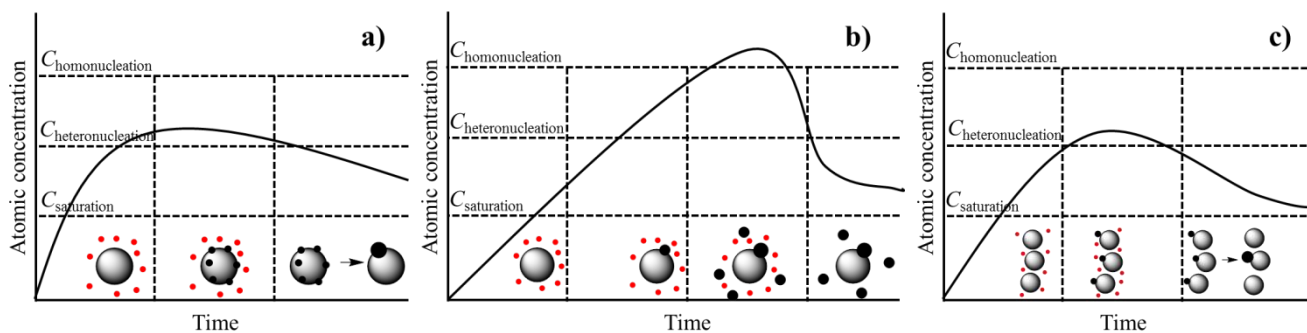
Figure 5-17. Proposed dumbbell formation mechanism for synthesis in tetralin (a), synthesis in toluene (b) and synthesis in toluene with Ag salt deficiency (c); grey spheres: CoFe₂O₄, black dots: Ag particles, red dots: Ag⁰/Ag⁺ monomers.

To sum up the information on the dumbbells formation mechanisms, schematic concepts are presented in **Figure 5-17**. The syntheses in tetralin in absence of large amounts of reducing agent, such as oleylamine lead to a very reluctant formation of dumbbell-like particles. The slow speed of the reaction makes it possible to investigate the growth and nucleation mechanisms. In the syntheses, in which the primary magnetic nanoparticles with an amorphous phase are involved, the formation of the so-called "raspberry" structures is being observed, followed by Ostwald ripening, leading to a dumbbell-like structure. The synthesis in toluene with oleylamine with highly crystalline primary nanoparticles involved results in immediate dumbbell-like structure of the particles. If the concentration of the Ag precursor is sufficient for steady formation of the Ag atoms in the solution (marked red on the scheme) the critical nucleation concentration is reached and formation of unattached Ag particles occurs. If, however, the source of Ag atoms depletes and the reaction is not stopped by cooling the reaction medium to room temperature, not only the formation of the free Ag particles does not take place, but also Ostwald ripening process starts. In this case the smaller Ag particles are being consumed by the bigger Ag particles, despite their attachment to CoFe$_2$O$_4$ particles. This mechanism is rather peculiar, since the case in point is not the Smoluchowski ripening (which is known for Ag particles at metallic surfaces[158]) and not an Ostwald ripening on the surface of a single CoFe$_2$O$_4$ particle, but something, that could be named "interparticle ripening", when several attached Ag particles take place in the ripening process.

5.3. Physical properties of the Ag@CoFe$_2$O$_4$

5.3.1. Surface plasmon resonance of the attached Ag particles

An important property of the Ag@CoFe$_2$O$_4$ particles is the plasmon resonance of the Ag particle, which can be detected by means of UV-vis spectroscopy. Particles in the solution, as

well as particles on the surface of cobalt ferrite absorb light in the range between 410 and 425 nm,[92],[153] giving a yellow shade to a normally black dispersion. When the silver particles are destabilized (by the lack of the surface groups, for example), they agglomerate, with disappearing light absorption (the shade color turns from yellow to red to finally disappear). The degradation of the silver particles can be observed, when a sample of Ag@CoFe$_2$O$_4$ (sample **DLP-70/24h 1:1.8**) was dissolved in toluene without oleylamine, which serves as a surfactant, protecting the Ag counterparts. Seven subsequent measurements were done, each measurement starting in 2 minutes after the end of the previous (the measurement lasts about 1 min). On **Figure 5-18** can be seen, that the intensity of the signal drops, and the signal broadens. The position of the peak is shifted to the shorter wavelength, which is not expected, since the larger particles absorb light at the longer wavelength. However, if the particles agglomerate over the Ostwald ripening, both smaller and bigger particles are expected to be found in the solution in course of the ripening process. Since the smaller particle should show higher absorption intensity due to their higher surface/volume ratio, the shift of the intensity maximum to shorter wavelength along with signal broadening can be explained.
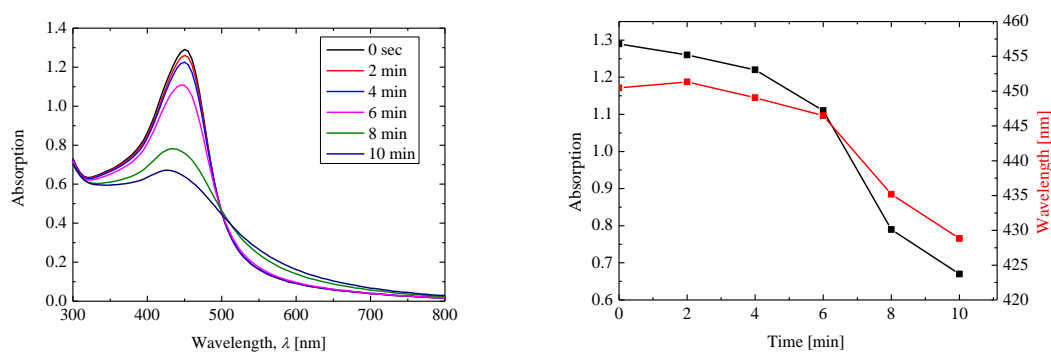
Figure 5-18. UV-vis spectra of the particles, destabilized by the lack of surface agent and shifting of the absorption peak wavelength (black) and intensity (red).

This observation, combined with the experience gathered during the synthesis optimization, leads to the conclusion that the oleylamine surface groups are in equilibrium with the

oleylamine groups in the solution. The lack of oleylamine in the solution leads to the depletion of the surface groups on Ag causing the agglomeration and further detachment from CoFe$_2$O$_4$.

Figure 5-19. Visible color change for the destabilized sample (II), caused by Ag agglomeration.

5.3.2. Magnetic properties of the Ag@CoFe$_2$O$_4$ particles

To investigate the magnetic properties and the change in the magnetic behavior after attachment of Ag particles VSM measurements are performed. **Figure 5-20** presents the comparison between the magnetization curves of the dumbbell-like particles and the pure CoFe$_2$O$_4$ particles that are used as source for the synthesis of the dumbbell-like particles. On **Figure 5-20 a)** the magnetization curves of samples **CFA-280/2h×5** and **DLP-70/24h 1:1.8 II** and on **Figure 5-20 b)** the magnetization curves of samples **CFA-280/2h×2** and **DLP-70/24h** 1:1.8 III are presented. The shape magnetization curve of the decorated particles is similar to that of the cobalt ferrite particles source for both sample pairs. The behavior in low field range is different. For samples **CFA-280/2h×5** and **DLP-70/24h 1:1.8 II** remanence magnetization M_r/M_s drops from 0.16 to 0.08 and coercivity H_c drops from 12.8 kA·m^{-1} to 4.3 kA·m^{-1}. The value of d_{mag} changes insignificantly from 9.7 nm to 9.5 nm. For samples CFA-280/2h×2 and **DLP-70/24h 1:1.8 III** the M_r/M_s and H_c values do not change after Ag attachment ($M_r/M_s = 0.09$, $H_c = 5.9$ kA·m^{-1}). The value of d_{mag} increases from 7.1 nm to 10.0 nm. The calculation of the saturation magnetization shows, that after normalization on the

59

mass of the magnetic material (CoFe$_2$O$_4$) in the particles the value of the M_s corresponds only to 55 % and 28 % of the value of the primary magnetic particles for the first and the second pair of samples respectively. This comes in contradiction to the data found in literature [91,127] claiming, that the saturation magnetization of the dumbbell-like particles is higher, than that of the pure cobalt ferrite. The source literature, in which Ag@CoFe$_2$O$_4$ are also presented, contains no clear TEM images of the dumbbell-like structures from which we could compare the ones here synthesized.
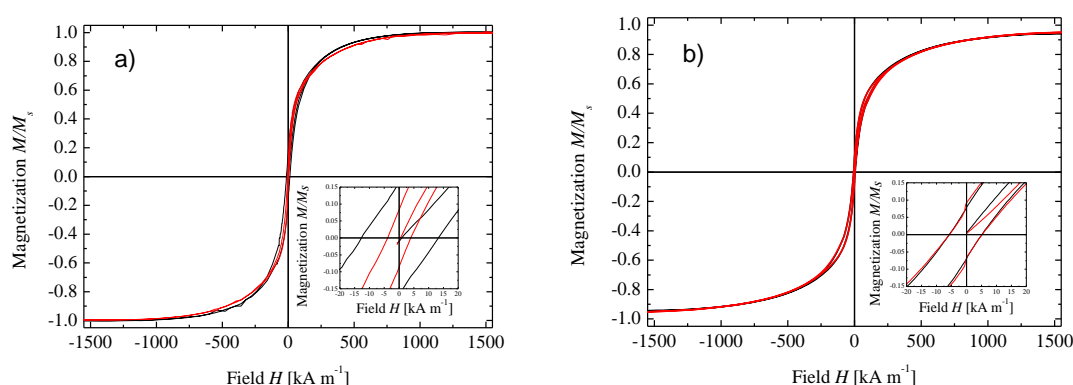
Figure 5-20. Comparison between the magnetization curves of the dumbbell-like particles (red) and the primary CoFe$_2$O$_4$ particles that were used as source for the synthesis of the dumbbell-like particles (black) for samples a) CFA-280/2h×5 and DLP-70/24h 1:1.8 II and b) CFA-280/2h×2 and DLP-70/24h 1:1.8 III

The magnetic properties of the particles are a useful tool for handling the dispersions. The magnetic separation of destabilized particles in toluene/ethanol mixture enables removing the unattached silver particles as can be seen in **Figure 5-21** which shows TEM images comparing the silver dumbbell-like structures before and after removing the excess of unattached silver particles utilizing the magnetic properties of cobalt ferrite.
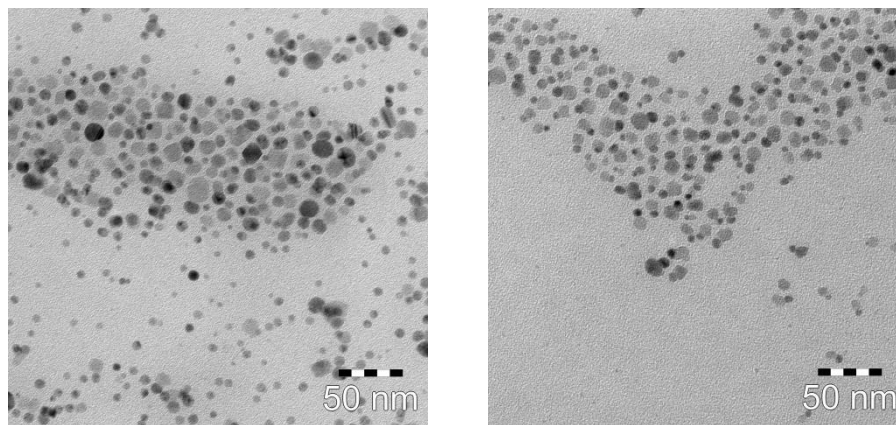
Figure 5-21. Removing the excess of unattached silver particles utilizing the magnetic properties of cobalt ferrite.

5.3.3. Crystal structure of Ag@CoFe$_2$O$_4$

An XRD measurement was performed in order to investigate the crystal phases of the Ag@CoFe$_2$O$_4$. **Figure 5-22** presents the XRD-measurement of the sample **DLP-70/24h 1:1.8**. The reflexes are very clear and can be attributed to the reflexes of pure cobalt ferrite and pure Ag. No unidentified reflexes were found, stating, that no mixed interphase between cobalt ferrite and silver is formed.
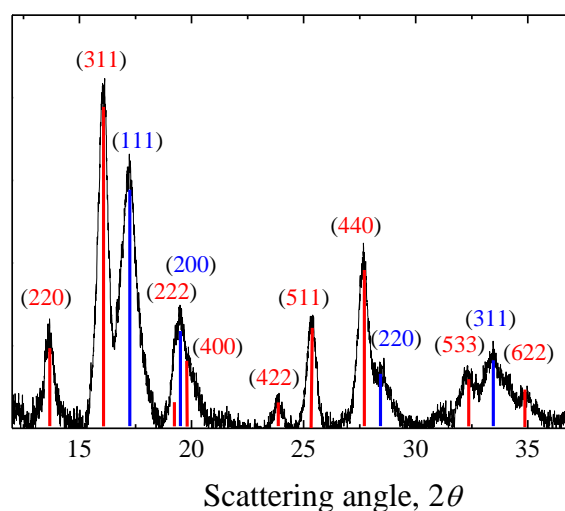
Figure 5-22. XRD-measurement of sample DLP-70/24h 1:1.8, red bars for CoFe$_2$O$_4$ reflexes, blue bars for Ag reflexes.

The fact, that no other phases are found, except for CoFe$_2$O$_4$ and Ag, brings no explanation of the low saturation magnetization of the sample. Since there is no change in the crystal structure of the sample after the functionalization, there might be a change in the magnetic ordering in CoFe$_2$O$_4$ near to the interphase.

The Mössbauer spectroscopy measurements of sample **DLP-70/24h 1:1.8 III** and source CoFe$_2$O$_4$ particles CFA-280/2h were performed at 4.3 K in the applied magnetic field of 5T. Sample CFA-280/2h was additionally measured at zero field for comparison. The spectra are shown on **Figure 5-23**. The spectrum of sample CFA-280/2h shows a clear spinel structure with A (tetrahedral) and B (octahedral) sub-spectra. The spectrum at 5T shows, that the magnetic moment are aligned along the field. Magnetization of the dominating B-sublattice follows the external field and hyperfine field and spin are antiparallel to the external field. The intensities of lines 2 and 5 are angle-dependent. The lines have a relative intensity, corresponding to an angle of 23° between the spin orientation and the vector of the applied magnetic field.

The spectrum of sample **DLP-70/24h 1:1.8 III** is similar to the spectrum of **CFA-280/2h**. The spectrum of Ag@CoFe$_2$O$_4$ particles has lower signal-to-noise ratio. Judging from the intensities of the lines 2 and 5, the spin-canting is higher for the dumbbell-like particles (25° vs 23° for the pure CoFe$_2$O$_4$ particles). This can be caused by a slight spin frustration at the contact site between Ag and CoFe$_2$O$_4$. Along with the sub-spectra, observed also for sample **CFA-280/2h**, sample **DLP-70/24h** 1:1.8 shows a slight unstructured contribution in the middle of the spectrum. This can be a signal of the paramagnetic iron atoms, suppressed by a strong external magnetic field.
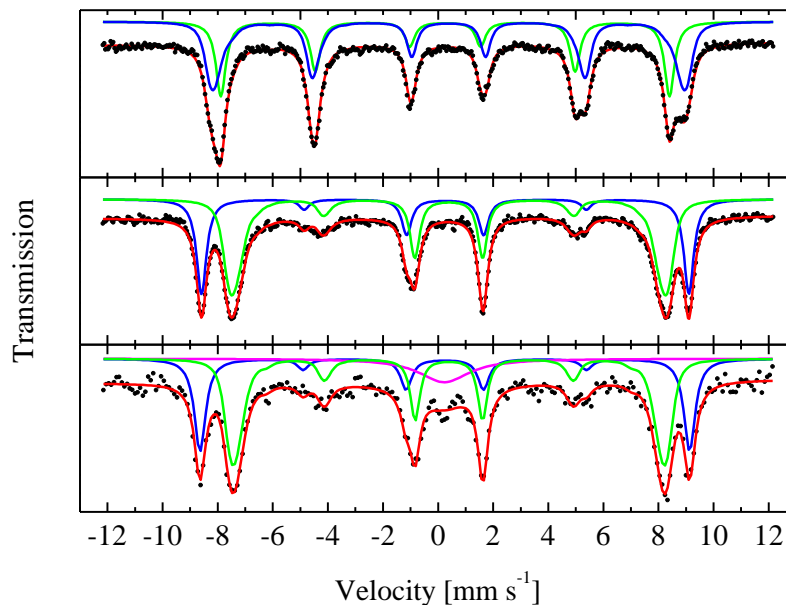
Figure 5-23. Mössbauer spectra measured at 4.3K for Ag@ CoFe₂O₄ particles and source CoFe₂O₄ particles: CFA-280/2h at 0T (above), CFA-280/2h at 5T(middle), DLP-70/24h 1:1.8 (below); measurement points (black), fitted curve (red), tetrahedral sublattice A (blue), octahedral sublattice B (green),

5.3.4. Hydrodynamic properties of Ag@CoFe₂O₄ in toluene

The hydrodynamic properties were investigated by means of DLS and AC-Susceptometry. The results were compared with data obtained from the measurements of the source CoFe₂O₄ particles. The samples show no sign of agglomeration or particles degradation with time. The hydrodynamic diameters calculated from both DLS and AC-Susceptometry measurements are increased for the Ag@CoFe₂O₄ particle (see **Figure 5-24**) as expected.
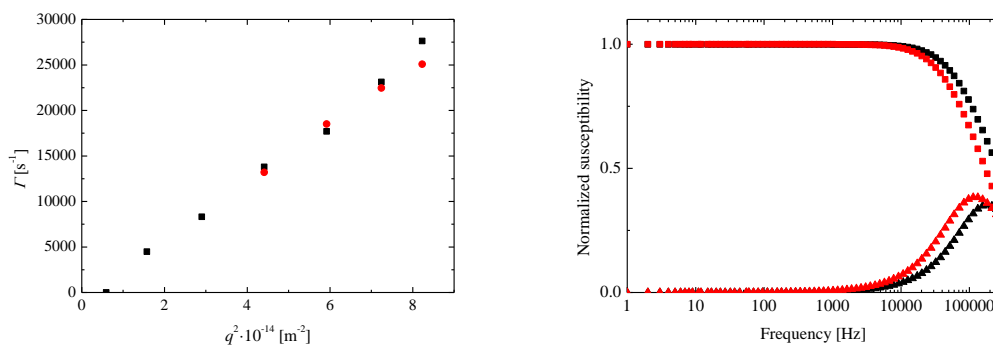
Figure 5-24. Γ vs q^2 plots and AC-Susceptometry curves for Ag@CoFe$_2$O$_4$ (red; sample DLP-70/24h 1:1.8 III) and their source CoFe$_2$O$_4$ particles (black; sample CFA-280/2h×2).

5.4. Summary on the synthesis of the dumbbell-like Ag@CoFe$_2$O$_4$ particles

The particles synthesized using the synthetic approach developed by S. Sun[92] resulted in a low functionalization degree of the CoFe$_2$O$_4$ particles and was considered inefficient. It was not possible to optimize the method to obtain the particles with the desired properties. The performed syntheses were however essential for understanding the formation mechanism, particularly for syntheses, where CoFe$_2$O$_4$ particles synthesized by oleate complexes thermal decomposition were involved. The latter are considered unsuitable for the synthesis of the dumbbell-like particles due to the multiple growth sites occurring in the reaction on their surface.

The synthetic approach proposed by Klajn[93] is a much more convenient way in obtaining the dimeric particles. The reaction parameters can be adjusted to influence the size of the resulting Ag particles, and to keep the functionalization rate above 80 %. The variation of the reaction parameters along with kinetic experiments also made possible to propose a formation mechanism of the particles. The CoFe$_2$O$_4$ particles synthesized using acetylacetonate complexes decomposition proved to be a reliable basis for the stable dumbbell-like particles, however, the size of the CoFe$_2$O$_4$ particles, which can be used for functionalization is limited from above.

The physical properties of the particles important for the further purposes were investigated. The magnetic properties of Ag@CoFe$_2$O$_4$ are suitable to involve the particles in the further experiments. The optical property of the particles, namely surface plasmon resonance, is an essential characteristic because even though on one hand the light absorption at 420 nm prevents the use of the higher intensity blue-laser powered light scattering instruments due to increased local heating, which would affect the measurement, on the other hand SRP allows tracking the changes in the particles architecture without the necessity of TEM measurements. Despite a decrease in the saturation magnetization, the particles retain their ferromagnetic behavior and their hydrodynamic properties can be investigated by means of AC-Susceptometry. Moreover DLS not only confirmed the results observed by AC-Susceptometry but also allowed to obtain the diffusion coefficients of the dumbbell-like particles.

The samples synthesized in toluene with oleylamine were involved in further experiments with polymer functionalization and transferred into the aqueous medium.

6. Synthesis and modification of the asymmetric hybrid particles

To obtain objects, which would combine the properties of the magnetic material with the properties of soft matter, the dumbbell-like particles synthesized in **Chapter 5** are functionalized with polymer chains. The functionalization with polymer exploits the asymmetric architecture of the dumbbell-like particle attaching selectively to the noble metal counterpart ending in the flagella-like distribution on the surface of the particles, rather than the brush-like distribution. The selectivity is obtained by the functionalization of the polymer chain with a thiol group allowing it to attach rather to Ag, than to $CoFe_2O_4$. The synthesis of such functionalized polymers and their attachment to the dumbbell-like particles is discussed.

6.1. Synthesis and characterization of the thiol-functionalized polymer

In this chapter the synthesis and characterization of the polymer with a thiol end-functional group is discussed. To meet the set requirements the polymer should possess certain hydrodynamic and chemical properties. The choice of the polymer is based mainly on its persistence length denoting the chain stiffness and its solubility in various solvents. Poly(tert-butylacrylate) (P(t-BuA)) is chosen as a precursor to polyacrylic acid (PAA), the ionization degree of which can be controlled in aqueous media by adjusting the pH.[159] Polyethylene glycol (PEG-SH) is commercially available in thiol-modified form and is suitable for attachment to the particle in both organic and aqueous solution. However, its high flexibility limits its utility for the hydrodynamic measurements. The molar mass of the synthesized polyacrylates ranges from 1000 $g \cdot mol^{-1}$, where the number of monomers is low enough to detect the signal of functional groups in NMR-spectroscopy, to 10 000 $g \cdot mol^{-1}$, what is enough for the stretched polymer chain to exceed the size of the dumbbell-like particle.

6.1.1. Synthesis of poly(tert-butyl acrylate) polyacrylic acid polymers with a functional thiol group

Poly(tert-butylacrylate) with different molar masss are synthesized over the atom-transferred radical polymerization (ATRP) using the technique described by Colombani.[160] ATRP is characterized by narrow molar mass distribution due to simultaneous growth process of the polymer chains in the reaction.[111] The concentration of free radicals in the reaction is low, thus termination reactions such as recombination and disproportionation do not take place. Another important advantage of ATRP is that the functional halogen group remains intact after the polymerization and can be further replaced by other functional group such as thiol group. The functionalization with the thiol group is achieved by reaction of a polymer with a bromine end functional group with thiourea. This is a S_N2 reaction, which is relatively slow for the leaving group at secondary carbon.[161] The hydrolysis of poly(tert-butylacrylate) is performed by adding concentrated trifluoroacetic acid (TFA) to the polymer solution.
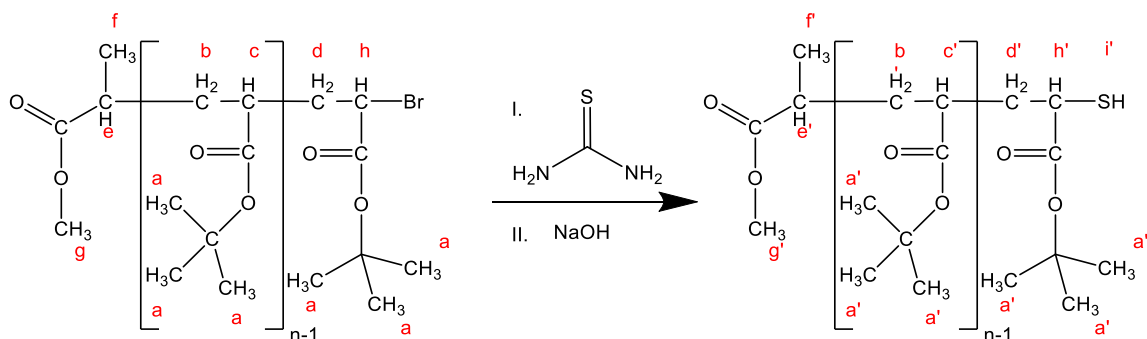
Figure 6-1. Reaction mechanism of P(t-BuA) thiolation

To get more information on the thiolation process of polyacrylates, poly(tert-butyl acrylate) with molar mass $M_w = 1000$ g·mol^{-1} was synthesized. The polymer was later put in reaction with TFA to investigate the preservation of thiol group during the hydrolysis. The synthesized polymer and its thiolated derivative were analyzed by Gel permeation chromatography (GPC). The molar mass distribution curve shows presence of the oligomers (sawtooth signal on **Figure 6-2**), which is typical for the polymers with low molar mass. One

monomer unit of poly(tert-butyl acrylate) has a molar mass of 128 g·mol^{-1}. The synthesized polymer with molar mass M_w of 1600 g·mol^{-1} contains about 12.5 monomer units. The polydispersity index *PDI* is 1.28, which is higher than expected for such polymers.[160] It was unable to obtain results for **PAA-SH 1k** using GPC, due to the carboxylic groups interacting with the chromatographical column.

The NMR-spectra of the primary poly(tert-butyl acrylate) and its thiolated derivative are shown on **Figure 6-3**. For calculation of the molar mass of the polymers the signal of the protons in the initiator methyl ester group (g' on the figure) was taken as a reference. The signal of these protons is a clear singlet, which is not overlapped by any other signals neither in P(t-BuA), nor in PAA. The molar masss calculated from GPC and NMR are compared in **Table 6-1**.
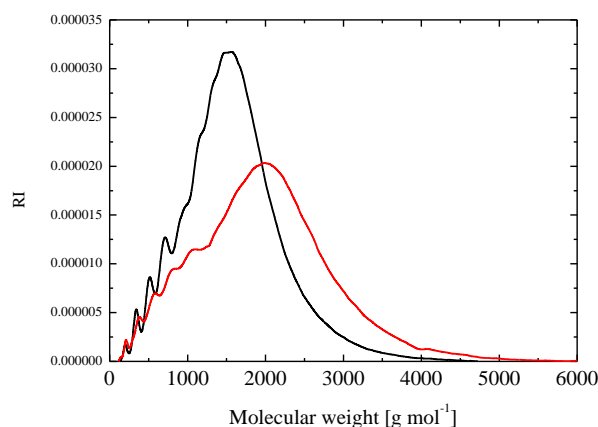
Figure 6-2. Molar mass distributions measured by GPC for P(t-BuA)-SH 1k (red) and P(t-BuA) 1k (black)
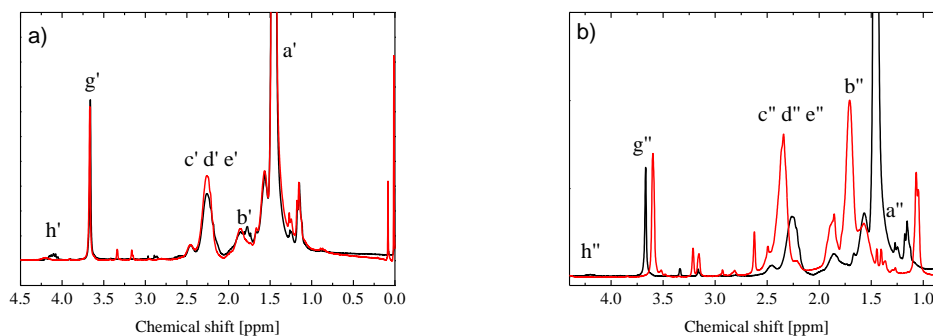
Figure 6-3. a): [1]**H NMR spectra of the P(t-BuA)-SH 1k (red) and P(t-BuA) 1k (black); b):** [1]**H NMR spectra of PAA-SH (red) 1k and P(t-BuA)-SH 1k (black).**

The ^{1}H NMR signals were attributed according to data, found in literature for poly(tert-butyl acrylates)[160] and with the help of AIST SDBS spectra and spectra predicted using ChemBioDraw Ultra 12.0. For **P(t-BuA) 1k** the multiplet signal of a proton h at carbon atom adjacent to the bromine group at 4.11 ppm loses its intensity and is shifted to 4.2 ppm. No new signals are observed, except for the doublet at 3.17 ppm and 3.34 ppm arising from the rest of the dimethyl formamide.[162] The ratio between the intensities of the reference protons of the metoxy group g and of the proton c in the monomer does not change, indicating that no side reaction with the initiator group took place. The elemental analysis shows the content of sulfur of 1.85%, corresponding to yield of 88%.

To cleave the tert-butyl groups from the polymer, thiolated poly(tert-butyl acrylate) was solved in dichloromethane and an excess of TFA was added. The ^{1}H NMR spectrum shows a loss of intensity of the signal at 1.75 ppm by 85%, indicating successful hydrolysis of the polymer. Elemental analysis shows 0.88% of sulfur in the polymer, corresponding to 23% of functionalized chains.
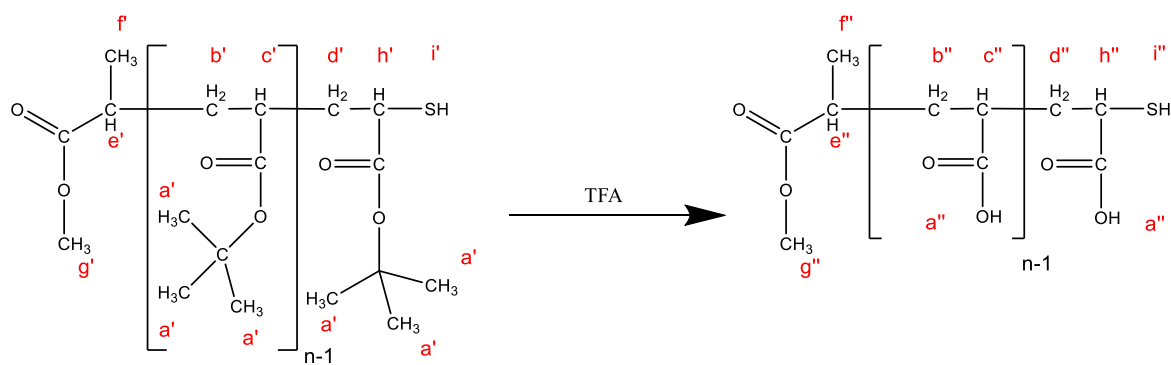
Figure 6-4. Hydrolysis of P(t-BuA)SH.

For further functionalization of the particles a polymer with the molar mass $M_w = 10000$ g·mol^{-1} was synthesized (**P(t-BuA) 10k**). The resulting polymer was thiolated the same way as was **P(t-BuA) 1k**. GPC and ^{1}H NMR measurements of the polymers were done (see **Figure 6-6**). GPC measurements shows the molar mass M_w of 10000 g·mol^{-1}, corresponding to 78 monomer units. The PDI is 1.10, which is rather narrow. NMR-spectrum does not allow to indicate the signal of the initiator group, due to its low intensity. The elemental analysis shows the content of sulfur of 0.05%, corresponding to yield of 22%. This is much lower, than the reported 98% yield for the published synthesis of thiolated polystyrene.[161] The reason for the low yield might be the steric hindrance, impeding the approaching of thiourea and formation of the transition state structure.
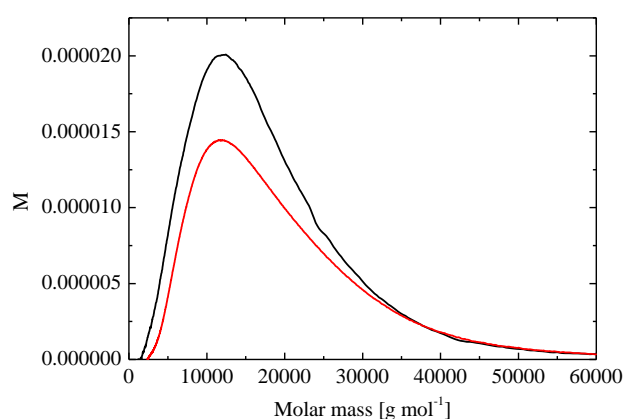
Figure 6-5. Molar mass distributions measured by GPC for P(t-BuA)-SH 10k (red) and P(t-BuA) 10k (black).
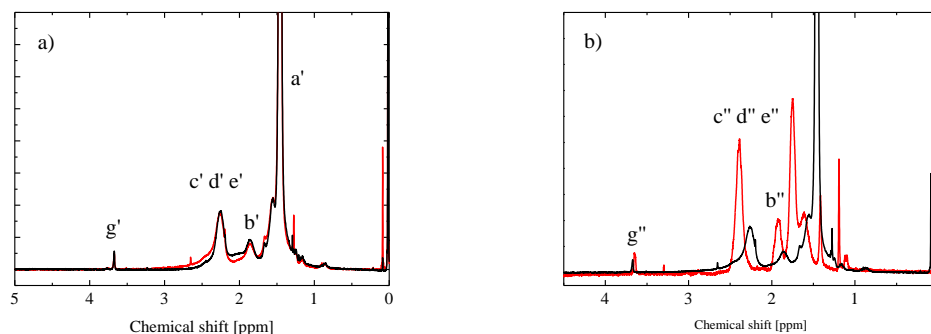
Figure 6-6. a): ¹H NMR spectra of the P(t-BuA)-SH 10k (red) and P(t-BuA) 10k (black); b): ¹H NMR spectra of PAA-SH (red) 10k and P(t-BuA)-SH 10k (black).

The ^{1}H NMR spectrum of the hydrolyzed polymer shows a drop of intensity for protons of tert-butyl group by 98 %, indicating successful hydrolysis. The molar mass drops from 9200 $g \cdot mol^{-1}$ to 5800 $g \cdot mol^{-1}$, as calculated from NMR, because of the cleavage of tert-butyl groups. This is somewhat higher than the expected value of 5100 $g \cdot mol^{-1}$. The elemental analysis shows sulfur content of 0.08 %, indicating that 18 % of chains are functionalized with thiol group.

To investigate the chemical structure of the polymers, investigations by means of FTIR and Raman spectroscopies were performed. FTIR-spectroscopy gives information on the chemical bonds, present in the molecule. However, not all the bonds give a strong signal in the IR-spectrum. To complement this, Raman spectroscopy is involved. Particularly, S-H bond shows only a weak signal in the IR spectra, but a strong one in the Raman spectra. **Figure 6-7** shows FTIR and Raman spectra for sample **P(t-BuA)SH 10k**. The signal-to-noise ratio is rather low, however a small signal can be distinguished at 2550 cm^{-1}, where the signal of the S-H bond is expected. The Raman spectra of the other samples show even stronger noise, and no information can be obtained from them.
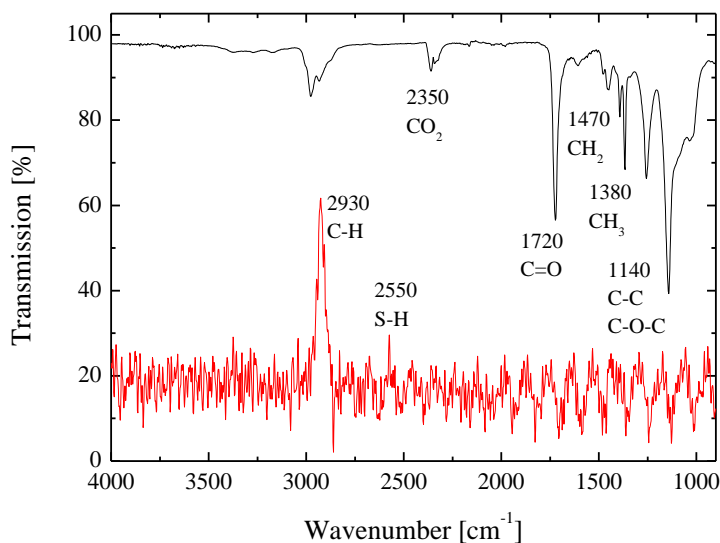
Figure 6-7. FTIR (black) and Raman (red) spectra of the P(t-BuA)SH 10k.

Table 6-1. The molar mass values for P(t-BuA) and its thiolated derivatives.

Sample Name	M_n	M_w	PDI	M_{NMR}
P(t-BuA) 1k	1250	1600	1.28	1250
P(t-BuA)SH 1k	1650	2300	1.39	1500
PAA-SH 1k	-	-	-	
P(t-BuA) 10k	9100	10000	1.10	10700
P(t-BuA)SH 10k	10000	13800	1.37	9200
PAA-SH 10k	-	-	-	5800

6.1.2. Summary on the synthesis of the thiol-functionalized polyacrylic acid

The thiol-functionalized polymer, intended for the further attachment to the particles, synthesized in **Chapter 5** was synthesized. Though the yield of the thiolated form of the polymer is lower, than expected, the unfunctionalized polymer is expected not to attach to the Ag@CoFe$_2$O$_4$ particles and be removed by magnetic separation.

6.2. Synthesis and modification of the asymmetric hybrid particles

In this chapter functionalization of the dumbbell-like particles with polymer synthesized in **Chapter 6.1** is discussed. Polymer attachment reaction is investigated for polyacrylic acid in aqueous solvents and for polyethylene glycol in both organic and aqueous solvents. The functionalized particles are investigated by means of IR spectroscopy, UV-vis spectroscopy, Dynamic light scattering, AC susceptometry, elemental analysis and TEM. For further

investigation of hydrodynamic properties of the polymer functionalized $Ag@CoFe_2O_4$ particles measurements at different pH values are planned. To achieve this purpose, experiments on transferring the particles into aqueous media with different surface agents are performed.

6.2.1. Functionalization of the dumbbell-like particles with polymer flagella

To create an asymmetric hybrid system, combining the properties of a hard magnetic particle and of a soft polymer, the dumbbell-like particles with shape anisotropy described in **Chapter 5** were synthesized and combined with the polymer, carrying the thiol functional end group, synthesized in **Chapter 6**. This combination occurs through the specific attachment of the thiol group of the polymer with the noble metal counterpart of the dimeric particle. The molecules with thiol groups first physically adsorb on the surface of Ag particles and then a sulfur-metal bond is created.[161] In this subchapter the attachment of the thiol group to a dimeric particle will be discussed.

6.2.1.1. Optimization of the polymer amount

The initial experiments have shown, that when an excess of the polymer is added into the particles dispersion, Ag particles agglomerate and dumbbells dimeric structures degrade. The number of polymer chains per a dumbbell-like particle (F_c) was calculated from equation **(6-1)** basing on the sulfur mass fraction value in polymer, obtained from elemental analysis and on the number of the particles,

$$F_c = \frac{N_p}{N_d} \cdot f_S \qquad \text{(6-1)}$$

$$N_p = \frac{m_p}{M_w \cdot N_A} \qquad \text{(6-2)}$$

$$N_d = \frac{6 \cdot m_d}{\rho_{CoFe_2O_4} \cdot \pi \cdot d^3} \qquad \text{(6-3)}$$

where N_p is the number of polymer chains, N_d the number of the dumbbell-like particles, f_S content of thiol-functionalized polymer chains, m_p the mass of the added polymer, M_w molar mass of the polymer, N_A the Avogadro constant, $\rho_{CoFe_2O_4}$ density of bulk cobalt ferrite, $d_{CoFe_2O_4}$ is the diameter of the cobalt ferrite particle, obtained from TEM measurements, then surface polymer density (F_S) is calculated as

$$F_S = \frac{F_C}{4 \cdot \pi \cdot d_{Ag}} \qquad \text{(6-4)}$$

where d_{Ag} is the diameter of the silver particle, attached to cobalt ferrite, obtained from TEM.

Figure 6-8 shows the TEM images of the dumbbell-like structures with different added amounts of P(t-BuA)SH 10k. It confirms the agglomeration of Ag particles, which can be also observed by eye. The same observation can be made when a small amount of thiourea is added to a dispersion of Ag@CoFe$_2$O$_4$, since a rapid loss of color is seen. The Ag agglomeration can be due to the reaction of the thiol group of thiourea with the silver replacing the surface groups and destabilizing the nanoparticles and therefore the same can be assumed for the functionalized polymer case. However, when the amount of the added polymer is low, the particles remain intact. Thus, after variation of the added polymer amount, an optimal amount of 200 chains per a particle is found, corresponding to approximately 3.2 chains per nm^2 of the Ag surface. This ratio is taken for all of the further functionalization approaches. To remove the unattached polymer from the solution, the particles are washed magnetically. Elemental analysis shows the sulfur content of 0.01 %, corresponding to app. 140 chains per a particle.

(a)   (b)
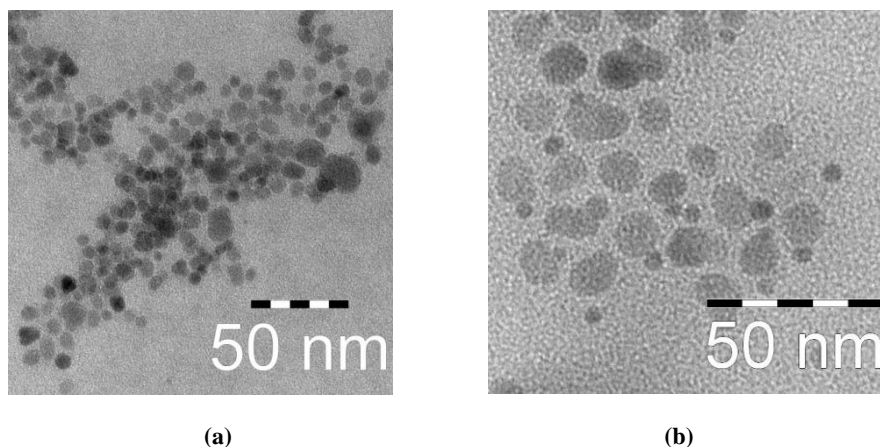
Figure 6-8. TEM images showing the stability of the dumbbell-like structures with different amounts of poly(tert-butyl acrylate)SH added: 2000 chains per Ag particle (a), 200 chains per Ag particle (b).

6.2.1.2.   FTIR spectroscopy analysis

To understand, how the thiol-functionalized polymer interacts with the particles, the particles are investigated by means of FTIR. The polymer is added to the particle dispersion in toluene and the particles are washed using magnetic separation. The particles are then redispersed in toluene again. A drop of the dispersion then is dried on the crystal of the FTIR instrument until no signal from the solvent is observed. The following measurements are compared: 1) pure polymer as powder, 2) dispersion of the dumbbell-like particles without the addition of the polymer and 3) dispersion of the $CoFe_2O_4$ particles with addition of the polymer and magnetic washing.

The spectra for the functionalization with thiolated polyethylene glycol and poly(tert-butyl acrylate) are shown on **Figure 6-9**. The spectrum of pure polyethylene glycol as well as of pure poly(tert-butyl acrylate) has a strong distinctive signal at 1100 cm^{-1}. No signals are found at this wavenumber for pure Ag@CoFe$_2$O$_4$ particles. The Ag@CoFe$_2$O$_4$ particles functionalized with PEG-SH retain the signal at 1100 cm^{-1} even after several magnetic washing, ensuring no unattached polymer remains in the solution. The same is observed for Ag@CoFe$_2$O$_4$ with poly(tert-butyl acrylate). On the other hand, a mixture of pure CoFe$_2$O$_4$

particles with thiolated polymer does not show any signals characteristic for polymer after magnetic washing.
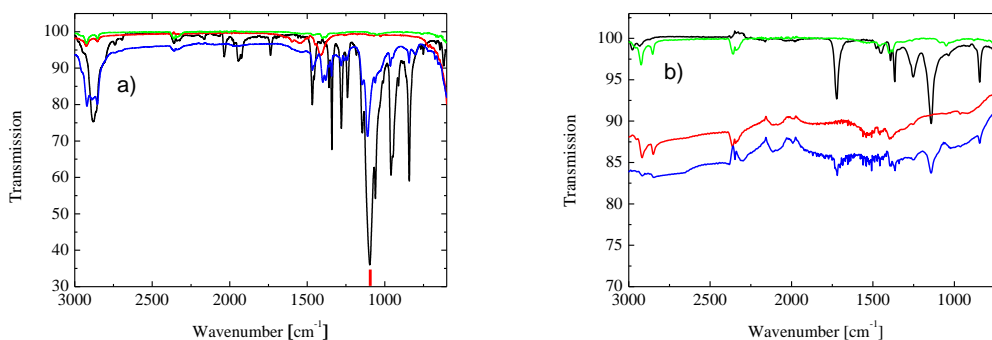
Figure 6-9. IR spectra of the polymer-functionalized particles, the pure polymer and the unfunctionalized particles; a): PEG-SH (black), Ag@CoFe$_2$O$_4$ (green), CoFe$_2$O$_4$+PEG-SH (red), Ag@CoFe$_2$O$_4$+PEG-SH (blue); b): P(t-BuA)SH (black), Ag@CoFe$_2$O$_4$ (green), CoFe$_2$O$_4$+ P(t-BuA)SH (red), Ag@CoFe$_2$O$_4$+ P(t-BuA)SH (blue).

The result of the FTIR spectroscopy proves that the polymer with a thiol end-group attaches successfully to a dumbbell-like particle, but does not attach to a pure CoFe$_2$O$_4$ particle. The fact, that only particles decorated with silver counterpart are suitable for polymer attachment, is an evidence of the different surface properties between Ag@CoFe$_2$O$_4$ and pure CoFe$_2$O$_4$ particles. This difference must be due to the fact that the adsorption rate on the silver particle is much higher than on the CoFe$_2$O$_4$ particle, or, more likely, that the adsorption on CoFe$_2$O$_4$ is not followed by a surface-metal bond, since it is known, that the thiol group readily creates a sulfur-metal bond with noble metals, such as silver, preceded by a physical adsorption, and replace the oleylamine groups with thiol groups[163]. This would lead to an asymmetric functionalization of the dimeric particle with polymer.

6.2.1.3. UV-vis analysis

The surface plasmon resonance of the Ag particle can be influenced by the molecules attached or adsorbed on its surface[164–167], since the wavelength of the absorption maximum and its intensity are dependent from the amount of the polymer added to the particles.[168]

Therefore UV-Vis measurements were performed to investigate the attachment of the polymer to the particles. The $Ag@CoFe_2O_4$ particles functionalized with PEG-SH or with PAA-SH were measured at the same concentration as the unfunctionalized $Ag@CoFe_2O_4$ particles. The absorption spectra are presented on **Figure 6-10**. The position of the peak was calculated as an intercept of the wavelength for the differentiated curve. It was found, that the position of the peak is shifted from 424.0 nm for unfunctionalized $Ag@CoFe_2O_4$ particles to 421.5 nm for $Ag@CoFe_2O_4$ with PAA-SH and to 426.0 nm for $Ag@CoFe_2O_4$ with PEG-SH. The peak intensity drops for $Ag@CoFe_2O_4$ with PAA-SH to 92 % of the pure $Ag@CoFe_2O_4$ and to 60 % for $Ag@CoFe_2O_4$ with PEG-SH. This decrease in the UV-vis absorption intensity data was also found in literature for gold nanoparticles functionalized with thiolated polymers.[168]
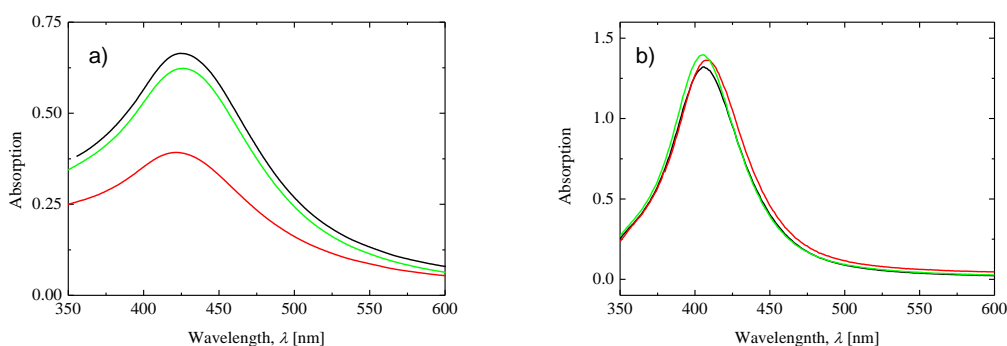
Figure 6-10. UV-vis spectra of the $Ag@CoFe_2O_4$ particles (a) and of the Ag particles (b) with no polymer (black), with PEG-SH (red) and with PAA-SH (green).

A blank experiment was performed with a dispersion of Ag particles in H_2O (stabilized with citric acid, $d = 20$ nm). To the particles dispersion the corresponding polymers with thiol group were added with the same ratio as for the $Ag@CoFe_2O_4$ particles. The wavelength shift of the absorption after functionalization with polymer has similar behavior as in case with $Ag@CoFe_2O_4$ particles. The Ag particles with no polymer show maximum in light absorption at 406.1 nm. The absorption wavelength of the particles functionalized with PEG-SH shifts to 408.2 nm and of the particles with PAA-SH to 404.8 nm. The absorption

intensity however does not drop as it was observed for Ag@CoFe$_2$O$_4$ particles, but it was raised by 3 % for PEG-SH and by 5 % for PAA-SH respectively. From literature it is known, that in general donation of electron density by chemisorbed ligands results in a blue-shift of the plasmon band position for a decrease in the particle size.[166] This was seen for electron density donation in the reaction of Ag with thiolates:[167]

$$C_nH_{2n+1}S^- + Ag_m^0 \rightarrow C_nH_{2n+1}S^{\partial-}Ag^{\delta+}Ag_{m-1}^{\partial-}$$
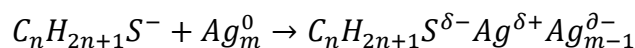
Where Ag_m^0 denotes zerovalent nanoparticles consisting of m atoms. A polarization (δ^+ and δ^-) results at the metal (M)/ligand (L) interface that depends on the character of the M−L bond, while electron density is shifted to the interior (∂^-). The red-shift is also known.[169] One of the reasons for a red-shift in the spectra is the oxidation of the silver particles. A thin layer of the oxidized Ag on the surface of the particles is enough to shift the adsorption maximum. The PEG-SH groups, while attaching to Ag particles substitute the oleylamine groups. Presumably, this leaves the Ag particles exposed to oxidation, ending in a thin layer of oxidized silver. The difference between PAA-SH and PEG-SH might lie in the speed of the exchange process and the extent of the exposure to oxidation during/after the attachment.

6.2.1.4. TEM analysis

To visualize the particles on the electron microscopy images, negative stains, such as osmium tetroxide (OsO$_4$) and phosphotungstic acid (H$_3$PW$_{12}$O$_{40}$) were applied. Osmium tetroxide is a well-known negative stain for soft matter.[170] High concentrations of OsO$_4$ staining normally lead to oxidation of the Ag particles.[171,172] The exposition time for 1% OsO$_4$ treatment was set to 60 minutes. It was found that these conditions do not induce Ag degradation for Ag-coated Au nanoparticles.[173] However, **Figure 6-11** that shows the TEM images of the particles before OsO$_4$ treatment (**Figure 6-11 a**) and after OsO$_4$ treatment (**Figure 6-11 b**) indicates that the silver particles suffer severe decomposition, partially detaching from CoFe$_2$O$_4$.

a)   b)
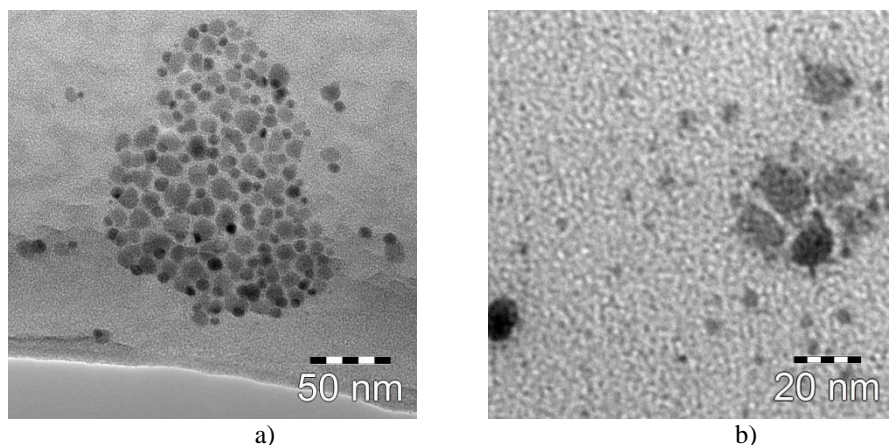
Figure 6-11. TEM images comparing the decay on the number of the Ag@CoFe$_2$O$_4$ particles before (a) and after staining with OsO$_4$ (b).

Treatment with phosphotungstic acid already on stage of blank experiment with pure PAA showed that the amount of stain left on the polymer is not enough to highlight the polymer. The concentration of tungsten was also not enough to perform Electron spectroscopy imaging (ESI) detection. Therefore there was no possibility of a direct visualization of the attachment site of the polymer on the Ag@CoFe$_2$O$_4$ particles.

6.2.1.5.   Formation of emulsions

Each sample of dumbbell-like particles contains a small amount of unfunctionalized CoFe$_2$O$_4$ particles and, if not removed by magnetic separation, free Ag particles. To separate the different types of particles, an experiment involving emulsion formation is performed. Since the reactivity of the thiol group with CoFe$_2$O$_4$ and Ag particles is different, it is planned to attach to the Ag particles a polymer with hydrophilic properties to create an amphiphilic particle. Commercially available PEG-SH (M_w = 5000 g·mol^{-1}) was added to a toluene dispersion containing Ag@CoFe$_2$O$_4$ particles (samples **DLP-70/24h 1:1.8**, **DLP-70/24h 1:1.8 II**, **DLP-70/24h 1:1.8 III**), mixed for 24 h, and the functionalized particles were added to a hexane/water mixture. The choice of the polymer was based on the fact, that polyethylene glycol is soluble in toluene, which makes functionalization of Ag@CoFe$_2$O$_4$ particles in toluene possible. Besides that it is also soluble in water, but not in hexane. So, if

the Ag particles are functionalized with hydrophilic PEG and $CoFe_2O_4$ retains the oleylamine surface groups, amphiphilic particles will be located on the interphase. After vigorous shaking, a stable emulsion has been observed. The emulsion remained stable within several hours. A schematic image of the experiment and the emulsion obtained for sample **DLP-70/24h 1:1.8 II** are presented on **Figure 6-13**. UV-vis and VSM measurements of both organic and water phase were done to estimate the presence of Ag and $CoFe_2O_4$.
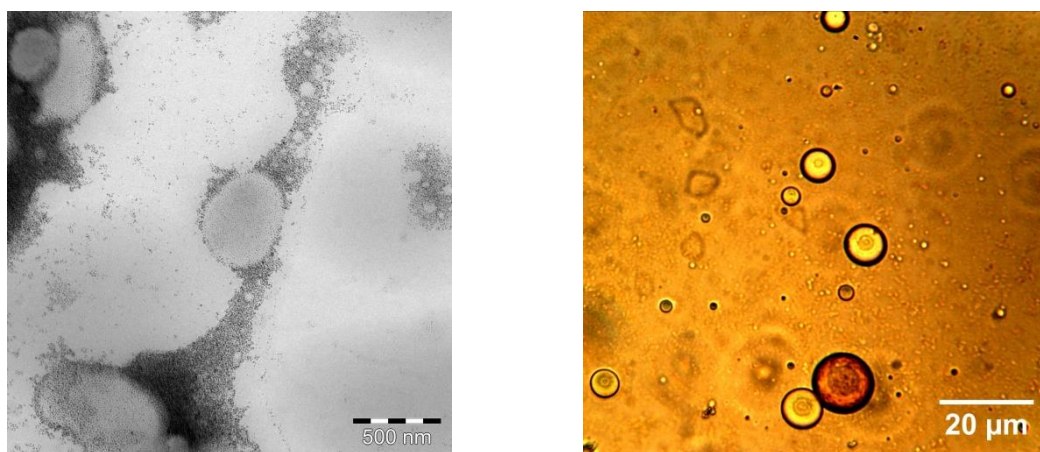
Figure 6-12. TEM and light microscopy images of the emulsions formed with DLP-70/24h 1:1.8 II + PEG.

The UV-spectroscopy shows much lower light absorption peak at 425 nm in the organic phase, when compared to the source $Ag@CoFe_2O_4$ particles. The lower water phase is colored yellow and has a distinctive absorption at 417 nm. The VSM measurement of water phase showed only little magnetic material in the water phase, thus, a conclusion has been made, that water phase consists mostly of free Ag particles. The upper hexane phase showed higher magnetization, than the water phase. Calculating from the magnetization of the source dispersion in toluene and total magnetization of the hexane and water phases, more than 50% of the particles are on the interphase. Taking in account, that about 81% of the particles in sample **DLP-70/24h 1:1.8 II** were decorated with silver, this confirms, that the particles are not decomposing into Ag and $CoFe_2O_4$. The same observations were made for emulsions formed with samples **DLP-70/24h 1:1.8** and **DLP-70/24h 1:1.8 III**. For comparison, the

toluene dispersion of **DLP-70/24h 1:1.8 II** was added to a hexane/water mixture without prefunctionalization with PEG. No stable emulsion was formed, with all the particles remaining in the organic phase. This experiment brings a hint at the asymmetric functionalization of Ag@CoFe$_2$O$_4$ particles with thiolated polymers.
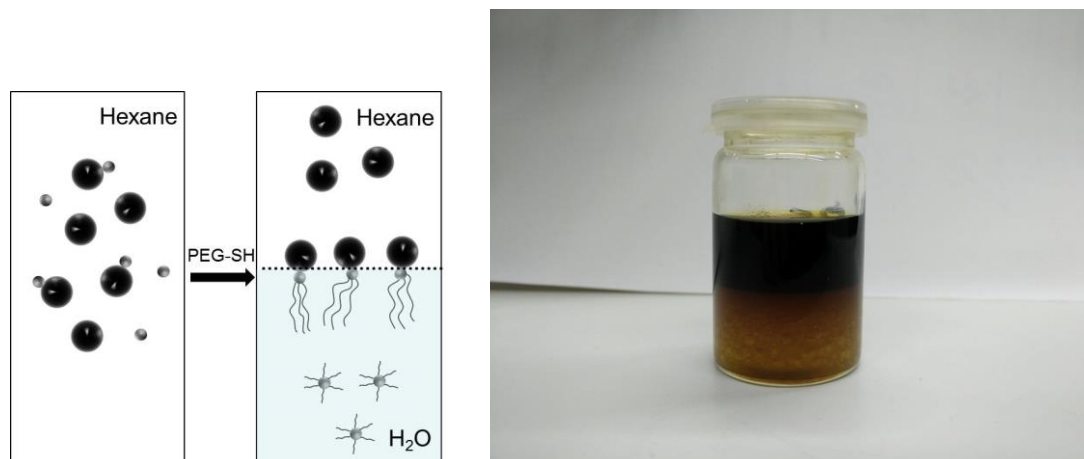
Figure 6-13.Schematic conception of the emulsion formation and the emulsion formed for sample DLP-70/24h 1:1.8 II.
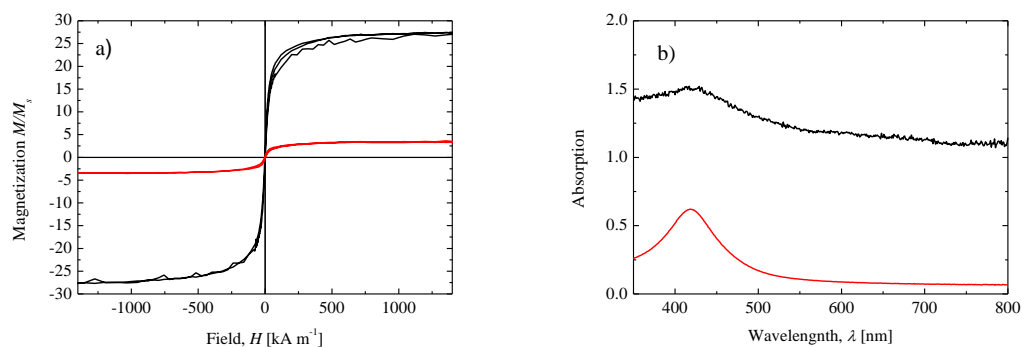
Figure 6-14. Magnetization curves (a) and UV-Vis spectra (b) for hexane phase (black) and water phase (red) of the emulsion made with sample DLP-70/24h 1:1.8 II.

6.3. Transfer of the dumbbell-like particles into aqueous medium

The further application of the particles involves the transfer of the particles into aqueous medium. This is required to be able to adjust the ionization degree of the PAA tails by variation of the pH of the dispersant. The transfer of the particles into the aqueous medium was performed by an exchange of the surface groups, such as oleylamine and oleic acid with polar surface agents. Transfer approaches with citric acid (CA) and with polyacrylic acid (PAA) were tried. Though the approach for pure $CoFe_2O_4$ particles is well described in the literature[76], experiments with citric acid were important for this investigation, since the polymer flagella consist of polyacrylic acid and using a surface group other than PAA would be convenient for further elemental analysis and IR spectroscopy.

A typical transfer experiment starts with washing of the magnetic particles to remove the excess of the surface groups and redispersion in THF. A solution of hydrophilic surface groups (PAA with $M_w = 1800$ g·mol^{-1} or CA) in THF are added, mixed together (since stirring should be avoided, the flask with the sample is placed on a shaker) and heated up to 70°C for 4 h. After that, hexane is added to sediment the particles, the particles are washed with hexane and then with ethanol to remove the excess of the surface agent and the precipitate is finally redispersed in aqueous solution (H_2O) with pH above 7.0.

Functionalization with citric acid proves to be unsuccessful. None of the samples are stable in the aqueous medium. Washing with ethanol causes severe agglomeration and the non-agglomerated particles are washed away during hexane washing. However, transfer with polyacrylic brings positive result. Above 80 % of the particles are dimers. But, as it was found, that only 5 % of the particles can be redispersed after the transfer. This yield is very low, when compared to transfer of the pure $CoFe_2O_4$ particles with yields of about 80 %.
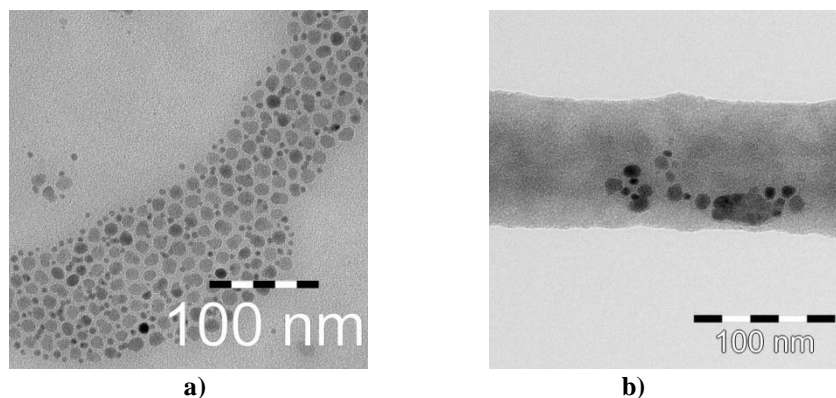
Figure 6-15. TEM images showing: a) Ag@CoFe$_2$O$_4$ (DLP-70/24h 1:1.8 II) in toluene b) Ag@CoFe$_2$O$_4$ in H$_2$O.

Such a low yield is a consequence of the silver agglomeration on the stage of washing with ethanol after the surface group exchange. This assumption is based on the observation of the red-brown precipitate, forming right after the addition of EtOH. Presumably, Ag particles are covered with an amount of PAA, which is insufficient to prevent the agglomeration. More resistant to agglomeration CoFe$_2$O$_4$ particles require less density of the surface groups. To protect the unstable Ag particles, prefunctionalization with thiol-group polymer was tried. Polyethylene glycol with thiol end-group was added into the dispersion of the dumbbell-like particles in toluene before the transfer with calculated ratio of 200 polymer chains per particle. The rest of the procedure remained unchanged. The yield of the transfer of the prefunctionalized particles was 10 %, which is double, compared to particles without prefunctionalization. Even though further elemental analysis and IR-spectroscopy was not possible since the polymer flagella consist of polyacrylic acid and not acid acetic, the batch of particles obtained is suitable for the measurements of hydrodynamic properties, which will be discussed in the next chapter.

6.4. Summary on the synthesis of the asymmetric hybrid particles

The dumbbell-like particles described in **Chapter 5** were successfully functionalized with various polymers, both synthesized in **Chapter 6** and commercially purchased. The amount

of the added polymer was optimized in terms of particles stability. Though no direct visualization of the attachment site was possible because, all the indirect methods point at the formation of the thiol bond exclusively with silver particles. The dumbbell-like particles were transferred into aqueous medium by application of hydrophilic surface groups. Despite the low yields of the transfer, a batch of particles suitable for the measurements of hydrodynamic properties was obtained (**DLP-70/24h 1:1.8 III** with **PAA-SH 10k**). The hydrodynamic properties will be discussed further in **Chapter 7**.

7. Hydrodynamic properties of the asymmetric hybrid particles

In this chapter the hydrodynamic properties of the asymmetric magnetic particles functionalized with polymer tails synthesized in previous chapters are discussed. The aim is to compare the hydrodynamic behavior before and after actuation of the particles by the magnetic field. A change in the diffusion coefficient or observation of the anomalous diffusion would hint at possible propulsion of the particles. The particles functionalized with flagella and actuated by external magnetic fields are compared to the particles without polymer flagella and with particles under no external magnetic fields. The particles are compared both in organic medium, where the polymer chains are expected to be collapsed, and in aqueous medium, where high pH leads to an increase of the stiffness of the flagella.

Information on the diffusion coefficients is obtained using the Dynamic light scattering and information on diffusion coefficients and diffusion behavior is obtained using Light scattering microscopy (LSM). Measurements are performed in both organic and aqueous media. For the measurement of hydrodynamic properties sample **DLP-70/24h 1:1.8 III** functionalized with various polymers are taken. Particles functionalized with poly(ethylene glycol) methyl ether thiol (M_n = 5000 g·mol^{-1}, commercially purchased), poly(tert-butyl acrylate)thiol M_n = 10000 g·mol^{-1} (sample **P(t-BuA)SH 10k**) and polyacrylic acid synthesized by hydrolysis of **P(t-BuA)SH 10k** (sample **PAA-SH 10k**) are ivnestigated. DLS measurements are performed in AC fields of various frequencies, LSM measurements are performed in AC fields as well as in static field. More detailed information on the measurement regimes choice is given in **Chapter 7.2.1**.

7.1. Measurements of the polymer functionalized Ag@CoFe$_2$O$_4$ particles in organic solvents

For measurements in nonpolar solvent samples of particles **DLP-70/24h 1:1.8 III** were functionalized with **P(t-BuA)SH 10k**, **PEG-SH 5k** and **PAA-SH 10k** (the polyacrylic acid was dissolved in acetone, functionalization was performed in mixture of acetone and toluene). The measurements are performed in mixture of toluene/oleylamine (10:1), in which particles remain stable. It is expected, that the polymer chains remain collapsed in nonpolar solvents and do not affect the hydrodynamic properties of the Ag@CoFe$_2$O$_4$ particles.

7.1.1. Dynamic light scattering measurements in organic solvents

DLS measurements were performed with the samples with concentration of 0.1 mg·ml^{-1} in toluene/oleylamine mixture (10:1).

Depolarized dynamic light scattering (DDLS) were performed with a setup including two Glan-Thomson polarizers. For a depolarized light scattering experiment, the incident laser beam has a vertical polarization, whereas the scattered light is detected in horizontal polarization. The vertical-horizontal (vh) geometry was used with the orientation of the polarizer in front of the light scattering detector adjusted to a crossed position with respect to the first polarizer. The decay rate Γ calculated from the autocorrelation function was plotted against the square wave vector q^2 and diffusion coefficients D_t and D_r were read from the slope of the linear fit and from the intercept respectively. The rotational diffusion was calculated from the intercept of the Γ value (see equations (**7-1**) and (**7-4**)).

$$\Gamma_{vv} = D_t q^2 + 6D_r$$

(**7-1**)[174]

$$q = \frac{4\pi n_0}{\lambda} sin\left(\frac{\theta}{2}\right)$$

(**7-2**)

Where n_0 is the refractive index of the solvent, λ is the wavelength of the laser, θ is the detector angle, q is the scattering vector. The hydrodynamic radius r_h is then calculated from the D_t using the Stokes-Einstein equation (**1-9**).

The Γ vs q^2 plots for DLS measurements in nonpolar solvents are shown on **Figure 7-1**. The intercept of the decay rate Γ is slightly distinct from zero for the samples. This might be a consequence of an anisotropic shape of the particles.
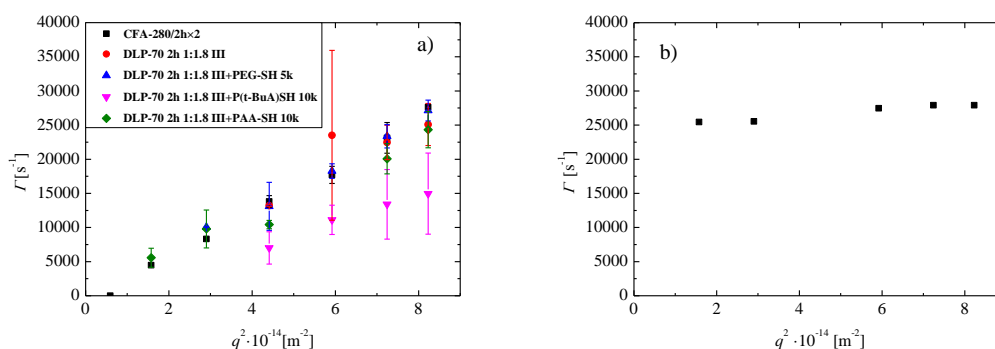
Figure 7-1. a): DLS measurements of sample DLP-70/24h 1:1.8 III functionalized with various polymers; b): DDLS measurements of sample DLP-70/24h 1:1.8 III functionalized with PAA-SH 10K.

Table 7-1. Results obtained from the DLS measurements of the samples measured in toluene.

Sample	D_t [$10^{12} \cdot m^2 \cdot s^{-1}$]
CFA-280/2h×2	36.3±0.7
DLP-70/24h 1:1.8 III	32.0±2.0
DLP-70/24h 1:1.8 III PEG	30.2±1.3
DLP-70/24h 1:1.8 III P(t-BuA)SH	20.7±2.0
DLP-70/24h 1:1.8 III PAA-SH	27.2±3.0

The data obtained from the measurements is collected in **Table 7-1**. The diffusion coefficient for the primary $CoFe_2O_4$ particles, $Ag@CoFe_2O_4$ particles and $Ag@CoFe_2O_4$ particles functionalized with PEG-SH and PAA-SH does not change significantly. In case of P(t-BuA)SH, the diffusion coefficient drops by 30 %.

The samples functionalized with polyacrylic acid can be measured with DDLS. **Sample DLP-70/24h 1:1.8 III** has a D_r in range of 4000-4500 s^{-1}. According to the Tirrado/Torre model for a cylinder-like object, these values correspond to a rod with a length of 120 nm and

diameter of 50 nm.[175] The translational diffusion coefficient is however much lower ($4.3 \cdot 10^{-12}$ compared to $27.2 \cdot 10^{-12}$), than observed in non-polarized measurement. This might indicate, that the only objects observed in a DDLS measurement are the agglomerates, and after the filtration no fluctuations of the scattering is observed.

7.1.2. Light scattering microscopy measurements in organic solvents

The goal of the Light scattering microscopy measurements is to estimate the diffusion behavior of the particles and to compare it to DLS measurements. Unlike DLS, LSM visualizes the diffusion of the particles, making it possible to calculate the mean squared displacement (*MSD*) over time. Diffusion processes of the investigated particles might not follow the Gaussian statistics and the dependence of the *MSD* against time is no longer linear. Instead, the equation for anomalous diffusion is used to describe such processes (equation (**7-3**)).

$$MSD \sim D \cdot t^{\alpha}$$

(**7-3**)

Where *D* is the diffusion coefficient, *t* is the time, *α* is the anomalous diffusion exponent.[176] The anomalous diffusion exponent defines the diffusion behavior: for $0 < \alpha < 1$ the process is parametrized as sub-diffusion, while $1 < \alpha < 2$ corresponds to superdiffusion. In case of the Brownian motion $\alpha = 1$. Another special case is for $\alpha = 2$, which is called ballistic motion.

The LSM measurements in static magnetic field were performed at field strength of 13 mT, where 35 % of the particles are aligned along the magnetic field, according to VSM measurements, measurements in alternating magnetic field were performed at 1.2 mT with 100 Hz frequency where 5 % of the particles are aligned along the magnetic field. Measurements were done in solvents with different viscosities. Hexane has the lowest

viscosity (0.294 mPa·s), but it has a refractive index (n_0) of 1.375, what differs from the RI of cobalt ferrite nanoparticles ($\approx$ 1.5). More viscous tetralin has n_0 of 1.54 making detection of smaller particles much more difficult. Sample with with PEG was also measured in ethanol and tetralin.

The results of the measurements are shown in **Figure 7-1**. The α values and diffusion coefficients are calculated for all samples. The α values of all samples are about 1.0. That is a sign of pure diffusive motion of the particles. The diffusion coefficients measured by LSM are lower, than observed in DLS measurements. Corrected by the viscosity factor the hydrodynamic diameter of the particles observed by LSM is almost twice as large as observed by DLS.

Table 7-2. Results obtained from LSM measurements.

Sample name	α	D_t [$10^{12} \cdot m^2 \cdot s^{-1}$]
DLP-70/24h 1:1.8 III hexane	0.99±0.28	23.8±4.1
DLP-70/24h 1:1.8 III DC hexane	1.02±0.24	20.3±9.0
DLP-70/24h 1:1.8 III AC hexane	0.97±0.26	16.1±5.3
DLP-70/24h 1:1.8 III PEG hexane	0.99±0.24	20.2±10.3
DLP-70/24h 1:1.8 III PEG DC hexane	1.03±0.26	14.2±4.7
DLP-70/24h 1:1.8 III PEG AC hexane	1.01±0.25	14.2±4.7
DLP-70/24h 1:1.8 III PEG EtOH	1.00±0.26	3.9±1.1
DLP-70/24h 1:1.8 III PEG EtOH DC	1.00±0.28	3.8±1.1
DLP-70/24h 1:1.8 III PEG EtOH AC	0.98±0.25	3.9±1.2
DLP-70/24h 1:1.8 III PEG Tetralin	0.89±0.24	3.1±1.1
DLP-70/24h 1:1.8 III PEG Tetralin DC	0.95±0.26	2.6±1.1
DLP-70/24h 1:1.8 III PEG Tetralin AC	0.82±0.05	3.3±1.4

7.2. pH-dependent measurements of the polymer functionalized Ag@CoFe$_2$O$_4$ particles in aqueous solvents

To estimate the impact of the polyacrylic acid attached to the Ag@CoFe2O4 particles on its hydrodynamic properties, radius of gyration (R_g) and Gaussian chain length (L_g) were calculated. According to Cranford and Buehler[159], the ionization degree of polyacrylic acid

is dependent on the pH of the solution the way presented on **Figure 8 14**. At pH ≥ 8 the ionization degree of PAA is 100 %.
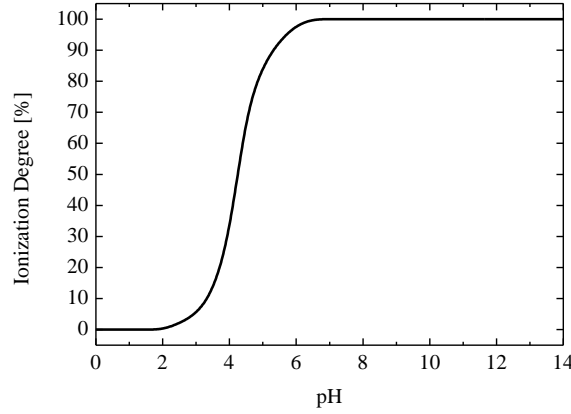
Figure 7-2. Polyelectrolyte persistence length as a function of pH for polyacrylic acid and polyallylamine hydrochloride (reproduced from[159], Fig. 11).

On the other hand, the persistence length (l_p) of polyacrylic acid at 100% ionization degree was estimated to be 12.6Å[119], thus the Kuhn length (l_k) is 25.2 Å. The contour length (R_{max}) for a polymer chain is calculated as

$$R_{max} = N_{CC} \cdot a_{CC} \cdot l_{CC} \cdot \cos\left(\frac{\theta_{CC}}{2}\right) \qquad \textbf{(7-4)}^{[177]}$$

Where N_{CC} is the number of monomer units, a_{CC} is the number of C-C bonds in the monomer unit, l_{CC} is the length of the C-C bond (1.54Å), θ_{CC} is the tetrahedral angle = 109°.[116] For polymer with 70 monomer units, R_{max} = 12.5 nm. The number of Kuhn monomers (N_b) is calculated as

$$N_b = \frac{R_{max}}{l_k} \qquad \textbf{(7-5)}^{[177]}$$

Then radii of gyration of an ideal linear chain (R_{gl}) and of a rod polymer (R_{gr}) are calculated as

$$R_{gl}^2 = \frac{N_b \cdot l_k^2}{6} \qquad\qquad \textbf{(7-6)}^{[177]}$$

$$R_{gr}^2 = \frac{N_b^2 \cdot l_k^2}{12} \qquad\qquad \textbf{(7-7)}^{[177]}$$

For a polymer with 70 monomer units R_{gl} = 2.30 nm and R_{gr} = 3.61 nm. Given the fact, that hydrodynamic radius is of the same order as radius of gyration,(r_h/R_{gr} = 0.64 for good solvent)[178] the hydrodynamic diameter of the Ag@CoFe$_2$O$_4$ particles is not expected change not above 20 % after functionalization with polyacrylic acid. One should take into account, that since the polymer chains are packed rather dense on the surface of the Ag particles and the distance between the polymer chains is lower, than the length of the chain, interactions between the polymer chains may take place leading to a deviation of the persistence length value from the literature value.

Using the polyacrylic acid (M_w = 1800 g·mol^{-1}) the Ag@CoFe$_2$O$_4$ are transferred into aqueous medium. The yield of the transferring method is low (less, than 10 % of the particles are redispersable). The particles in the aqueous dispersions are functionalized with thiol-modified polyacrylic acid (**PAA-SH 10k**) based on the calculation of 200 chains per a particle. The samples were washed magnetically to remove the excess of the polymer.

7.2.1. Dynamic light scattering measurements in aqueous solvents

The samples in aqueous solutions were measured with DLS and DDLS. The DLS measurements were performed with no external magnetic field as well as in the alternating magnetic field (1.2 mT with frequency of 1000 Hz (5% of the particles are aligned) and 10 mT (30% of the particles are aligned) with frequency of 100 Hz). An important optimization of the conditions was changing the temperature of the measurement cell from 298 K to

284.15 K. This was done to increase the viscosity (from 0.89 Pa·s to 1.26 Pa·s)[179] and slower both the translational and rotational diffusion. Using the 0.1 μm filter has also significantly facilitated the analysis.

The calculation of the parameter characterizing the propulsion properties from the equations (**1-1**), (**1-2**) and (**1-3**) of the particles has revealed the following. For the particles in H_2O at 10 °C the sperm number $S_p = 0.15$. This is lower, than is necessary for effective propulsion, however one should remember, that the model is designed for a single tail on the particle, whereas the investigated particles have about 200 chains per a particle. The parameter β denoting the effectiveness of the magnetic bead is as high as 3000 for an external alternating magnetic field of 100 Hz and 10 mT. This is even higher, than required. For AC field of 1 mT, 1000 Hz β is 30, which is still high enough for an effective actuation. The propulsion force F_0 is in range between 10^{-21} N and 10^{-23} N and Péclet number for propulsion (Pe_{trans}), calculated as $Pe_{trans} = F_0/k_B \cdot T$ is in range from 0.3 to 0.003, which is low, but again, the model is designed for a single polymer tail. To compare the magnetic torque with rotational diffusion another Péclet number is introduced $Pe_{rot} = m \cdot B/k_B \cdot T$. For AC field with field strength of 10 mT, $Pe_{rot} = 0.2$. This order shows, that thermal fluctuations will compete with the torque. Decreasing the field strength to 1 mT will decrease Pe_{rot} to 0.02.

The DLS measurements show high diffusion coefficients values fluctuation for small angles, caused by backscatter and scatter from larger objects, such as dust. The diffusion coefficients are calculated from the measurements at 130° as giving the best intensity. The results of the measurements are gathered in **Table 7-3**. The hydrodynamic diameter of the samples, functionalized with polyacrylic acid lies in the same range as the samples without the polymer. DDLS measurements proved to be inefficient. Low shape anisotropy of the sample causes almost no fluctuation of the intensity.

The DLS measurements show strong fluctuation of the diffusion coefficient value in the whole pH range for all samples. A certain tendency is being observed for the samples measured under external AC field at 100 Hz, 10 mT. The diffusion coefficients of the $Ag@CoFe_2O_4$ particles without polymer flagella do not change significantly with rising pH (see
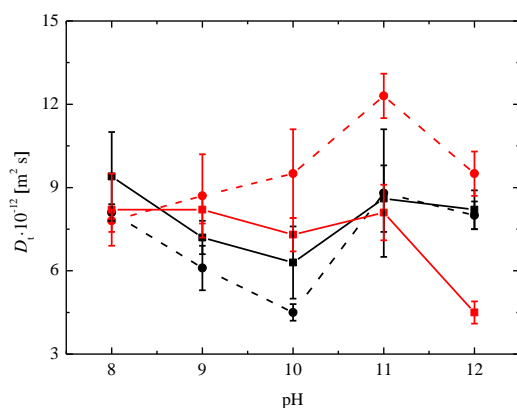
Figure 7-3). The diffusion coefficients of the $Ag@CoFe_2O_4$ particles functionalized with **PAA-SH 10k** show a strong fluctuation with rising pH as well. When the external alternating magnetic field is applied, the particles functionalized with polymeric tail show higher diffusion coefficients than the particles of the same species without polymeric tail. A similar tendency is observed for the measurements at 110°. The fact, that $Ag@CoFe_2O_4$ particles without polymer functionalization do not show any change of the diffusion proves that no thermophoresis due to possible heating of the measurement cell by the Helmholtz coil is being observed. On **Figure 7-4** the distribution of the diffusion coefficients for measurements at pH 11.0 are shown. All distributions show lognormal behavior with no sign of changing the distribution character.

Table 7-3. Apparent diffusion coefficients obtained from the DLS measurements of samples DLP-70 24h 1:1.8 II and DLP-70 24h 1:1.8 II + PAA 10k at different pH values; measured at 130°.

Sample name	Diffusion coefficient D_t [$10^{12} \cdot m^2 \cdot s^{-1}$]
	pH

		8.0	9.0	10.0	11.0	12.0
DLP-70/24h 1:1.8 III	No field	9.4±1.6	7.2±0.6	6.3±1.3	8.6±1.2	8.2±0.7
	AC field 100Hz, 10 mT	8.1±0.3	6.1±0.8	4.5±0.3	8.8±2.3	8.0±0.5
	AC field 1000Hz, 1.2 mT	9.2±0.4	6.7±0.7	1.9±0.2	8.1±0.6	10.0±0.3
DLP-70 24h 1:1.8 III + PAA-SH 10k	No field	8.2±1.3	8.2±0.5	7.3±0.6	8.1±1.0	4.5±0.4
	AC field 100Hz, 10 mT	7.8±0.4	8.7±1.5	9.5±1.6	12.3±0.8	9.5±0.8
	AC field 1000Hz, 1.2 mT	8.0±1.5	7.8±2.1	6.9±0.9	8.1±1.6	3.8±0.3
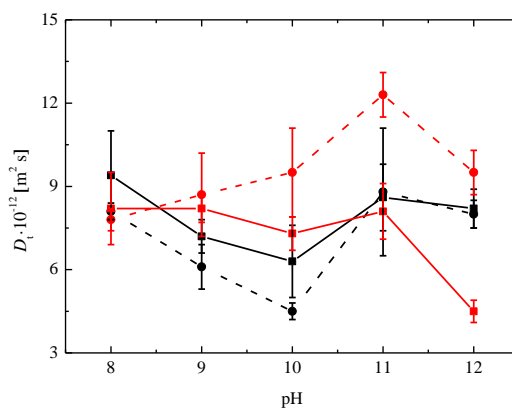
Figure 7-3. Diffusion coefficients depending on the pH value of the solutions for sample DLP-70/24h 1:1.8 III (black) and sample DLP-70/24h 1:1.8 III + PAA-SH 10 k (red); measured with no magnetic field applied (solid line) and in alternating magnetic field (10 mT, 100 Hz; dashed line).
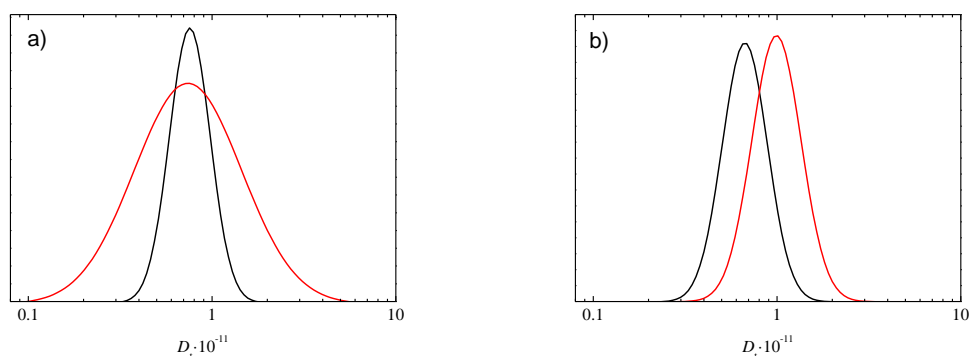
Figure 7-4. Diffusion coefficient distributions from the DLS measurements, a): sample DLP-70/24h 1:1.8 III (pH 11, no magnetic field (black), AC field, 100Hz, 10mT (red)); b): sample DLP-70/24h 1:1.8 III + PAA-SH 10 k (pH 11, no magnetic field (black), AC field, 100Hz, 10mT (red)). Measured at 130°.

7.2.2.   Light scattering microscopy measurements in aqueous solvents

The Light scattering microscopy measurements were done for samples in aqueous solutions at different pH values. Since the particles tend to degrade even in the weak acidic solutions, only solutions with pH ≥ 8 were performed. The solutions with different pH were prepared by taking a commercially purchased 0.1M NaOH solution and diluting it with Millipore water. The pH of the solutions was controlled by a pH-meter. All the measurements were

performed at room temperature. The measured solutions were injected into the measurement cell through a 0.1 μm filter. Measurements in the magnetic field were performed under the same conditions as stated above.

The results of the measurements are shown on **Figure 7-5** and gathered in **Table 7-4**. The anomalous diffusion exponents for all samples are above 1.0 for pH ≥8.0. Though volume drift of the sample in the cell is monitored and the samples are measured after the dispersion comes to an equilibrium inside the cell, the α values are unexpectedly high and do not follow any explainable trend.

Table 7-4. Anomalous diffusion exponents at different pH.

Sample Name	α					
	pH 8.0	pH 9.0	pH 10.0	pH 11.0	pH 12.0	pH 13.0
DLP-70/24h 1:1.8 III	1.18±0.26	1.15±0.27	1.18±0.24	1.16±0.25	1.17±0.26	1.15±0.28
DLP-70/24h 1:1.8 III DC	1.14±0.24	1.08±0.22	1.28±0.28	1.10±0.25	1.16±0.25	1.17±0.26
DLP-70/24h 1:1.8 III AC	1.16±0.24	1.13±0.26	1.21±0.27	1.17±0.29	1.18±0.25	1.17±0.25
DLP-70/24h 1:1.8 III PAA	1.12±0.24	1.25±0.16	1.22±0.21	1.25±0.20	1.16±0.26	1.19±0.27
DLP-70/24h 1:1.8 III PAA DC	1.23±0.21	1.27±0.18	1.28±0.11	1.29±0.21	1.16±0.26	1.15±0.02
DLP-70/24h 1:1.8 III PAA AC	1.20±0.21	1.30±0.20	1.27±0.16	1.28±0.24	1.17±0.25	1.17±0.25

For the comparison of the pH-dependent measurements the values of the apparent diffusion coefficients are taken (see **Table 7-5** and **Figure 7-5**). The values are generally lower, than observed in the DLS measurements (when adjusted by factor of temperature). A certain trend can be observed consisting in an almost constant hydrodynamic diameter for samples functionalized with PAA in pH range from 8.0 to 13.0. The samples without PAA flagella show on the contrary a decrease of the diffusion coefficient from pH 8.0 to pH 11.0 and are higher in this pH range than the values of the functionalized particles.

The influence of the magnetic field seems to have similar effects on the unfunctionalized and functionalized samples. Both sample species show a decrease of the diffusion coefficient, when static magnetic field is applied.

Such results come in a certain disagreement with the published information on the behavior of the polyacrylic acid in the solutions with different pH. According to Adamczyk[180] and Buehler[119], polyacrylic acid reaches 100% ionization already at pH of 8.0 (see Figure 7-2). At this point the persistence length of approximately 10-13 Å is reached. The LSM measurements show, that the hydrodynamic diameter doesn't grow between the pH 9.0 and pH 13.0.

Table 7-5. Results from the LSM measurements of aqueous samples at different pH.

Sample Name	Diffusion coefficient D_t [$10^{12} \cdot m^2 \cdot s^{-1}$]					
	pH 8.0	pH 9.0	pH 10.0	pH 11.0	pH 12.0	pH 13.0
DLP-70/24h 1:1.8 III	10.1±3.6	9.5±3.8	6.9±2.4	5.6±2.4	7.1±2.3	7.1±3.6
DLP-70/24h 1:1.8 III DC	8.1±2.9	7.9±2.6	6.7±2.7	5.9±2.8	7.3±2.6	5.1±1.7
DLP-70/24h 1:1.8 III AC	8.0±2.7	9.5±3.3	7.8±3.7	5.7±2.0	6.4±2.2	7.0±2.9
DLP-70/24h 1:1.8 III PAA	6.9±1.8	6.7±1.5	6.4±2.1	6.4±2.2	6.4±2.5	6.7±2.5
DLP-70/24h 1:1.8 III PAA DC	6.5±1.8	6.0±2.0	6.3±2.0	5.7±1.9	6.8±2.8	6.5±2.1
DLP-70/24h 1:1.8 III PAA AC	7.1±1.4	6.8±2.0	6.3±1.4	6.1±1.8	7.1±3.6	6.8±2.3
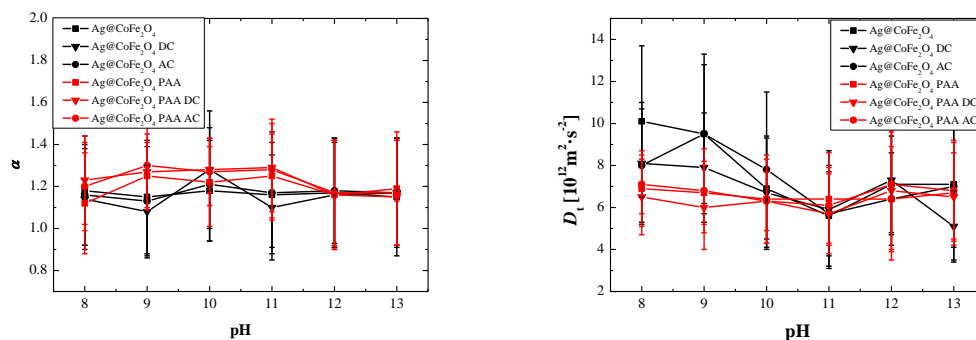
Figure 7-5. Diffusion coefficients and *α* measured at different pH for particles without polymer (black) and with polymer (red).

A measurement in more viscous solvent was performed. As a solvent a mixture of glycerol with 0.1M NaOH (3:1) was taken. Its viscosity is 3.5 cPa·s and is much higher, than of the water. **Figure 7-6** shows that anomalous diffusion exponent remains at 1 for both functionalized and unfunctionalized particles also in external magnetic field. This is comparable to what is observed for samples in organic media.
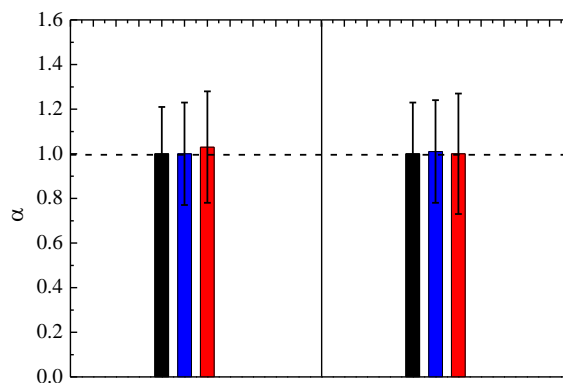
Figure 7-6. Anomalous diffusion exponent for unfunctionalized (left)and functionalized (right) particles in glycerol without magnetic field (black), with external static field (blue) and alternating magnetic field (red).

7.3. Summary on the hydrodynamic properties of the asymmetric magnetic particles functionalized with polymer flagella

Summarizing the results from DLS and LSM measurements, it is possible to say, that the particles show slight change in the hydrodynamic properties when being functionalized asymmetrically with polyacrylic acid. The application of the magnetic field is found to have an effect on the particles with polyacrylic acid in aqueous solutions. These particles show a deviation of diffusion coefficients when an alternating magnetic field is applied. The measurement error is relatively high and hinders the interpretation of this possible effect. Basing on these observations it is hard to state, if particles possess the ability to move in any manner other than the Brownian diffusion. Overcoming the Brownian diffusion is expected to be characterized by a more certain change of the anomalous diffusion exponent in presence of the magnetic field. In order to make a conclusion, more precise data and lower measurement errors are required.

8. Summary and outlook

In this work, asymmetric nanoscale objects consisting of a magnetic core and soft polymer flagella have been successfully synthesized. The hydrodynamic properties of these objects in various solvents under actuation by an external magnetic field have been investigated.

Several synthetic approaches for the synthesis of the magnetic $CoFe_2O_4$ particles were carried out, the influence of the reaction parameters were investigated and the reaction conditions were optimized. The synthetic approach exploiting metals oleate complexes thermal decomposition[55] results in well-dispersed particles in a size range between 15 and 25 nm. It is shown, that the shape and the size of the particles are influenced by the reaction temperature. The synthesis at lower temperatures is found to lead to formation of crystal phases different from cobalt ferrite having smaller saturation magnetization. The synthetic approach including thermal decomposition of iron acetylacetonate and cobalt acetylacetonate complexes[66] with repeated growth iterations results in well-dispersed particles in a size range between 10 and 15 nm after several growth iterations. These particles show a high agglomeration resistance and high saturation magnetization of up to 90 % of the bulk saturation magnetization value.[128] The lower reaction temperature is found to lead to narrower size distribution and longer reaction time leads to faster growth of the $CoFe_2O_4$ particles.

The obtained $CoFe_2O_4$ particles have been used for synthesis of dumbbell-like $Ag@CoFe_2O_4$ particles. Two different synthetic approaches have been tried and optimized towards almost uniform particles ensemble. The reduction of silver salt in tetralin in presence of $CoFe_2O_4$ particles[92] leads to the formation of dumbbell-like structures. The content of the $CoFe_2O_4$ functionalized with Ag counterpart is found to be low, not exceeding 60 %. The second synthetic approach is based on the reduction of silver salt in toluene with oleylamine in

presence of $CoFe_2O_4$ particles. The particles synthesized this way show a high content of the dumbbell-like particles (> 80 %) and are stable over time against disassembly and agglomeration. Various possible mechanisms for the formation and growth have been suggested and discussed. The physical properties of the $Ag@CoFe_2O_4$ dumbbell-like particles, such as magnetism and surface plasmon resonance have been investigated.

The poly(tert-butylacrylate) polymers for functionalization of the dumbbell-like $Ag@CoFe_2O_4$ particles have been synthesized in an atom-transfer radical polymerization and functionalized with thiol group with further hydrolysis to polyacrylic acid. The attachment of the synthesized polymers over thiol group to the Ag surface of $Ag@CoFe_2O_4$ particles has been performed and investigated. Numerous indirect instrumentation methods, such as UV-vis and IR spectroscopies, as well as elemental analysis along with experiments on formation of emulsions indicate the successful selective attachment of the polymer to the Ag part.

The hydrodynamic properties of the $Ag@CoFe_2O_4$ particles functionalized with various polymers have been investigated by light scattering methods, such as DLS and LSM, in organic and aqueous dispersants. The results of the measurements in organic dispersants show no difference in the diffusion behavior of the particles before and after an external alternating magnetic field is applied. The DLS measurements in H_2O reveal an increase of the diffusion coefficients for the $Ag@CoFe_2O_4$ particles functionalized with polyacrylic acid after application of the external alternating magnetic field with the frequency of 100 Hz and field strength of 10 mT. This effect is not observed for $Ag@CoFe_2O_4$ particles without attached polyacrylic acid. Furthermore, with increasing pH of the solution the effect of increasing diffusion coefficient is getting larger for the $Ag@CoFe_2O_4$ particles functionalized with polyacrylic acid. These results couldn't be supported by the results from the LSM measurements, in which no change in the diffusion behavior is observed upon application of the external alternating magnetic field.

For further experiments the following can be suggested. Since the light scattering measurements were performed on the detection limits of the instrumentation techniques, modification of the measured objects should be made to facilitate the measurements. The increase of the size of the objects would increase the intensity of the scattered light and enhance the results of the measuring techniques exploiting the scattered light. Another improvement would be using the particles, which do not show any plasmon resonance in range of 400-420 nm. This would make application of lasers with shorter wavelength and higher intensity possible. Otherwise, a strong decrease in the intensity of scattered light for the lasers with such wavelength is observed. Moreover, strong light absorption is expected to cause a local overheating around the Ag part changing the environmental conditions around the particle. Yet, if another type of propulsion, such as self-thermophoresis, which has already been described for microparticles[16–19,181], will be investigated, the dumbbell-like particles are already suitable for light scattering measurements involving the lasers with shorter wavelength, including the frequent 488 nm laser for DLS. Another important aspect of the measurements is the variation of alternating magnetic field strength and frequency. As can be seen from the calculations in **Chapter 7.2.1** increasing the frequency would increase the S_p parameter. However, an increase of the magnetic field strength B is also necessary to keep the β parameter high enough to maintain the effectiveness of the magnetic bead. To enable this, a new instrumentation setup with magnetic coils capable to produce stronger magnetic fields is required. The purported value of the magnetic field strength is 0.02 T or higher at frequency of 10^5 Hz. A proper cooling of the coil is to be taken care of. The viscosity of the dispersant is another parameter, which is essential for suppression of the strong Brownian motion, but also influencing the value of β parameter. Higher viscosity demands higher magnetic field strength. Lower temperature decreases the tail's bending modulus, leading to a higher sperm number and increases the solvent viscosity. The increase of the size of the particles and of the length of the polymer flagella along with corresponding

increase of the rigidity of the polymer tail (such as DNA strains with persistence length of about 50 nm) can be applied for higher aspect ratio of the particles, thus enabling the DDLS measurements and to break the symmetry according to the "scallop theorem",[14] leading to a more distinct ballistic movement of the particles.

9. Experimental Part

9.1. Chemicals

Table 9-1. The list of used chemicals.

Chemical	Manufacturer	Purity
1,2,3,4-tetrahydronaphthalene	Merck	98 %
0.1 M sodium hydroxide	Grüssing	99 %
acetone	VWR	techn.
acetic acid (glacial)	VWR	techn.
aluminum oxide, basic	Acros Organic	98 %
aluminum oxide, neutral	Sigma-Aldrich	98 %
chloroform	Fisher Scientific	99.8 %
chloroform D	Euriso-Top	99.8 %
cobalt (II) acetylacetonate	Sigma Aldrich	97 %
cobalt (II) chloride hexahydrate	ABCR GmbH & Co. KG	97 %
copper (I) bromide	Sigma-Aldrich	98 %
dibenzyl ether	ABCR GmbH & Co. KG	98 %
dichloromethane	VWR	techn.
dimethyl formamide, extra dry	Acros Organics	99.8 %
ethanol	VWR	techn.
ethanol (absolute)	Fisher Scientific	HPLC
iron (III) acetylacetonate	ABCR GmbH & Co. KG	99 %
iron (III) chloride hexahydrate	Sigma-Aldrich	97 %
methanol	VWR	techn.
methyl-2-bromopropionate	Sigma-Aldrich	97 %
n-butyl acrylate	Sigma-Aldrich	99 %
n-hexane	VWR	techn.
octadecene-1	Aldrich	90 %
oleic acid	Fisher Scientific	70 %
oleic alcohol	ABCR GmbH & Co. KG	85 %
oleylamine	Acros Organics	80 - 90 %
osmium tetroxide	Sigma Aldrich	99.8 %
PMDETA	Sigma Aldrich	99 %
polyacrylic acid $M_w = 1800$ g·mol^{-1}	Sigma Aldrich	
silver acetate, anhydrous	Alfa Aesar	99 %
silver nitrate	Applichem	99 %
sodium hydroxide	Fisher Chemical	99.2 %
sodium oleate	Fluka	98 %
sulfuric acid	VWR	95%
tetrahydrofuran	various	techn.
tert-butyl acrylate	Sigma-Aldrich	98 %
PEG-SH, $M_w = 5000$ g·mol^{-1}	Aldrich	98 %
thiourea	Acros Organics	99 %
toluene	Fisher Scientific UK	99.9 %
trifluoroacetic acid	Solvay Organics	99 %
water	Acros Organics	99.9 %
deuterium oxide	Euriso-Top	99.9 %

The listed chemicals were used without further purification, if not stated otherwise.

9.2. Analytic methods

Magnetization curves are monitored at room temperature with an ADE Magnetics Vibrating Sample Magnetometer EV7 up to maximum field strength of 2.2 T. A typical experiment consists of a virgin curve, followed by a full hysteresis loop. Samples are measured in sealed Teflon vessels, placed on a glass sample holder between two poles of an electromagnet, and vibrated at a frequency of 70 Hz.

Dynamic light scattering (DLS) measurements are performed on a High-Performance Particle Sizer HPP5002 (Malvern Instruments) at 20 °C, using glass cuvettes. The particle size distribution is derived from a deconvolution of the measured intensity autocorrelation function by the non-negative least-squares algorithm included in the DTS software. The DLS measurements in aqueous solvents are performed using ALV Autocorrelator with 22 mW He/Ne Laser (λ=633 nm) and Glan Thompson prism for DDLS. All samples are filtered five times before measurement (0.45 µm PTFE).

Elemental analyses (EA) are carried out on a Perkin-Elmer Analyzer 2400 (in Düsseldorf) and on an Elementar Vario EL (Elementar) in Cologne. Samples for more precise elemental analysis are sent to Mikrolab Kolbe in Mülheim.

Transition Electron Microscopy (TEM) images are performed on samples prepared via dropcasting on a carbon-coated copper grid by using a LEO 912 Omega, Oberkochen, Germany.

Attenuated total reflection infrared (ATR-FTIR) spectra are measured on a Nicolet FT-IR-5SXB spectrometer equipped with a Specac Golden Gate Heated Diamond ATR Top Plate (in Düsseldorf) and on IR Affinity-1 acquired form Shimadzu Company (in Cologne).

The NMR spectra of samples are measured on NMR Bruker® AV 300 [300 MHz] spectrometer at room temperature with TMS as a reference.

AC-susceptometry measurements are performed using DynoMag (Hardware version B) instrument purchased from Firma Imego in frequency range of 1 Hz – 250000 Hz and field strength up to $0.4 \text{ kA} \cdot \text{m}^{-1}$.

The XRD measurements are performed on a Stoe Stadi instrument. Monochromatic Mo $K\alpha$ radiation with a wavelength of $\lambda = 0.7093$ Å is used in the range of $2\theta = 0 - 80°$.

GPC measurement are done using sampler (Sykam S5250), with pump (Flow Intelligent Pump AI-12), degasser (Flow Gastorr AG-32) and a column (MZ Analysentechnik, MZ-Gel SD plus). Samples are solved in THF (HPLC Grad). An UV-Detector (Sykam S3245) and an RI-detector (Schambeck SFD RI2012A) are used.

Mossbauer spectroscopy is performed in the University Duisburg Essen in the working group of Prof. Dr. H. Wende. A 30 mCi ^{57}Co source mounted on a WissEl MVT-1000 high-velocity Mossbauer driving unit with a maximum velocity of $\sim 1000 \text{ mm} \cdot \text{s}^{-1}$ in constant acceleration mode is used. In the low velocity regime ($< 12 \text{ mm} \cdot \text{s}^{-1}$), a 20 μm α-Fe foil is used as calibration standard, while a WissEl MVC-450 laser interferometer is used for calibration at higher velocities.

Light scattering microscopy measurements are performed with LM-10 dark field scattering microscope, equipped with Helmholtz coils. Measurements are evaluated using NTA 2.3 and NTA 3.0 Software.

9.3. Synthetic procedures

9.3.1. Synthesis of CoFe$_2$O$_4$ particles

The synthesis of CoFe$_2$O$_4$ particles from mixture of iron and cobalt oleate complexes consists of two steps. First step is the synthesis of mixture of cobalt and iron oleate complexes. In a typical synthesis, 4 mmol of FeCl$_3$·6H$_2$O, 2 mmol of CoCl$_2$·6H$_2$O, 16 mmol of sodium oleate (C$_{18}$H$_{33}$O$_2$Na), 10 ml of H$_2$O, 10 ml of ethanol and 20 ml of hexane were mixed in a

Schlenck tube and refluxed at 60°C for 4 h. The mixture of oleate complexes was obtained by separation of the water phase and subsequent evaporation of the residual ethanol and hexane at 70^0 C and water at 110^0 C.

Second step is thermal decomposition of mixed oleate complexes. Mixed oleate complexes, obtained in first step, 20 ml 1-octadecene and 0.54 ml of oleic acid were mixed and stirred magnetically for 1 h. under flowing nitrogen. The mixture then was heated to the target temperature with a heating rate of 1°C/min and was held at this temperature for 60 min under flowing nitrogen with continuous stirring. System was refluxed all the time. Temperature control was performed using J-KEM digital temperature controller. Sample CFO-320 was synthesized in a tube oven, samples CFO-315 and 310 were synthesized using a heating mantle (**Figure 9-1**).
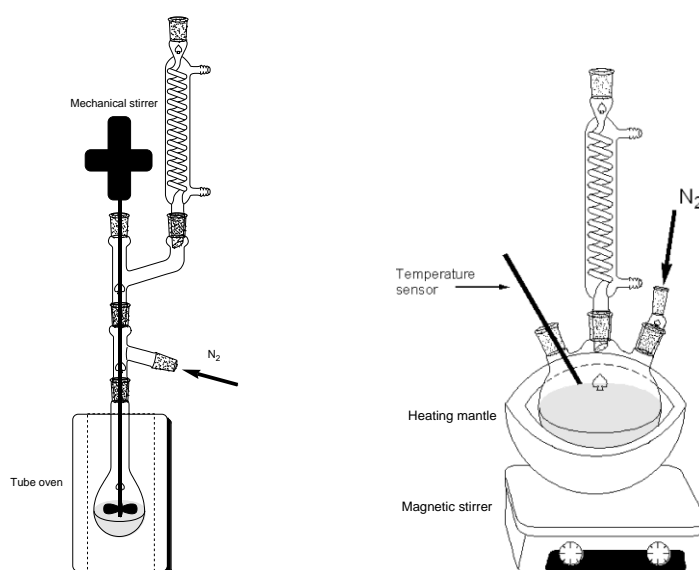
Figure 9-1. Scheme of the synthetic equipment using tube oven (left) and heating mantle (right) for the synthetic approach with oleate complex

The theoretical yield for $CoFe_2O_4$ is 2.28% of mass. Theoretical concentration of magnetic material in the raw solution is 23 mg·ml^{-1}. The particles dispersion in 1-octadecene was mixed with ethanol (1:3) and centrifuged at 6000 rpm for 15 minutes. The supernatant was discarded and the precipitate redispersed in hexane.

The second method is based on the thermal decomposition of the acetylacetonate mixed-metal complex[66] and includes the synthesis of the seed particles with their further growth. In a typical synthesis of the seed particles 2 mmol of $Fe(acac)_3$, 1mmol of $Co(acac)_2$, 6 mmol of oleic acid, 6 mmol of oleylamine 6 mmol, and 20 ml of phenyl ether are mixed and magnetically stirred under a flow of nitrogen. The mixture is heated to 200°C for 120 min and then, under a blanket of nitrogen, heated to reflux (300 °C) for another 120 min. The black-brown mixture was cooled to room temperature by removing the heat source. Under ambient conditions, ethanol (60 ml) was added to the mixture, and a black material was precipitated and separated via centrifugation. The black precipitate was redispersed in toluene/oleylamine mixture (10:1). The further growth approach consists in following. To preliminary synthesized particles in toluene $Fe(acac)_3$ (2 mmol), $Co(acac)_2$ (1mmol), oleic acid (6 mmol), oleylamine (6 mmol), oleyl alcohol and dibenzyl ether (20 ml) were mixed and magnetically stirred under a flow of Ar. The mixture was heated to 200 °C for 120 min and then, under a blanket of Ar, heated to reflux (300 °C) for another 60 min. Acetone separator was used to remove the forming acetone out of the reaction medium. The black mixture was cooled to room temperature by removing the heat source. Under ambient conditions, ethanol (120 ml) was added to the mixture, and a black material was precipitated and separated via centrifugation. The black product was redispersed in toluene/oleylamine mixture.

To obtain cobalt ferrite particles in form of powder, the particles were washed using the magnetic separation. For this purpose ethanol was used. To the particles dispersion in toluene an excess of ethanol was added (1:4) and a magnet was placed under the vial with particles. The supernatant was discarded, the particles redispersed in 0.5 ml of hexane. Then, to the hexane dispersion ethanol (20 ml) was added and the particles were gathered by a magnet again. Washing is considered to be complete, when the particles are no more stable in hexane.

9.3.2. Synthesis of Ag@CoFe$_2$O$_4$ particles

For the synthesis of dumbbell-like Ag@CoFe$_2$O$_4$ particles, the synthetic approach described by Sun[92] was used as a basis. In a typical synthesis, 5 ml of solution of CoFe$_2$O$_4$ in tetraline with a defined concentration was made, sonicated for 30 min. 5ml solution of silver salt in tetraline with respect concentration (calculated for Ag$^+$), sonicated for 30 min. and then injected into CoFe$_2$O$_4$ solution at 100° C and kept at this temperature for 1 h with magnetic stirring. For all syntheses fresh solution of silver nitrate or silver acetate was used. The resulting solutions were mixed with ethanol, centrifuged and the sediment was separated. The particles were washed using magnetic separation and then redispersed in 1 ml of hexane.

Table 9-2. List of dumbbell-like particles synthesized in tetraline

Sample name	Primary particles	Synthesis temperature [°C]	CoFe$_2$O$_4$ conc. [mg·ml^{-1}]	Ag conc. [mg·ml^{-1}]	CoFe/Ag ratio
DLP-100 1:1	CFO-310	100	0.1	0.1	1:1
DLP-100 4:1	CFO-310	100	0.4	0.1	4:1
DLP-100 4:2	CFO-310	100	0.4	0.2	2:1
DLP-100 4:4	CFO-310	100	0.4	0.4	1:1
DLP-100 8:1	CFO-310	100	0.8	0.1	8:1
DLP-100 8:2	CFO-310	100	0.8	0.2	4:1
DLP-100 8:4	CFO-310	100	0.8	0.4	2:1
DLP-100 8:1-K	CFO-310	100	0.8	0.1	8:1

The synthesis of dumbbell-like Ag@CoFe$_2$O$_4$ particles in toluene with oleylamine was based on the synthetic approach described by Klajn.[93] In a typical synthesis, 60 ml of solution of CoFe$_2$O$_4$ in toluene with a defined concentration was made. Oleylamine and silver acetate were added under Ar blanket. The solution was heated up to 70 °C and kept at this temperature for 12h with magnetic stirring. The resulting yellow-black solution was washed using magnetic separation and then redispersed toluene/oleylamine mixture (10:1).

9.3.3. Synthesis of PAA-SH

Synthesis of poly(tert-butyl acrylate)

The poly(tert-butyl acrylate) was prepared using ATRP. The monomer (tert-butyl acrylate) is purified before each polymerization. To do this, the monomer is filtered through a column with basic aluminum oxide under flowing Ar and then put in a flask with further evacuation and filling with Ar. The catalyst (copper (I) bromide) is stirred for 12 h. with glacial acetic acid and then washed with 80 ml ethanol and 80 ml diethyl ether under flowing Ar. The catalyst is then dried under vacuum and then stored in a desiccator under Ar.

Copper (I) bromide is put into the Schlenck flask, evacuated for 20 min. and filled with Ar. After that, 10 ml of monomer (tert-butyl acrylate) is added, followed by another evacuation and filling with Ar. Then ligand (PMDETA) is added, followed by evacuation and filling with Ar. After that, the rest of the monomer is added and the initiator (MBrP) is added to the mixture. The flask is evacuated shortly and filled with Ar. The polymerization is performed in a slow flow of Ar at 80 °C over night. The resulting polymer is solved in acetone and filtered over a column with neutral aluminum oxide to remove the catalyst. Then the polymer is solved in acetone and precipitated in methanol/water mixture (10:1) three times. After washing the polymer is dried in the vacuum oven for 12 h. at 60 °C.

P(t-BuA) 1k[1]H-NMR: (300 MHz, CDCl$_3$) δ (ppm) = 1.16 (d, overlapped, 3H, f), δ = 1.46 (s, broadened, 9H, a), δ = 1.80 (m, broadened, 2H, b), δ = 2.26 (m, 1H, c), δ = 2.46 (m, overlapped, 1H, e), δ = 2.49 (m, 2H, d), δ = 3.67 (s, 3H, g), δ = 4.11 (m, 1H, h).

P(t-BuA) 10k ^{1}H-NMR: (300 MHz, CDCl$_3$) δ (ppm) = 1.15 (d, overlapped, 3H, f), δ = 1.46 (s, broadened, 9H, a), δ = 1.82 (m, broadened, 2H, b), δ = 2.24 (m, 1H, c), δ = 2.38 (m, overlapped, 1H, e), δ = 2.49 (m, 2H, d), δ = 3.67 (s, 3H, g).

Table 9-3. Experimental details of synthesis of P(t-BuA)

Sample	M_w, g·mol^{-1}	tert-BuA	Cu(I)Br	PMDETA	MBrP
P(t-BuA) 1k	1000	5.0 g	0.34 g	0.43 g	0.83 g
P(t-BuA) 10k	10000	10.0 g	0.068 g	0.086 g	0.17 g

Synthesis of thiol-modified poly(tert-butyl acrylate)

A mixture of poly(tert-butyl acrylate) and thiourea are put into a three-neck flask, evacuated for 2h and filled with Ar. After that, dry DMF is added, the flask is evacuated shortly and filled with Ar. The mixture is heated up to 100 °C for 24 hours under flowing Ar. Then, a solution of sodium hydroxide in water (0.6 mg NaOH in 4.8 ml H$_2$O) is added and the mixture is heated up to 110 °C for another 48 h. After that two drops of concentrated sulfuric acid are added and the mixture is cooled to room temperature and stirred for 12h. The purification is in methanol/water mixture, analogous to the one for the synthesis of poly(tert-butyl acrylate). To remove the traces of DMF the polymer is dried in the vacuum oven at 80 °C for 24 h or more, until the ^{1}H NMR signal of DMF is no longer observed.

P(t-BuA)-SH 1k ^{1}H-NMR: (300 MHz, CDCl$_3$) δ (ppm) = 1.16 (d, overlapped, 3H, f'), δ = 1.46 (s, broadened, 9H, a'), δ = 1.86 (m, broadened, 2H, b'), δ = 2.26 (m, 1H, c'), δ = 2.46 (m, overlapped, 1H, e'), δ = 2.49 (m, 2H, d'), δ = 3.67 (s, 3H, g'), δ = 4.21 (m, 1H, h').

P(t-BuA)-SH 10k ^{1}H-NMR: (300 MHz, CDCl$_3$) δ (ppm) = 1.16 (d, overlapped, 3H, f), δ = 1.46 (s, broadened, 9H, a), δ = 1.85 (m, broadened, 2H, b), δ = 2.25 (m, 1H, c), δ = 2.49 (m, 2H, d), δ = 3.67 (s, 3H, g).

Sample	M_w, [g·mol^{-1}]	P(t-BuA) [g]	Thiourea [g]	V DMF, [ml]
P(t-BuA)-SH 1k	1000	0.85	0.90	30
P(t-BuA)-SH 10k	10000	2.6	0.20	50

Hydrolysis of thiolated poly(tert-butyl acrylate)

To a solution of 90 mg of thiolated poly(tert-butyl acrylate) in 5.0 ml dichloromethane 200 μl of trifluoroacetic acid are added and the mixture is stirred at room temperature for 48 h. The solvent, the rests of TFA and cleaved tert-butyl are removed in the rotational evaporator.

PAA-SH 1k ^{1}H-NMR: (300 MHz, D_2O) δ (ppm) = 1.05 (d, overlapped, 3H, f''), δ = 1.70 (s, broadened, 9H, a'), δ = 1.87 (m, broadened, 2H, b''), δ = 2.34 (m, 1H, c'), δ = 2.62 (m, overlapped, 1H, e''), δ = 2.49 (m, 2H, d''), δ = 3.60 (s, 3H, g''), δ = 4.21 (m, 1H, h').

PAA-SH 10k ^{1}H-NMR: (300 MHz, D_2O) δ (ppm) = 1.11 (d, 3H, f''), δ = 1.62 (s, broadened, 9H, a'), δ = 1.92 (m, broadened, 2H, b''), δ = 2.39 (m, 2H, d''), δ = 3.65 (s, 3H, g'').

9.3.4. Surface modification of Ag@CoFe$_2$O$_4$ particles

To perform the transfer of the Ag@CoFe$_2$O$_4$ particles into aqueous medium the dispersion of the particles in toluene/oleylamine (10:1) (30.0 ml with concentration of 1.0 mg·ml^{-1}) was washed magnetically with ethanol twice to remove the excess of oleylamine. Then the particles were precipitated with an excess of ethanol and redispersed in 25 ml THF. Then 5 ml solution of PAA in THF (M_w = 1800 g·mol^{-1}, 20 mg·ml^{-1}) was added. The mixture was heated up to 70 °C and maintained at this temperature for 4 hours at vigorous shaking. After cooling the flask 20 ml of hexane were added, the supernatant was discarded and to the precipitated particles 15 ml EtOH was added to remove the excess of polyacrylic acid. Washing with EtOH was repeated twice, then 5 ml of synthetic H_2O was added and pH was adjusted to slightly basic value (between 7.0 and 8.0) with commercially available 0.1 M NaOH solution.

Appendix

Table A-1. Magnetic properties of CoFe$_2$O$_4$ nanoparticles

Sample name	m, [10^{19} A·m^2]	d_{mag}, [nm]	Mr/M_S	Hc, [kA·m^{-1}]	M_S, [A·m^2·kg^{-1}]	$\mu_{CoFe2O4}$, [%]
CFO-310	0.79	7.2	0.23	54.7	4.9	6.5
CFO-315	1.59	9.1	0.24	50.5	9.4	12.5
CFO-320	1.12	8.1	0.23	53.6	30.6	40.5
CFA-300/1h×2-1	1.16	8.2	-	-	-	-
CFA-300/1h×2-2	1.53	9.0	0.08	6.93	64.6	85.5
CFA-280/1h×8-1	0.93	7.6	-	-	-	-
CFA-280/1h×8-2	1.21	8.3	-	-	-	-
CFA-280/1h×8-3	1.44	8.9	-	-	-	-
CFA-280/1h×8-4	1.53	9.0	-	-	-	-
CFA-280/1h×8-5	1.62	9.2	-	-	-	-
CFA-280/1h×8-6	1.82	9.5	-	-	-	-
CFA-280/1h×8-7	1.82	9.5	-	-	-	-
CFA-280/1h×8-8	1.90	9.9	0.21	20.6	54.3	72.0
CFA-280/2h×5-1	0.70	6.9	-	-	-	-
CFA-280/2h×5-2	1.25	8.4	-	-	-	-
CFA-280/2h×5-3	1.34	8.6	-	-	-	-
CFA-280/2h×5-4	1.44	8.9	-	-	-	-
CFA-280/2h×5-5	1.89	9.7	0.17	13.4	65.8	87.2
CFA-280/2h×2-1	1.25	8.4	-	-	-	-
CFA-280/2h×2-2	1.82	9.5	0.11	6.3	72.3	95.7

Bibliography

[1]   B. J. Nelson, I. K. Kaliakatsos, J. J. Abbott, *Annu. Rev. Biomed. Eng.* **2010**, *12*, 55–85.

[2]   K. E. Peyer, S. Tottori, F. Qiu, L. Zhang, B. J. Nelson, *Chem. - A Eur. J.* **2013**, *19*, 28–38.

[3]   S. Balasubramanian, D. Kagan, C. M. Jack Hu, S. Campuzano, M. J. Lobo-Castanon, N. Lim, D. Y. Kang, M. Zimmerman, L. Zhang, J. Wang, *Angew. Chemie - Int. Ed.* **2011**, *50*, 4161–4164.

[4]   V. Garcia-Gradilla, J. Orozco, S. Sattayasamitsathit, F. Soto, F. Kuralay, A. Pourazary, A. Katzenberg, W. Gao, Y. Shen, J. Wang, *ACS Nano* **2013**, *7*, 9232–9240.

[5]   J. Wang, W. Gao, *ACS Nano* **2012**, *6*, 5745–5751.

[6]   L. Zhang, T. Petit, K. E. Peyer, B. J. Nelson, *Nanomedicine Nanotechnology, Biol. Med.* **2012**, *8*, 1074–1080.

[7]   C. J. Kearney, H. Skaat, S. M. Kennedy, J. Hu, M. Darnell, T. M. Raimondo, D. J. Mooney, *Adv. Healthc. Mater.* **2015**, *4*, 1634–1639.

[8]   L. Soler, S. Sánchez, *Nanoscale* **2014**, *6*, 7175.

[9]   W. Gao, J. Wang, *ACS Nano* **2014**, *8*, 3170–3180.

[10]   Z. Zhang, A. Zhao, F. Wang, J. Ren, X. Qu, *Chem. Commun.* **2016**, DOI 10.1039/C6CC00910G.

[11]   J. Orozco, V. Garcia-Gradilla, M. D'Agostino, W. Gao, A. Cortes, J. Wang, *ACS Nano* **2013**, *7*, 818–824.

[12]   S. Kim, F. Qiu, S. Kim, A. Ghanbari, C. Moon, L. Zhang, B. J. Nelson, H. Choi, *Adv. Mater.* **2013**, *25*, 5863–5868.

[13]   T. Y. Huang, F. Qiu, H. W. Tung, X. B. Chen, B. J. Nelson, M. S. Sakar, *Appl. Phys. Lett.* **2014**, *105*, DOI 10.1063/1.4895937.

[14]   E. M. Purcell, *Am. J. Phys.* **1977**, *45*, 3–11.

[15]   R. Piazza, *Soft Matter* **2008**, *4*, 1740.

[16]   O. Ilic, I. Kaminer, Y. Lahini, H. Buljan, M. Soljačić, *ACS Photonics* **2016**, acsphotonics.5b00605.

[17]   S. Nedev, S. Carretero-Palacios, P. Kühler, T. Lohmüller, A. S. Urban, L. J. E. Anderson, J. Feldmann, *ACS Photonics* **2015**, *2*, 491–496.

[18]   L. Baraban, R. Streubel, D. Makarov, L. Han, D. Karnaushenko, O. G. Schmidt, G. Cuniberti, *ACS Nano* **2013**, *7*, 1360–1367.

[19]   H.-R. Jiang, N. Yoshinaga, M. Sano, *Phys. Rev. Lett.* **2010**, *105*, 268302.

[20]   F. Lugli, E. Brini, F. Zerbetto, *J. Phys. Chem. C* **2011**, *116*, 592–598.

[21]   R. Dong, J. Li, I. Rozen, B. Ezhilan, T. Xu, *Nat. Publ. Gr.* **2015**, 1–7.

[22]   T. Lee, M. Alarco, C. Miksch, K. Hahn, J. G. Gibbs, **2014**.

[23]   N. Mano, A. Heller, *J. Am. Chem. Soc.* **2005**, *127*, 11574–11575.

[24]   S. Gangwal, O. Cayre, M. Bazant, O. Velev, *Phys. Rev. Lett.* **2008**, *100*, 1–4.

[25]   W. F. Paxton, A. Sen, T. E. Mallouk, *Chemistry (Easton).* **2005**, *11*, 6462–6470.

[26]   P. Mitchell, *FEBS Lett.* **1972**, *28*, 1–4.

[27]   R. Dreyfus, J. Baudry, M. L. Roper, M. Fermigier, H. a Stone, J. Bibette, *Nature* **2005**, *437*, 862–865.

[28]   P. Fischer, A. Ghosh, *Nanoscale* **2011**, *3*, 557–563.

[29]   B. Jang, E. Gutman, N. Stucki, B. F. Seitz, P. D. Wendel-García, T. Newton, J. Pokki, O. Ergeneman, S. Pané, Y. Or, et al., *Nano Lett.* **2015**, *15*, 4829–4833.

[30]   B. J. Williams, S. V Anand, J. Rajagopalan, M. T. a Saif, *Nat. Commun.* **2014**, *5*, 3081.

[31]   E. M. Purcell, *Proc. Natl. Acad. Sci. U. S. A.* **1997**, *94*, 11307–11311.

[32]   W. Gao, D. Kagan, O. S. Pak, C. Clawson, S. Campuzano, E. Chuluun-Erdene, E. Shipton, E. E. Fullerton, L. Zhang, E. Lauga, et al., *Small* **2012**, *8*, 460–467.

[33]   L. Turner, W. S. Ryu, H. C. Berg, *J. Bacteriol.* **2000**, *182*, 2793–2801.

[34]   A. M. Maier, C. Weig, P. Oswald, E. Frey, P. Fischer, T. Liedl, *Nano Lett.* **2016**, acs.nanolett.5b03716.

[35]   A. Ghosh, P. Fischer, *Nano Lett.* **2009**, *9*, 2243–5.

[36]   D. Schamel, A. Mark, J. Gibbs, C. Miksch, *ACS Nano* **2014**, *8*, 8794–8801.

[37]   S. Tottori, L. Zhang, F. Qiu, K. K. Krawczyk, A. Franco-Obregón, B. J. Nelson, *Adv. Mater.* **2012**, *24*, 811–816.

[38]   S. Tottori, B. J. Nelson, *Biomicrofluidics* **2013**, *7*, 61101.

[39]   A. W. Mahoney, N. D. Nelson, K. E. Peyer, B. J. Nelson, J. J. Abbott, *Appl. Phys. Lett.* **2014**, *104*, 1–4.

[40]   S. Eslami, J. G. Gibbs, Y. Rechkemmer, J. Van Slageren, M. Alarcón-Correa, T. C. Lee, A. G. Mark, G. L. J. A. Rikken, P. Fischer, *ACS Photonics* **2014**, *1*, 1231–1236.

[41]   A. Ghosh, A. Ghosh, D. Paria, G. Rangarajan, *J. Phys. Chem. Lett.* **2014**, *5*, 62–68.

[42]   H. Aono, H. Ebara, R. Senba, T. Naohara, T. Maehara, H. Hirazawa, Y. Watanabe, *J. Magn. Magn. Mater.* **2012**, *324*, 1985–1991.

[43]   C. H. Wiggins, R. E. Goldstein, *Phys. Rev. Lett.* **1997**, *2*, 4.

[44]   C. P. Lowe, *Philos. Trans. R. Soc. Lond. B. Biol. Sci.* **2003**, *358*, 1543–1550.

[45]   M. C. Lagomarsino, F. Capuani, C. P. Lowe, *J. Theor. Biol.* **2003**, *224*, 215–224.

[46]   A. Cebers, *Curr. Opin. Colloid Interface Sci.* **2005**, *10*, 167–175.

[47]   K. Ērglis, R. Livanovičs, a. Cēbers, *J. Magn. Magn. Mater.* **2011**, *323*, 1278–1282.

[48]   R. Livanovičs, A. Cēbers, *Phys. Rev. E* **2012**, *85*, 041502.

[49]   E. Gauger, H. Stark, *Phys. Rev. E - Stat. Nonlinear, Soft Matter Phys.* **2006**, *74*, 1–10.

[50]   H. Diamant, *Hydrodynamic Properties of Colloids (Internal Report)*, **2011**.

[51]   G. Falkovich, *Fluid Mechanics*, Cambridge University Press, Cambridge, **2010**.

[52]   P. W. Atkins, J. de Paula, *Physikalische Chemie*, Wiley-IEEE Press, Freiburg, **2006**.

[53]   A. Einstein, *Ann. Phys.* **1905**, *322*, 549–560.

[54]   V. LaMer, R. Dinegar, *J. Am. Chem. Soc.* **1950**, *72*, 4847–4854.

[55] N. Bao, L. Shen, W. An, P. Padhan, C. Heath Turner, A. Gupta, *Chem. Mater.* **2009**, *21*, 3458–3468.

[56] W. Ostwald, *Z. Phys. Chem* **1900**, *34*, 495–503.

[57] I. M. Lifshitz, V. V. Slyozov, *J. Phys. Chem. Solids* **1961**, *19*, 35–50.

[58] H. M. Zheng, R. K. Smith, Y. W. Jun, C. Kisielowski, U. Dahmen, A. P. Alivisatos, *Science* **2009**, *324*, 1309–1312.

[59] M. Niederberger, H. Cölfen, *Phys. Chem. Chem. Phys.* **2006**, *8*, 3271–3287.

[60] S. Sultana, Rafiuddin, M. Zain Khan, K. Umar, *J. Alloys Compd.* **2012**, *535*, 44–49.

[61] S. Ammar, A. Helfen, N. Jouini, F. Fiévet, I. Rosenman, F. Villain, P. Molinié, M. Danot, *J. Mater. Chem.* **2001**, *11*, 186–192.

[62] M. G. Naseri, E. B. Saion, M. Hashim, A. H. Shaari, H. A. Ahangar, *Solid State Commun.* **2011**, *151*, 1031–1035.

[63] M. Goodarz Naseri, E. Bin Saion, H. A. Ahangar, M. Hashim, A. H. Shaari, *J. Magn. Magn. Mater.* **2011**, *323*, 1745–1749.

[64] K. Maaz, S. Karim, A. Mumtaz, S. K. Hasanain, J. Liu, J. L. Duan, *J. Magn. Magn. Mater.* **2009**, *321*, 1838–1842.

[65] D.-H. Chen, X.-R. He, *Mater. Res. Bull.* **2001**, *36*, 1369–1377.

[66] S. Sun, H. Zeng, D. Robinson, *J. Am. Chem. Soc.* **2004**, *4*, 126–132.

[67] J. Xu, H. Yang, W. Fu, K. Du, Y. Sui, J. Chen, Y. Zeng, M. Li, G. Zou, *J. Magn. Magn. Mater.* **2007**, *309*, 307–311.

[68] C. Cannas, A. Musinu, D. Peddis, G. Piccaluga, *Chem. Mater.* **2006**, *18*, 3835–3842.

[69] M. Atif, S. K. Hasanain, M. Nadeem, *Solid State Commun.* **2006**, *138*, 416–421.

[70] N. Frickel, R. Messing, T. Gelbrich, A. M. Schmidt, *Langmuir* **2010**, *26*, 2839–2846.

[71] M. C. Mascolo, Y. Pei, T. A. Ring, *Materials (Basel).* **2013**, *6*, 5549–5567.

[72] F. N. H. Oh, M. Tajabadi, M. E. Khosroshahi, *Int. J. Chem. Eng. Appl.* **2012**, *3*, 3–7.

[73] I. Sharifi, H. Shokrollahi, M. M. Doroodmand, R. Safi, *J. Magn. Magn. Mater.* **2012**, *324*, 1854–1861.

[74] J. Park, K. An, Y. Hwang, J.-G. Park, H.-J. Noh, J.-Y. Kim, J.-H. Park, N.-M. Hwang, T. Hyeon, *Nat. Mater.* **2004**, *3*, 891–895.

[75] B. Kalska-Szostko, U. Wykowska, D. Satuła, *Appl. Surf. Sci.* **2014**, *306*, 7–15.

[76] Q. Dai, M. Lam, S. Swanson, R. R. Yu, D. J. Milliron, T. Topuria, P. Jubert, A. Nelson, *Langmuir* **2010**, *26*, 17546–17551.

[77] N. T. K. Thanh, N. Maclean, S. Mahiddine, *Chem. Rev.* **2014**, *114*, 7610–7630.

[78] A. Henglein, M. Giersig, *J. Phys. Chem. B* **1999**, *103*, 9533–9539.

[79] M. Harada, E. Katagiri, *Langmuir* **2010**, *26*, 17896–17905.

[80] J. E. Mondloch, X. Yan, R. G. Finke, *J. Am. Chem. Soc.* **2009**, *131*, 6389–6396.

[81] V. N. Richards, N. P. Rath, W. E. Buhro, *Chem. Mater.* **2010**, *22*, 3556–3567.

[82] S. Sun, H. Yu, S. Wang, *US Pat. 7,288,134* **2007**.

[83]   H. Yu, M. Chen, P. M. Rice, S. X. Wang, R. L. White, S. Sun, *Nano Lett.* **2005**, *5*, 379–382.

[84]   S. Peng, C. Lei, Y. Ren, R. E. Cook, Y. Sun, *Angew. Chem. Int. Ed. Engl.* **2011**, *50*, 3158–3163.

[85]   L. Zhang, Y.-H. Dou, H.-C. Gu, *J. Colloid Interface Sci.* **2006**, *297*, 660–664.

[86]   C. Wang, H. Daimon, S. Sun, *Nano Lett.* **2009**, *9*, 1493–1496.

[87]   C. Xu, B. Wang, S. Sun, *J. Am. Chem. Soc.* **2009**, *131*, 4216–4217.

[88]   I. Schick, S. Lorenz, D. Gehrig, S. Tenzer, W. Storck, K. Fischer, D. Strand, F. Laquai, W. Tremel, *Beilstein J. Nanotechnol.* **2014**, *5*, 2346–2362.

[89]   S. Chakrabortty, J. A. Yang, Y. M. Tan, N. Mishra, Y. Chan, *Angew. Chem. Int. Ed. Engl.* **2010**, *49*, 2888–2892.

[90]   B. H. McNaughton, P. Kinnunen, M. Shlomi, C. Cionca, S. N. Pei, R. Clarke, P. Argyrakis, R. Kopelman, *J. Phys. Chem. B* **2011**, *115*, 5212–5218.

[91]   S. K. Sharma, G. Lopes, J. M. Vargas, L. M. Socolovsky, K. R. Pirota, M. Knobel, *J. Appl. Phys.* **2011**, *109*, 07B530.

[92]   Y. Li, Q. Zhang, A. V Nurmikko, S. Sun, *Nano Lett.* **2005**, *5*, 1689–1692.

[93]   Y. Ridelman, G. Singh, R. Popovitz-Biro, S. G. Wolf, S. Das, R. Klajn, *Small* **2012**, *8*, 654–660.

[94]   O. Moscoso-Lodoño, D. Muraca, P. Tancredi, C. Cosio-Castañeda, K. R. Pirota, L. M. Socolovsky, *J. Phys. Chem. C* **2014**, *118*, 13168–13176.

[95]   A. Figuerola, M. van Huis, M. Zanella, A. Genovese, S. Marras, A. Falqui, H. W. Zandbergen, R. Cingolani, L. Manna, *Nano Lett.* **2010**, *10*, 3028–3036.

[96]   I. V. Markov, *Crystal Growth for Beginners*, World Scientific Publishing Co. Pte. Ltd., Singapore, **1995**.

[97]   V. G. Dubrovskii, *Nucleation Theory and Growth of Nanostructures*, **2014**.

[98]   K. Oura, V. G. Lifshits, A. A. Saranin, A. V. Zotov, M. Katayama, *Surface Science: An Introduction*, Springer-Verlag Berlin Heidelberg New York, Heidelberg, **2010**.

[99]   D. Turnbull, *J. Chem. Phys.* **1950**, *18*, 198–203.

[100] E. H. Frei, S. Shtrikman, D. Treves, *Phys. Rev.* **1957**, *106*, 446–455.

[101] L. G. Parry, *Philos. Mag.* **1965**, *11*, 303–312.

[102] S. Odenbach, *Colloidal Magnetic Fluids: Basics, Development and Application of Ferrofluids*, Springer Berlin Heidelberg, Berlin, Heidelberg, **2009**.

[103] R. Chantrell, *IEEE Trans.* **1978**, 975–977.

[104] W. Fuller Brown, *Phys. Rev.* **1963**, *130*, 1677–1686.

[105] E. P. Wohlfarth, *Handbook of Magnetic Materials - 3*, **1982**.

[106] "Stoner-Wohlfarth Theory," can be found under https://www.google.com/url?sa=t&rct=j&q=&esrc=s&source=web&cd=6&ved=0ahU KEwjNwffSj6LLAhXFLw8KHUWtAIwQFgg6MAU&url=https://www.tu-chemnitz.de/physik/OFGF/lectures/external/bill/sw.pptx&usg=AFQjCNG4UvifFh0mb LmC_x1c2AVZp7Hk9A&sig2=60gz7-ITAm, **n.d.**

[107] D. J. Dunlop, *Phys. Earth Planet. Inter.* **1981**, *26*, 1–26.

[108] A. G. Kolhatkar, A. C. Jamison, D. Litvinov, R. C. Willson, T. R. Lee, *Tuning the Magnetic Properties of Nanoparticles*, **2013**.

[109] R. G. Jones, E. S. Wilks, W. V. Metanomski, J. Kahovec, M. Hess, R. Stepto, *Compendium of Polymer Terminology and Nomenclature*, **2010**.

[110] J. S. Wang, K. Matyjaszewski, *J. Am. Chem. Soc.* **1995**, *117*, 5614–5615.

[111] K. Matyjaszewski, J. Xia, *Chem. Rev.* **2001**.

[112] J.-S. Wang, K. Matyjaszewski, *Macromolecules* **1995**, *28*, 7901–7910.

[113] W. a. Braunecker, K. Matyjaszewski, *Prog. Polym. Sci.* **2007**, *32*, 93–146.

[114] K. a Davis, K. Matyjaszewski, **2000**, 4039–4047.

[115] A. D. Jenkins, P. Kratochvíl, R. F. T. Stepto, U. W. Suter, *Pure Appl. Chem.* **1996**, *68*, 2287–2311.

[116] G. Miquelard-Garnier, C. Creton, D. Hourdet, *Soft Matter* **2008**, *4*, 1011–1023.

[117] B. Tieke, *Makromolekulare Chemie*, Wiley-VCH, Weinheim, **2005**.

[118] M. Hara, *Polyelectrolytes: Science and Technology*, CRC Press, **1992**.

[119] S. Cranford, M. Buehler, *Macromolecules* **2012**, *45*, 8067–8082.

[120] C. Bustamante, S. B. Smith, J. Liphardt, D. Smith, *Curr. Opin. Struct. Biol.* **2000**, *10*, 279–285.

[121] T. Odijk, *J. Polym. Sci. Polym. Phys. Ed.* **1977**, *15*, 477–483.

[122] J. Skolnick, M. Fixman, *J. Phys. Chem. B* **2010**, *114*, 3185–3196.

[123] M. Ullner, *J. Phys. Chem. B* **2003**, *107*, 8097–8110.

[124] S. T. Dubas, J. B. Schlenoff, *Macromolecules* **1999**, *32*, 8153–8160.

[125] K. Büscher, K. Graf, H. Ahrens, C. A. Helm, *Langmuir* **2002**, *18*, 3585–3591.

[126] B. Lee, S. Koo, *J. Ind. Eng. Chem.* **2012**, *18*, 1191–1195.

[127] G. Lopes, J. Vargas, S. Sharma, *J. Phys. Chem. C* **2010**, 10148–10152.

[128] S. Chikazumi, *Physics of Ferromagnetism*, Clarendon Press, Oxford, **1997**.

[129] B. D. Cullity, C. D. Graham, *Introduction to Magnetic Materials*, Wiley-IEEE Press, Piscataway, **2009**.

[130] W. Gan, B. Xu, H.-L. Dai, *Angew. Chem. Int. Ed. Engl.* **2011**, *50*, 6622–6625.

[131] K. J. Klabunde, R. M. Richards, *Nanoscale Materials in Chemistry*, Wiley, Hoboken, **2009**.

[132] M. J. Davies, S. C. Parker, G. W. Watson, *J. Mater. Chem.* **1994**, *4*, 813–816.

[133] J. Von Hoene, R. G. Charles, W. M. Hickam, *J. Phys. Chem.* **1958**, *62*, 1098–1101.

[134] A. D. Pomogailo, G. I. Dzhardimalieva, *Nanostructured Materials Preparation via Condensation Ways*, **2014**.

[135] S. Mourdikoudis, L. M. Liz-marzán, *Chem. Matter.* **2013**, *25*, 1465–1476.

[136] X. Hong, M. Li, N. Bao, E. Peng, W. Li, J. Xue, J. Ding, *J. Nanoparticle Res.* **2014**,

16, DOI 10.1007/s11051-013-1935-4.

[137] E. Wetterskog, M. Agthe, A. Mayence, J. Grins, D. Wang, S. Rana, A. Ahniyaz, G. Salazar-Alvarez, L. Bergström, *Sci. Technol. Adv. Mater.* **2014**, *15*, 055010.

[138] L. Tauxe, T. a. . Mullender, T. Pick, *J. Geophys. Res.* **1996**, *101*, 571–583.

[139] P. J. Wasilewski, *Earth Planet. Sci. Lett.* **1973**, *20*, 67–72.

[140] Ö. Özdemir, D. J. Dunlop, *J. Geophys. Res.* **1985**, *90*, 11513–11523.

[141] M. Feyen, E. Heim, F. Ludwig, A. M. Schmidt, *Chem. Mater.* **2008**, *20*, 2942–2948.

[142] F. Ludwig, A. Guillaume, M. Schilling, N. Frickel, A. M. Schmidt, *J. Appl. Phys.* **2010**, *108*, 033918.

[143] E. Roeben, L. Roeder, S. Teusch, M. Effertz, U. K. Deiters, A. M. Schmidt, *Colloid Polym. Sci.* **2014**, *292*, 2013–2023.

[144] H. E. Swanson, H. F. McMurdie, M. C. Morris, E. H. Evans, B. Paretzkin, *Standard X-Ray Diffraction Powder Patterns*, Nat. Bur. Stand. (U.S.), **1971**.

[145] E. Wetterskog, C. Tai, J. Grins, *ACS Nano* **2013**, *7*, 7132–7144.

[146] E. Wetterskog, M. Agthe, A. Mayence, J. Grins, *Sci. Technol. Adv. Mater.* **2014**, *15*, DOI 10.1088/1468-6996/15/5/055010.

[147] B. P. Pichon, O. Gerber, C. Lefevre, I. Florea, S. Fleutot, W. Baaziz, M. Pauly, M. Ohlmann, C. Ulhaq, O. Ersen, et al., *Chem. Mater.* **2011**, *23*, 2886–2900.

[148] E. R. Jette, F. Foote, *J. Chem. Phys.* **1933**, *1*, 29.

[149] S. Saito, K. Nakahigashi, Y. Shimomura, *J. Phys. Soc. Japan* **1966**, *21*, 850–860.

[150] C. Wang, Y. Wei, H. Jiang, S. Sun, *Nano Lett.* **2009**, *9*, 4544–4547.

[151] S. Sun, H. Yu, S. Wang, *US Pat. 7,288,134* **2007**.

[152] C. Wang, C. Xu, H. Zeng, S. Sun, *Adv. Mater.* **2009**, *21*, 3045–3052.

[153] M. Chen, Y.-G. Feng, X. Wang, T.-C. Li, J.-Y. Zhang, Qian, *Langmuir* **2007**, *23*, 5296–5304.

[154] V. I. Klimov, *Nanocrystal Quantum Dots Second Edition*, CRC Press, Boca Raton, **2010**.

[155] H. Zeng, S. Sun, *Adv. Funct. Mater.* **2008**, *18*, 391–400.

[156] G. Antczak, G. Ehrlich, *Surface Diffusion*, Cambridge University Press, Cambridge, **2010**.

[157] L. Duo, M. Finazzi, F. Ciccacci, *Magnetic Properties of Antiferromagnetic Oxide Materials: Surfaces, Interfaces, and Thin Films*, Wiley-VCH, Weinheim, **2010**.

[158] C. R. Stoldt, C. J. Jenks, P. a. Thiel, a. M. Cadilhe, J. W. Evans, *J. Chem. Phys.* **1999**, *111*, 5157.

[159] S. W. Cranford, C. Ortiz, M. J. Buehler, *Soft Matter* **2010**, *6*, 4175–4188.

[160] O. Colombani, M. Ruppel, F. Schubert, *Macromolecules* **2007**, *40*, 4338–4350.

[161] L. Garamszegi, C. Donzel, G. Carrot, *React. Funct. Polym.* **2003**, *55*, 179–183.

[162] H. Gottlieb, V. Kotlyar, A. Nudelman, *J. Org. Chem.* **1997**, *62*, 7512–7515.

[163] H. Hiramatsu, F. E. Osterloh, *Chem. Mater.* **2004**, *16*, 2509–2511.

[164] C. G. Blatchford, O. Siiman, M. Kerker, *J. Phys. Chem.* **1983**, *87*, 2503–2508.

[165] P. Mulvaney, *Langmuir* **1996**, *12*, 788–800.

[166] A. Henglein, *J. Phys. Chem.* **1993**, *97*, 5457–5471.

[167] K. B. Mogensen, K. Kneipp, *J. Phys. Chem. C* **2014**, *118*, 28075–28083.

[168] M. G. Bellino, E. J. Calvo, G. Gordillo, *Phys. Chem. Chem. Phys.* **2004**, *6*, 424–428.

[169] S. Peng, J. M. McMahon, G. C. Schatz, S. K. Gray, Y. Sun, *Proc. Natl. Acad. Sci.* **2010**, *107*, 14530–14534.

[170] P. Barland, M. Rojkind, *Nature* **1966**, *212*, 84–85.

[171] S. Chen, A. E. Goode, J. N. Skepper, A. J. Thorley, J. M. Seiffert, K. F. Chung, T. D. Tetley, M. S. P. Shaffer, M. P. Ryan, A. E. Porter, *J. Microsc.* **2015**, *261*, 157–166.

[172] M. A. Hayat, *Basic Techniques For Transmission Electron Microscopy*, Academic Press. Inc, San Diego, **1986**.

[173] M. A. Hayat, *Immunogold-Silver Staining: Principles, Methods, and Applications*, CRC Press, **1995**.

[174] D. Lehner, H. Lindner, O. Glatter, *Langmuir* **2000**.

[175] M. M. Tirado, C. L. Martínez, J. G. de la Torre, *J. Chem. Phys.* **1984**, *81*, 2047–2052.

[176] R. Metzler, J. Klafter, *Phys. Rep.* **2000**, *339*, 1–77.

[177] M. Rubinstein, R. H. Colby, *Polymer Physics*, Oxford University Press, Oxford, **2011**.

[178] I. Teraoka, *Polymer Solutions An Introduction to Physical Properties*, Wiley-Interscience, New York, **2002**.

[179] W. W. Kestin Joseph, Sokolov Mordechai, *J. Phys. Chem. Ref. Data* **1978**, *7*, 941–948.

[180] Z. Adamczyk, A. Bratek, B. Jachimska, T. Jasinski, P. Warszynski, *J. Phys. Chem. B* **2006**, *110*, 22426–22435.

[181] J. Feng, S. K. Cho, *Micromachines* **2014**, *5*, 97–113.

Index of Figures

Index of Tables

Eidesstattliche Erklärung

Ich versichere, dass ich die von mir vorgelegte Dissertation selbständig angefertigt, die benutzten Quellen und Hilfsmittel vollständig angegeben und die Stellen der Arbeit - einschließlich Tabellen und Abbildungen -, die anderen Werken im Wortlaut oder dem Sinn nach entnommen sind, in jedem Einzelfall als Entlehnung kenntlich gemacht habe; dass diese Dissertation noch keiner anderen Fakultät oder Universität zur Prüfung vorgelegen hat; dass sie noch nicht veröffentlicht worden ist sowie, dass ich eine solche Veröffentlichung vor Abschluss des Promotionsverfahrens nicht vornehmen werde. Die Bestimmungen der Promotionsordnung sind mir bekannt. Die von mir vorgelegte Dissertation ist von Prof. Dr. Annette M. Schmidt betreut worden.

Teilpublikationen liegen nicht vor

Köln, den 9.5.2016

Alexey Bushmelev

Curriculum Vitae

Alexey Bushmelev

geboren am 05.03.1987 in Nowosibirsk

Staatsangehörigkeit: Russische Föderation

Familienstand: ledig

<u>Schulbildung und Studium</u>

1994-2004	Schulausbildung in der Mittelschule №130, Nowosibirsk
2004-2009	Studium an der Fakultät für Naturwissenschaften, Abteilung Chemie, Nowosibirsker Staatliche Universität
2007-2009	Diplomarbeit im Laboratorium für katalytische Polymerisation der Olefine am Institut für Katalyse SO RAN zum Thema „Synthese und Untersuchung von Bis(imino)pyridinkomplexen von Cobalt als Katalysatoren für die Ethylenpolymerisation"
2009-2010	Promotion an der Heinrich-Heine Universität Düsseldorf, Institut für Organische Chemie (II), Gruppe von Prof. Dr. A. M. Schmidt
2010 - …	Promotion an der Universität zu Köln, Institut für Physikalische Chemie, Gruppe von Prof. Dr. A. M. Schmidt